

QuSquare: Scalable Quality-Oriented Benchmark Suite for Pre-Fault-Tolerant Quantum Devices

David Aguirre*,^{1,2} Rubén Peña*,² and Mikel Sanz^{1,2,3,4}

¹*Department of Physical Chemistry, University of the Basque Country UPV/EHU, Apartado 644, 48080 Bilbao, Spain*

²*BCAM - Basque Center for Applied Mathematics,*

Mazarredo, 14 E48009 Bilbao, Basque Country – Spain

³*EHU Quantum Center, University of the Basque Country UPV/EHU, Apartado 644, 48080 Bilbao, Spain*

⁴*IKERBASQUE, Basque Foundation for Science, Plaza Euskadi 5, 48009, Bilbao, Spain*

As quantum technologies continue to advance, the proliferation of hardware architectures with diverse capabilities and limitations has underscored the importance of benchmarking as a tool to compare performance across platforms. Achieving fair, scalable and consistent evaluations is a key open problem in quantum computing, particularly in the pre-fault-tolerant era. To address this challenge, we introduce QuSquare, a quality-oriented benchmark suite designed to provide a scalable, fair, reproducible, and well-defined framework for assessing the performance of quantum devices across hardware architectures. QuSquare consists of four benchmark tests that evaluate quantum hardware performance at both the system and application levels: Partial Clifford Randomized, Multipartite Entanglement, Transverse Field Ising Model (TFIM) Hamiltonian Simulation, and Data Re-Uploading Quantum Neural Network (QNN). Together, these benchmarks offer an integral, hardware-agnostic, and impartial methodology to quantify the quality and capabilities of current quantum computers, supporting fair cross-platform comparisons and fostering the development of future performance standards.

I. INTRODUCTION

The rapid development of quantum computing has led to a proliferation of hardware architectures, each with different capabilities and limitations. This raises a key challenge: how the performance of different quantum computers should be fairly compared. As in classical computing, quantum benchmarks are essential not only to track technological progress but also to identify the strengths, limitations, and areas for improvement of hardware platforms. However, designing fair and consistent benchmarks is challenging, since current quantum devices differ in scale, underlying technology, connectivity, supported gate sets, and other features. This diversity makes it challenging to establish common standards for evaluation. In the absence of rigorous quantum benchmarks, there is a risk of relying on misleading performance metrics that may distort research priorities, create a false perception of technological progress, complicate the development of technology roadmaps for industry, and lead to biased comparisons between architectures [1].

Several efforts have been made to evaluate the performance of real quantum processors across different technologies, including superconducting circuits, trapped-ion, cold atoms, and other emerging platforms [2–23]. These evaluations have been carried out at different levels of quantum hardware abstraction, using diverse workloads and methodologies. Nevertheless, in several cases the use of a single metric has led to biased assessments of hardware performance. While these evaluations provide

valuable insights into the capabilities of each hardware platform for a particular workload, direct comparisons across hardware lack validity. This situation highlights the need for more than a single metric and for a common framework for performance assessment. One way to address this challenge is through benchmark suites, which provide a methodology for evaluating quantum devices through a set of workloads and evaluation criteria. This helps reduce the heterogeneity of individual studies. Recent initiatives in the quantum computing community have led to the development of benchmark suites [24–34], which include several workloads designed to assess performance at multiple levels — from component level tests that characterize individual hardware elements to system- and application- level tests that evaluate the whole quantum processor. Despite these advances, the lack of standardized methodologies for designing benchmark suites and defining evaluation criteria remains a key challenge for fair comparison of quantum hardware performance.

In recent years, the quantum computing community has emphasized the need to establish quality attributes that benchmark suites should satisfy [1, 35–37], as well as efforts toward the standardization of performance evaluation methodologies [1, 38–40]. In particular, several attributes have been identified as essential for the design of reliable benchmark suites. Firstly, given the rapid growth in the number of qubits in quantum hardware, *scalability* emerges as a fundamental requirement for benchmarks, ensuring that devices with a large number of qubits can be efficiently evaluated. Furthermore, given the diversity of platforms currently available, benchmarks should be impartial and not favor any particular technology, allowing *fair* comparisons between them. Finally, benchmarks should be well-defined, with clear protocols and

* These authors contributed equally to this work.

compilation rules that eliminate ambiguity, ensuring *reproducibility* across providers and users, and guaranteeing that quantum computers are evaluated on a common basis.

Considering the quality attributes that a quantum benchmark suite should satisfy, we propose QuSquare, a suite composed of both system- and application-level tests to assess the performance of pre-fault-tolerant quantum devices. Taken together, these tests are designed to ensure that the suite satisfies the following quality criteria: scalability, fairness, relevance, verifiability and reproducibility.

To this end, the QuSquare suite consists of a set of tests designed to evaluate different aspects of quantum hardware performance. The test suite includes four benchmarks: Partial Clifford Randomized, Multipartite Entanglement, Transverse Field Ising Model (TFIM) Hamiltonian Simulation, and Data Re-uploading Quantum Neural Network (QNN). The Partial Clifford benchmark assesses the accuracy with which a quantum processor implements a subset of Clifford gates, which is particularly relevant in contexts such as quantum error correction. The Multipartite Entanglement benchmark evaluates the ability of quantum processors to generate genuine multipartite entanglement, a key resource in quantum computing. The TFIM Hamiltonian Simulation benchmark evaluates the capability of quantum hardware to simulate a quantum many-body dynamics by means of the transverse field Ising model. Finally, the Data Re-uploading QNN benchmark assesses the performance of the hardware in classification problems.

This article is organized as follows. In Section II, we describe the design criteria adopted for the QuSquare suite. We discuss the scope and abstraction levels considered, the quality attributes that guided its design, and the strategies adopted to ensure hardware-agnostic and fair performance evaluation across different quantum computing platforms. In Section III, we introduce the QuSquare suite and provide detailed descriptions of each benchmark. For each benchmark, we present the protocol for its implementation on a quantum computer, describe the parameters that can be selected by the user and the strategies used to choose them, describe the performance metrics used for quantitative evaluation, specify the reporting requirements, and analyze both the properties of the benchmark and those of the associated metrics. Finally, in Section IV, we present our conclusions and outline directions for future work.

II. BENCHMARK SUITE DESIGN PRINCIPLES

The QuSquare suite has been designed to evaluate the quality of quantum computers by assessing the noise in implementing general circuits and the ability to execute specific applications. Other aspects have not been included because noise level is the most critical characteristic for pre-fault-tolerant devices. Furthermore, evalu-

ating additional characteristics is meaningful only when comparing devices with similar error rates, making noise assessment the first and most important step. The suite was developed following the guidelines proposed by Acuaviva et al. [1], which outline principles for creating reliable quantum benchmarks.

- **Quality attributes:** The development of the QuSquare suite has been guided by key quality attributes that ensure the reliability of the benchmark suite. These include *relevance*, which guarantees that the benchmark suite targets meaningful workloads and captures performance aspects that are significant for quantum computation; *reproducibility*, which is achieved through all benchmark definitions, configurations, execution procedure are clearly and well defined, ensuring that results can be independently reproduced by any user or provider; *fairness*, which ensures impartial comparison across different technologies and mitigates bias toward specific architectures; and *scalability*, which enables the performance of quantum computers with a large number of qubits to be measured.

- **Compilation rules:** Defining compilation rules is crucial to ensure a fair comparison between quantum computers. The QuSquare suite focuses on evaluating the peak performance of each quantum processor under optimal compilation settings. The following compilation rules are allowed:

- *Classical subroutine simulation* is not allowed, unless explicitly specified by the benchmark. All circuits must be executed on quantum hardware without replacing quantum subroutines with classically simulated equivalents.
- *Circuit equivalence transformations* are allowed, provided that the equivalent circuit produces the same final quantum state. For instance, approximate circuit transformations are not allowed. Circuit cancellation is allowed, enabling the elimination of subcircuits that have no effect on the final quantum state, such as a unitary operation immediately followed by its inverse. Remove gates that do not affect the final measurements are not allowed.
- *Choosing physical qubits*: Any set of physical qubits can be selected for the execution of the benchmark, provided that the same qubits are used for every measurement or estimation associated with a given performance metric.
- *Low-level optimizations*: Low-level optimizations, such as pulse optimizations, are not allowed.

These compilation rules ensure that all benchmarks are compiled under the same conditions, avoiding artificial performance improvements. Both the

provider and the user must follow these compilation rules, unless explicitly specified otherwise by the benchmark.

- **Scope and abstraction levels:** The QuSquare suite is designed to operate at different levels of abstraction, covering both system-level and application-level benchmarks. At the system-level, the suite evaluates hardware capabilities such as entanglement generation and Clifford gate implementation accuracy. At the application level, it assesses the performance of application algorithms, such as Hamiltonian simulation and quantum machine learning tasks, reflecting the practical computational power of the quantum hardware.
- **Reporting requirements:** The final report of each benchmark is essential to ensure reproducibility and transparency of the benchmark suite. To this end, every benchmark execution must include:
 - Information about the hardware device used.
 - The transpiled quantum circuit executed on the device.
 - The set of physical qubits employed for each circuit execution.
 - The calibration data corresponding to the time of each circuit execution.
 - The compilation configuration and settings applied to each circuit.
 - All selected benchmark parameters and their corresponding values.

Additional reporting requirements specific to each test will be detailed in subsequent sections.

- **Error correction and mitigation rules:** The use of error mitigation and error correction is optional. However, whenever such techniques are applied, their implementation must be explicitly documented, and results must be reported both with and without error correction or mitigation to ensure transparency and enable fair comparison across devices. The specific technique employed, along with all relevant configuration details, must also be reported.

III. DESCRIPTION OF THE BENCHMARK SUITE

The QuSquare suite consists of four benchmarks: Partial Clifford Randomized, Multipartite Entanglement, TFIM Hamiltonian Simulation, and Data Re-uploading QNN. The first two benchmarks evaluate quantum hardware at the system level, while the latter two it at the application level.

Each benchmark is organized into three subsections: *Background and motivation*, which outlines the theoretical foundations and relevance of the benchmark in the quantum computing field; *Benchmark description*, which provides stepwise instructions for executing the benchmark on a quantum processor, describes how benchmark parameters should be selected, explains the strategies employed to execute it, defines the metric, and specifies the reporting requirements to ensure reproducibility and transparency of the benchmark; and *Benchmark property analysis*, which discusses the properties that the benchmark satisfies.

A. Partial Clifford Randomized Benchmark

1. Background and motivation

The N -qubit Clifford group [41], denoted as \mathbb{C}_N , consists of unitary operations that normalize the N -qubit Pauli group \mathcal{P}_N . Formally, this means that any Clifford operation $C \in \mathbb{C}_N$ maps a Pauli operator $P \in \mathcal{P}_N$ to another Pauli operator under conjugation:

$$\forall C \in \mathbb{C}_N, \quad CPC^\dagger \in \mathcal{P}_N, \quad \forall P \in \mathcal{P}_N. \quad (1)$$

Typical examples of Clifford gates that are not in the Pauli group include the Hadamard (H), the phase gate ($S = \sqrt{Z}$), the controlled-NOT (CNOT), the SWAP, and the i SWAP gates. Notably, the subgroup $\{H, S, \text{CNOT}\}$ is sufficient to generate the full Clifford group on any number of qubits. The number of elements in the N -qubit Clifford group is given by [42]:

$$|\mathbb{C}_N| = 2^{N^2+2N} \prod_{j=1}^N (4^j - 1), \quad (2)$$

which, despite being finite, grows exponentially with the number of qubits.

The Clifford group is particularly significant due to the Gottesman-Knill theorem [43], which states that quantum circuits composed solely of Clifford gates and measurements in the Pauli basis can be efficiently simulated on a classical computer in polynomial time. Consequently, Clifford circuits alone do not provide a quantum computational advantage over classical computation. To achieve universal quantum computation, a gate set must include at least one non-Clifford gate, such as the T gate ($T = \sqrt{S}$).

Despite their limited computational power, Clifford gates play a fundamental role in quantum computing. They are essential for:

- **Quantum error correction:** Stabilizer codes rely on Clifford operations for encoding, syndrome extraction, and decoding [44].
- **Classical shadows:** Classical shadows is a technique for estimating many observables from few

copies of a quantum state using randomized measurements [45]. These measurements are typically based on unitary transformations drawn from ensembles such as local or global Clifford unitaries [45, 46], which are widely used due to their efficient implementation and favorable theoretical properties.

- **Quantum cryptography and key distribution:** Many cryptographic protocols, such as entanglement distillation [47], Six-State Protocol [48], and Quantum Secret Sharing Scheme [49], leverage Clifford operations.
- **Quantum benchmarking:** An important property of Clifford gates is that they form a unitary 3-design. This property makes them particularly useful for benchmarking quantum devices. Techniques such as randomized benchmarking [50] use Clifford gates to characterize error rates in quantum gate implementations.
- **Quantum circuits:** Although Clifford operations alone are not universal, they provide the essential framework upon which arbitrary unitaries are constructed when combined with a non-Clifford gate such as T . In practice, this decomposition is particularly relevant for real quantum devices, where Clifford gates are typically implemented with high fidelity and used as the fundamental calibrated primitives, while non-Clifford gates are synthesized or injected as higher-level resources to achieve full universality.

In this work, we focused on Randomized Benchmarking (RB) protocols to assess how accurately a quantum computer implements Clifford gates. RB encompasses a broad class of methods that utilize random circuits of varying depths to quantify the error rates in a given gate set. Initially developed in the mid-to-late 2000s [50–52], RB was designed to overcome key limitations of quantum process tomography [53, 54]. Over time, numerous distinct RB protocols have emerged, each with specific applications, strengths, and limitations. Some major families of RB protocols include: *Standard RB* [55], *Native Gate RB protocols* [37, 56–59], *RB for General Groups* [37, 60, 61], *Simultaneous RB* [62], *Interleaved RB* [63], *Cycle Benchmarking* [64], *Purity Benchmarking protocols* [65, 66] and *RB protocols for Non-Markovian Errors* [37, 67]. Despite their structural similarities, these protocols measure different error characteristics.

In this benchmark, we utilize a slight modification of a recently proposed RB protocol known as *Binary Randomized Benchmarking* (BiRB)[57], which is based on Direct Fidelity Estimation (DFE) [68] method, and serves for measuring error rates in Clifford gates. Notably, BiRB falls within the category of *Native Gate RB*

protocols, which are specifically designed to benchmark layers of gates sampled from a distribution.

The BiRB protocol presents several advantages over other RB protocols, which motivate its selection for this benchmark:

- **Scalability:** BiRB does not require mirror circuits, stabilizer state preparation, or complex stabilizer state measurements, unlike many other RB protocols that measure similar error quantities, such as Direct RB [56] or Clifford Group RB [55]. The only additional overhead, beyond the implementation of the Clifford gates whose errors are to be characterized, consists of the measurement in the Pauli basis, which can be performed with a single layer of single-qubit gates. This scalability allows us to evaluate Clifford gate error rates on larger quantum processors.
- **Robustness to State Preparation and Measurement (SPAM) Errors:** BiRB is designed to mitigate the influence of SPAM errors, thereby allowing an accurate characterization of the errors in the implementation of Clifford gates, while minimizing the impact of other error sources that could otherwise lead to misleading results.

2. Benchmarking description

In this benchmark, our objective is to evaluate the largest portion of a Clifford unitary that the quantum computer can implement with high fidelity. To this end, we estimate the mean error rate of circuit layers corresponding to a fraction of circuits that realize global random Clifford unitaries, which we refer to as *μ -fraction random Clifford circuits*, or simply *μ -fraction circuits*. The central idea is to report the largest fraction of the Clifford circuit –ideally the entire circuit– that the device can implement with fidelity exceeding a given threshold. We now provide a detailed definition of the μ -fraction random Clifford circuits and describe the quantity used to characterize their noise on a quantum device.

μ -fraction random Clifford circuits.— A μ -fraction random Clifford circuit on N qubits is defined by the following construction. First, a random Clifford unitary is sampled uniformly from the N -qubit Clifford group and transpiled into a circuit implementation of depth d , composed of Clifford gates. Since such implementations are not unique, we typically select one that is expected to minimize errors on the target device for example, one with minimum depth or fewer two-qubit gates. We then compute $d_\mu = \lceil \mu d \rceil$, where $\mu \in (0, 1]$ specifies the fraction of the circuit to be retained. An integer s is chosen uniformly at random from the interval $[0, d - d_\mu]$, and the μ -fraction random Clifford circuit is defined as the contiguous subsequence of gates between depths s and $s + d_\mu$ of the original circuit.

Estimating the average entanglement infidelity of μ -fraction circuits.— The quantity of interest, denoted by ϵ_μ , is defined as one minus the *decay rate* with circuit depth of the fidelity of μ -fraction random Clifford circuits acting on N qubits. This quantity is interesting because when stochastic Pauli errors are the dominant source of error, ϵ_μ is approximately equal to the average entanglement infidelity of μ -fraction random Clifford circuits

$$\varepsilon_\mu = 1 - \mathbb{E}_C F_e(\mathcal{U}(C), \Phi(C)), \quad (3)$$

where C are μ -fraction random Clifford circuits, \mathcal{U} is the superoperator of the perfect implementation of a circuit, and Φ the imperfect implementation. The precise definition of ϵ_μ follows from the following considerations. The average entanglement fidelity of d layers of μ -fraction random Clifford circuits C_d is given by

$$\bar{F}_d = \mathbb{E}_{C_d} F_e(\mathcal{U}(C_d), \Phi(C_d)). \quad (4)$$

Similar to the BiRB benchmark [57] with Ω -distributed circuits, the average fidelity \bar{F}_d decays exponentially with

circuit depth when stochastic Pauli noise is the dominant noise source, as demonstrated in Appendix A, i.e. $\bar{F}_d \approx Ap_{rc}^d$, for constants A and p_{rc} . The average error rate of layers of μ -fraction random Clifford circuits is then defined as

$$\epsilon_\mu = \frac{4^N - 1}{4^N} (1 - p_{rc}). \quad (5)$$

We choose ϵ_μ to be this particular rescaling of p_{rc} because p_{rc} corresponds to the effective polarization of a μ -fraction random Clifford circuit –i.e., the polarization in a depolarizing channel that would give the same fidelity decay– and so ϵ_μ is the effective average infidelity of a μ -fraction random Clifford circuit layer. Additional information on these quantities can be found in Refs. [56, 57, 69].

It is important to note that when $\mu = 1$, we are considering the complete Clifford group and ε_μ measures the *average gate set infidelity* (AGSI), analogous to Standard RB.

a. Stepwise instructions. The detailed description of the benchmark is presented in the following box, and a flowchart of the procedure is shown in Figure 1.

Protocol 1: Partial Clifford Randomized Benchmark protocol

Initialization: Choose the number of qubits to be tested, N , and the value of μ based on prior knowledge.

Return: The largest value of μ for which the estimation r_μ of the infidelity ϵ_μ remains less than or equal to 0.1.

Procedure:

1. **Choosing Parameters:** Select M , the maximum number of μ -fraction circuits layers (depths), and define a sequence of positive integers $m = \{m_1, \dots, m_M\}$ such that $m_i < m_j$ for $i < j$, representing the different layer depths of the μ -fraction circuits. Additionally, define another sequence of positive integers $n = \{n_1, \dots, n_M\}$, where each n_i specifies, for the depth m_i , the number of times different m_i layers of μ -fraction circuits are selected. Finally, choose l , the number of times each layered circuit is executed.

2. **Construct the circuits and get the data:**

For each i from 1 to M :

(a) For each j from 1 to n_i :

i. Sample a uniform random N -qubit Pauli string $P \in \{\pm(I, X, Y, Z)^{\otimes N}\} \setminus \{\pm I^{\otimes N}\}$, i.e., a Pauli operator with a global sign, different from the identity. Then, generate a uniformly random state $|\psi(P)\rangle$ from the set of tensor-product stabilizer states stabilized by P , such that $P|\psi(P)\rangle = |\psi(P)\rangle$. Compute L_0 , a circuit of single qubit gates that prepares $|\psi(P)\rangle$, such that $L_0|0\rangle^{\otimes N} = |\psi(P)\rangle$.

ii. Select m_i Clifford unitaries U_1, \dots, U_{m_i} randomly from the N -qubits Clifford group \mathbb{C}_N . For each Clifford unitary, generate the most efficient quantum circuit, composed of Clifford gates and optimized for the specific quantum processor, obtaining the circuits C_1, \dots, C_{m_i} , with depths d_1, \dots, d_{m_i} . For each circuit C_k , select uniformly randomly a number s_k from the interval $[0, \lfloor d_k(1 - \mu) \rfloor]$. The μ -fraction random Clifford circuit L_k is defined by the contiguous sequence of gates from depth s_k to $s_k + \lfloor d_k\mu \rfloor$ within the original circuit C_k .

iii. Compute classically the final layer L_f of single-qubit gates that transform

$$P' = U(L_{m_i}) \cdots U(L_1) P U(L_1)^{-1} \cdots U(L_{m_i})^{-1} \quad (6)$$

into a tensor product of Z and I operators, where $U(L)$ denotes the unitary implemented by circuit L .

- iv. Prepare the $|0\rangle^{\otimes N}$ state on the processor and construct the circuit by appending the sequence $L = L_0 \cdots L_{m_i} L_f$ to it.
- v. Run the circuit L and measure in the computational basis obtaining l eigenvalues of P' , that will lie in $\{-1, 1\}$. We call α_{ij} the mean of these l values obtained.
- (b) Compute the mean $f_i = \frac{1}{n_i} \sum_{j=1}^{n_i} \alpha_{ij}$.

3. **Fit the data to the model:** Fit the data obtained in previous step to an exponential model of the form

$$f_i = Ap_{rc}^{m_i}, \quad (7)$$

where the parameters A and p_{rc} are determined by performing a linear regression on the logarithm of the model.

4. **Compute r_μ :** Compute an estimation of ϵ_μ :

$$r_\mu = \frac{4^N - 1}{4^N}(1 - p_{rc}).$$

5. **Check r_μ conditions:** If $r_\mu > 0.1$, select a smaller value of μ and repeat the procedure from Step 2. If $r_\mu \leq 0.1$ and $\mu = 1$, return $\mu = 1$ together with r_μ . If $r_\mu < 0.1$ and $0.1 - r_\mu > 0.01$, increase μ and repeat the procedure from Step 2, else, return the current values of μ and r_μ .

Further details regarding the validity of Steps 2 and 3 can be found in Ref. [57].

b. *Selection of parameters and strategies.* The strategies and parameters restrictions are as follows:

- The first step, namely the choice of parameters, is left to the user; however, in order to ensure precise and accurate results, we provide several recommendations. Since our protocol employs the BiRB structure to estimate the infidelity of the circuits, one can refer to the original BiRB work for guidance on parameter selection. As stated there, it is statistically optimal to maximize the number of random circuits while setting the number of shots per circuit to one. In practice, however, this approach may be impractical due to the time required to generate and load a large number of distinct circuits onto the processor. For this reason, it is acceptable to instead use fewer circuits with more shots each. Although we do not prescribe a fixed number of circuits or shots, further guidance on their selection can be found in Appendix B of [57]. In practice, we recommend that the product of the number of circuits and the number of shots exceed 10^5 in order to achieve low variance and thus obtain precise estimates. Another parameter of interest is the number of layer depths to be tested. As established in BiRB work, two depths are sufficient, provided that they are separated by $O(\log(1/p))$, where p is the decay parameter estimated in Step 3 and is related to the processor fidelity. Since we are

interested in executing circuits with relatively high fidelity, this separation is small, i.e., of order $O(1)$. We therefore recommend using at least two depths, with their values separated by at least three layers.

- We do not prescribe a specific method for transpiling each Clifford unitary before extracting the corresponding portion of the circuit. Instead, given a device with a particular topology and native gate set, we leave it to the user to determine the most suitable transpilation strategy. This includes selecting the qubits on which the algorithm will run and optimizing the resulting circuit implementation. The only required conditions are as follows:
 1. For a given N and μ , all circuits of different depths must be transpiled and executed on the same set of qubits.
 2. The transpilation process must be performed independently for each layer. This allows for optimizations within the transpilation of individual layers, but not across the joint implementation of all layers.
 3. Prior to truncation, the transpilation of a unitary into a quantum circuit must yield a circuit that exactly realizes the target unitary transformation. Moreover, the native gate set into which the circuit is transpiled must consist solely of Clifford gates, ensuring that the truncated circuit continues to implement a Clifford unitary. If this condition cannot

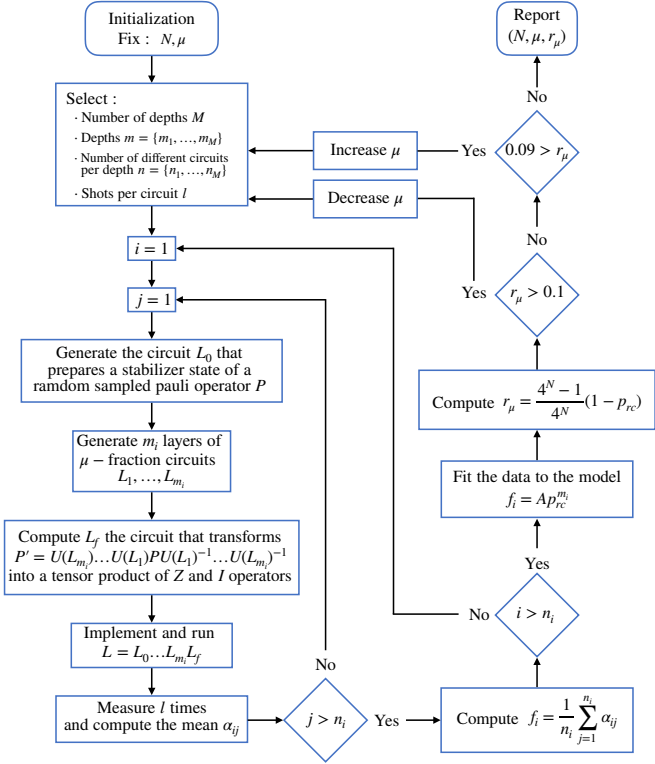


FIG. 1 Flowchart of the Partial Clifford Randomized Benchmark. The diagram summarizes the steps described in Protocol 1, including parameter initialization, circuit generation and execution, measurement estimation, and the iterative update of μ based on the estimated infidelity r_μ .

be readily fulfilled, an alternative approach is to construct an intermediate representation of the circuit composed exclusively of Clifford gates, perform the truncation within this representation, and subsequently transpile the resulting circuit into native gates, while aiming to preserve a circuit depth comparable to that obtained by directly truncating the native circuit.

- The fifth step of the algorithm does not prescribe a specific strategy for increasing or decreasing μ when the conditions for returning to Step 2 are met. This choice is left to the user, who should explicitly report the strategy employed. We recommend adopting a binary search over the variable μ , as it requires only a logarithmic number of steps in the desired precision.
- To reduce the number of different values of μ that must be tested when running the benchmark with N qubits to achieve an infidelity close to 0.1, it is advantageous to heuristically estimate an appropriate initial value of μ . Several strategies can be employed for this purpose. For example, one may select a value of μ close to that obtained for $N - 1$

Parameters and strategies	Rules
M	≥ 2
$m = \{m_1, \dots, m_M\}$	$m_M - m_1 \geq 3$
$n = \{n_1, \dots, n_M\}$	$n_i \cdot l \geq 10^5, \forall n_i \in n$
l	$n_i \cdot l \geq 10^5, \forall n_i \in n$
Unitary transpilation	Each unitary is independently transpiled into Clifford gates prior to truncation.
Total circuit transpilation	The circuit resulting from the concatenation of layers cannot be optimized.
Set of qubits	All circuits must be transpiled to target the same set of qubits.
Select initial μ	While the choice is left to the user, leveraging information from the benchmark execution with one fewer qubit or from classical simulations is recommended.
Strategy to update μ	The choice is left to the user; however, a binary search is recommended.

TABLE I Summary of the parameters and strategies for the Partial Clifford Randomized Benchmark. The table includes the rules for selecting the parameters M , $m = \{m_i\}_{i=1}^M$, $n = \{n_i\}_{i=1}^M$, and l . Furthermore, it includes the rules for unitary and total circuit transpilation, the qubit-selection requirements, and the recommended strategies for choosing the initial value of μ and updating it during the benchmark.

qubits, or, if N is sufficiently small, perform classical simulations of the device to estimate a suitable value. After testing the initial estimate on the target device, the user may then refine μ using any of the adjustment strategies discussed previously.

Table I presents a summary of the parameters, strategy restrictions, and recommendations associated with this benchmark.

c. Metric definition. The metric reported by this benchmark, for a given number of qubits N , is the triple (N, μ_{\max}, r_μ) , where $0 \leq \mu_{\max} \leq 1$ denotes the maximum value of μ for which a μ -circuit can be executed on a processor with N qubits such that the resulting infidelity r_μ is less than or equal to 0.1, within a tolerance of 0.01.

d. Reporting requirements. For the Partial Clifford Benchmark, experimental teams or hardware providers are required to submit a comprehensive report that includes the elements specified in Section II, as well as the following additional items:

- The random unitaries selected in Step 2(a)ii of Protocol 1, prior to transpilation and truncation.

- The strategy employed to generate the μ -fraction circuits in Step 2(a)ii of Protocol 1; that is, the method by which the Clifford unitary is translated into a circuit and the procedure used to extract the corresponding portion of the circuit.
- The values of f_i computed in Step 2b of Protocol 1 for each circuit depth m_i .
- The tuples (μ, r_μ) computed each time Protocol 1 reaches Step 5.

3. Benchmark and metric property analysis

In this section, we examine which of the benchmark and metric properties defined in [1] are satisfied. We begin by analyzing the benchmark properties, which we consider this process until getting the result from the quantum computer.

1. **Relevance:** As established, Clifford gates play a central role in quantum computation, and their reliable implementation constitutes a critical step toward the realization of fault-tolerant quantum computing. Consequently, since this benchmark overcomes the limitations of existing randomized benchmarking protocols in assessing error rates on large-scale quantum processors in a fair and architecture-independent manner, we consider it to be highly relevant.
2. **Reproducibility:** If the benchmark is executed on the same quantum computer with the same configuration, and a sufficiently large number of Clifford circuits and shots per circuit are sampled, the reported results will be statistically consistent. Any variations between runs will be limited to statistical fluctuations that depend only on the number of sampled circuits, the number of implemented layers, and the number of shots performed.
3. **Fairness:** The benchmark is parameterized by several user-selectable options, such as the transpilation strategy or the choice of gate set used to implement the circuit. This flexibility enables the user to obtain the best possible results while avoiding fixed rules that apply only to specific devices. In contrast to other benchmarks based on RB protocols that focus on circuits built from specific gates, this benchmark evaluates the performance of quantum processors on a general task –implementing a Clifford unitary, or a portion thereof– without imposing assumptions about the circuit topology or native gate set. These choices are left to the user, enabling a fair comparison of devices based on their ability to perform this task, independent of their architecture.

4. **Verifiability:** The benchmark is well defined, with strong support from proven theorems established in other benchmarks such as BIRB, as well as from the analytical results derived for our class of circuits in this section and in the appendices. In addition, we provide practical recommendations for selecting the parameters of the benchmark, ensuring that the reported results are accurate and reliable.

5. **Usability:** By relying on Clifford circuits, we ensure that all steps requiring classical computations can be performed efficiently in polynomial time, with no prohibitively large constants or exponents. For the quantum part of the benchmark, the circuits are implemented on a user-chosen number of qubits, with their depth determined by one of the benchmark parameters. This design makes the protocol straightforward to implement on quantum processors of arbitrary size and connectivity.

Using the data obtained from the quantum device, the metric defined in Sec. III A 2c is computed classically. This metric is analyzed with respect to the following properties, as shown in Table IV:

1. **Practical:** The metric is practical, as computing sample means and fitting the model via linear regression is computationally scalable. Moreover, the number times we recompute r_μ scales logarithmically with the desired precision, further ensuring overall efficiency and scalability.
2. **Repeatable:** The metric is repeatable because the computations performed on the measurement data obtained from the quantum processor are fully deterministic.
3. **Reliable:** The metric is reliable because a quantum processor with lower noise should be capable of implementing deeper circuits, which in turn implies that it can realize circuits with a larger value of μ_{\max} compared to a noisier device.
4. **Consistent:** No hardware-specific bias is introduced, and the metric is computed identically across all architectures. Therefore, the metric is consistent.

B. Multipartite Entanglement Benchmark

1. Background and motivation

Entanglement is one of the fundamental resources in quantum mechanics and plays a central role in quantum computation. Indeed, entanglement has been demonstrated to be a fundamental resource enabling quantum algorithms to overcome classical computation [70]. The Greenberger–Horne–Zeilinger (GHZ) state [71] is an entangled quantum state that is useful as a resource for

a variety of applications, including quantum computing [72], quantum metrology [73], quantum teleportation [74], and other tasks. Due to technological advances, GHZ states have been generated across various platforms, including trapped ions [75, 76], superconducting circuits [77–80], Rydberg atom [81, 82], photonic systems [83, 84], and silicon-based architectures [85].

The N -qubit GHZ state is defined as

$$|\text{GHZ}_N\rangle = \frac{1}{\sqrt{2}} (|0\rangle^{\otimes N} + |1\rangle^{\otimes N}).$$

Several quantum algorithms have been proposed to generate GHZ states [75, 86–89]; however, the most efficient circuit for preparing a GHZ state strongly depends on the characteristics of the quantum processor, its native gate set, qubit connectivity topology, and other hardware-specific aspects. Once a circuit designed to prepare the GHZ state is implemented on a given processor, it is essential to evaluate how accurately the state is prepared. This accuracy can be quantitatively assessed through the quantum state fidelity.

The quantum state fidelity provides a quantitative measure of how close two quantum states are. It can therefore be used to assess how accurately a target quantum state has been prepared. The fidelity of a quantum state, given by its density matrix ρ , with respect to the known GHZ state is defined as

$$\mathcal{F} = \langle \text{GHZ}_N | \rho | \text{GHZ}_N \rangle.$$

The fidelity reaches a value of 1 when ρ is identical to the pure state $|\text{GHZ}_N\rangle\langle\text{GHZ}_N|$. There are various methods to estimate the fidelity such as parity oscillations [76, 90], multiple quantum coherences (MQC) [91], quantum state tomography [78], classical shadow tomography [92], shadow overlap [93] or Direct Fidelity Estimation (DFE) [68]. Among these, one of the most scalable approaches to measuring the fidelity of a quantum state is Direct Fidelity Estimation (DFE), whose complexity –particularly for states such as the GHZ state– is independent of the number of qubits. This method involves performing measurements with respect to Pauli observables that can be efficiently computed classically. The required Pauli-basis measurements can be efficiently implemented on a quantum processor by applying a single-qubit Pauli gate to each qubit, followed by a measurement in the computational basis, ensuring that the procedure does not increase the circuit depth. Furthermore, the classical computation of the employed Pauli operators is efficient, as the simulations involve only Clifford circuits, and the Gottesman–Knill theorem [94] guarantees classical efficiency. Given its advantages for fidelity estimation, Direct Fidelity Estimation is employed in this benchmark.

Direct Fidelity Estimation.— Direct fidelity estimation is a technique that allows us to compute the fidelity of an arbitrary quantum state by performing at most $O(2^N)$ measurements in the Pauli basis. However, when the

states under consideration are stabilizer states, such as the GHZ state, the number of required measurements depends only on the desired precision of the fidelity estimation. The procedure to estimate the fidelity between a given pure state $|\psi\rangle$ and a classical unknown density matrix state ρ is described below.

Let $\mathbb{P}_N = \{P_i \mid i = 1, \dots, 2^{2N}\}$ denote the set of all possible Pauli strings on N qubits, and define $p_i = \langle \psi | P_i | \psi \rangle$, which is computed classically. The goal is to construct an estimator for the fidelity, denoted by Y , that satisfies

$$\Pr(|Y - \mathcal{F}(\rho, |\psi\rangle\langle\psi|)| \leq \varepsilon) \geq 1 - \delta, \quad (8)$$

where ε and δ denote the maximum estimation error allowed and the confidence level of the estimator, respectively. The number of measurements required depend on these two parameters. The estimation of the fidelity is computed using the following procedure:

1. Choose $\ell = \lceil 8/(\varepsilon^2 \delta) \rceil$ Pauli strings from \mathbb{P}_N randomly, with the probability of selecting equal to $p_i^2/2^N$.
2. For each of the Pauli strings P_i chosen, prepare the state ρ on the quantum computer m_i times, where

$$m_i = \left\lceil \frac{8}{p_i^2 \ell \varepsilon^2} \log \left(\frac{4}{\delta} \right) \right\rceil.$$

Each copy of the state ρ is measured in the basis of the Pauli strings P_i , obtaining measurement outcomes $A_{ij} \in \{1, -1\}$ for $j = 1, \dots, m_i$.

3. Compute Y with these results

$$Y = \frac{1}{\ell} \sum_{i=1}^{\ell} \left(\frac{1}{m_i p_i} \sum_{j=1}^{m_i} A_{ij} \right).$$

The total number of times the state ρ must be prepared and measured in a Pauli basis on the quantum computer is $m = \sum_{i=1}^{\ell} m_i$, while the number of p_i values that need to be computed classically is ℓ .

When the state $|\psi\rangle$ is a stabilizer state, such as the case of the GHZ state, the p_i are either 0 or 1 for all i . Therefore, there are 2^N Pauli strings with selection probability 2^{-N} , while all others have zero probability. Furthermore, the value of m becomes independent of the number of qubits, and both ℓ and m remain significantly smaller. To preserve the bound given in Eq. (8), the number of Pauli strings to be selected is given by $\ell = \lceil \frac{8 \log(4/\delta)}{\varepsilon^2} \rceil$, and $m_i = 1$. Therefore, the total number of measurements is $m = \lceil \frac{8 \log(4/\delta)}{\varepsilon^2} \rceil$, which does not depend on N . See the Ref. [68] for more details.

2. Benchmark description

The Multipartite Entanglement Benchmark aims to report the largest GHZ state with genuine multipartite entanglement that can be generated on the quantum processor. It provides standardized information about the size of the qubit cluster that can be entangled in a quan-

tum state relevant for various applications, and which is, in principle, both straightforward to generate and measure.

a. Stepwise instructions A detailed description of the benchmark is provided in the following box, and a flow chart of the procedure is shown in Figure 2.

Protocol 2: Multipartite Entanglement Benchmark protocol

Initialization: Set $N = 2$, and fix ε and δ .

Return: Maximum number of qubits that can generate the GHZ state with fidelity greater than $1/2$.

Procedure:

1. **Selection of Pauli strings:** Since the quantum state $|\text{GHZ}_N\rangle$ is a stabilizer state, and it can be expressed as $|\text{GHZ}_N\rangle = G_N |0\rangle$, where G_N is a Clifford unitary. Therefore, there exist exactly 2^N Pauli strings P for which the expectation value

$$\langle \text{GHZ}_N | P | \text{GHZ}_N \rangle = 1,$$

while the expectation value vanishes for all other Pauli strings. The set of Pauli strings with nonzero expectation values, from which we sample to perform direct fidelity estimation, is given by

$$\mathcal{T} = \left\{ G_N P G_N^\dagger : P \in \bigotimes_{i=1}^N S_i, \quad S_i \in \{I, Z\} \setminus \{I^{\otimes N}\} \right\}.$$

Notice that the identity operator $I^{\otimes N}$ is excluded to avoid bias in the fidelity estimation. The selection procedure consists of choosing

$$\ell = \left\lceil \frac{8 \log(4/\delta)}{\varepsilon^2} \right\rceil$$

Pauli strings $\{P_i\}_{i=1}^\ell$ uniformly at random from the set \mathcal{T} . This sampling can be performed efficiently on a classical computer, as all the gates involved are Clifford operators.

2. **Construct the circuit:** Design the most efficient quantum circuit \mathcal{C} that the provider can implement on the target processor to prepare the N -qubit GHZ state.
3. **Quantum data acquisition:** For each i from 1 to ℓ , execute the quantum circuit \mathcal{C} on the quantum computer and perform a single measurement in the basis corresponding to each Pauli string P_i selected in Step 1. Each measurement yields outcomes $A_i \in \{-1, 1\}$. If the quantum processor only allows measurements in the computational basis, apply an additional layer of single-qubit gates to transform the measurement basis accordingly before performing the measurement.
4. **Compute the estimator of the fidelity:** Using the data obtained in the previous step, compute the estimator Y of the fidelity $\mathcal{F}(|\text{GHZ}_N\rangle\langle \text{GHZ}_N|, \rho)$ between the GHZ state $|\text{GHZ}_N\rangle$ and the state ρ prepared by the quantum computer during the execution of the circuit \mathcal{C} , as follows:

$$Y = \frac{1}{\ell} \sum_{i=1}^{\ell} A_i.$$

5. **Evaluate fidelity:** If the fidelity estimator minus the allowed error, $Y - \varepsilon$, exceeds $1/2$, this implies that, with probability $1 - \delta$, the fidelity surpasses $1/2$, and the test for N qubits was successful. Repeat the procedure from Step 1 for successive values of N and report the largest N such that the test is successful.

Parameters and strategies	Rules
δ	≤ 0.1
ε	≤ 0.05
Strategy for updating N	The choice is left to the user; however, a binary search is recommended.

TABLE II Summary of the parameters and strategies for the Multipartite Entanglement Benchmark. The table includes the rules for the confidence level δ and ε , and a recommended strategy for updating the number of qubits N .

a

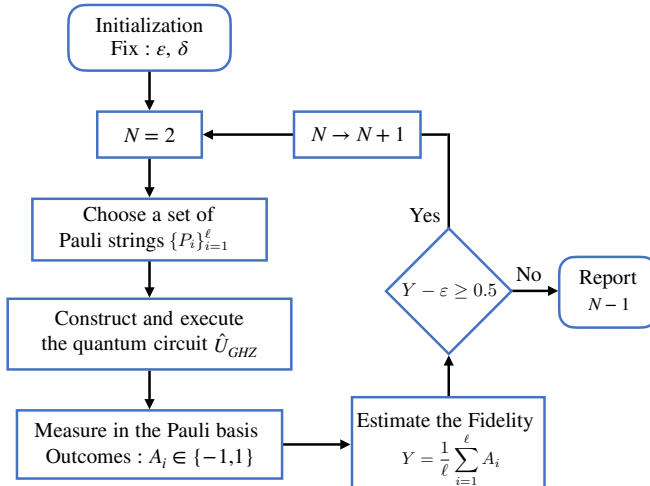


FIG. 2 Flowchart of the Multipartite Entanglement Benchmark. The diagram summarizes the steps described in Protocol 2, including the selection of Pauli strings, the construction and execution of the quantum circuit, the computation of the fidelity estimator, and the iterative increase of the number of qubits N .

b. Selection of parameters and strategies. The benchmark requires the selection of two parameters ε and δ and the strategy for updating N . Upper bounds for ε and δ are provided to ensure accurate results. Specifically, it is recommended to set $\varepsilon \leq 0.05$ to maintain an estimation error below 5%, with a confidence level of at least 90% (i.e., $\delta \leq 0.1$). With these settings, fewer than $2 \cdot 10^4$ measurement shots are required, an amount manageable by most current quantum processors. The strategy for updating the parameter N is left to the user, although a binary search procedure is recommended. A summary of the parameters and execution strategies for this benchmark is provided in Table II.

c. Metric definition. The purpose of this metric is to quantify the maximum number of qubits for which a quantum computer can generate entanglement in a GHZ state. This provides an indication of the device's capability to produce genuine multipartite entanglement. The metric is defined as the size of the largest GHZ state that the provider can prepare with high confidence and with fidelity greater than 1/2 [90, 95].

d. Reporting requirements. For the Multipartite Entanglement Benchmark, experimental teams or hardware providers are required to submit a comprehensive report that includes the elements specified in Section II, as well as the following additional items:

- A detailed description of the quantum circuit used to generate the GHZ state.
- The resulting fidelity for each qubit number, corresponding to the Y value computed in Step 4 of Protocol 2.

3. Benchmark and metric property analysis

An analysis of the properties satisfied by this benchmark is presented below.

- 1. Relevance:** This benchmark is particularly relevant because the prepared state corresponds to a widely used quantum state in various applications, as discussed in Section III B 1. Moreover, this state is especially relevant in the current era of quantum computing, as it is both feasible to generate and practically useful. In addition, the benchmark provides valuable insight into the overall quality of a quantum processor, offering an estimate of the number of functional qubits that can be reliably employed for computation.
- 2. Reproducibility:** This benchmark is reproducible provided that the same qubits are selected for the test and the same circuit is used across different runs. Minor variations in the reported results are expected due to hardware calibration and statistical fluctuations; however, the reported metric N across independent executions should not differ by more than one.
- 3. Fairness:** The benchmark is parameterized by several user-defined options, including the specific circuit used to prepare the target state, the transpilation strategy, the choice of native gate set, and the selection of qubits on which the circuit is executed. This flexibility allows users to obtain the best possible performance from each device while avoiding rigid rules tailored to particular architectures. By leaving these choices to the user, the benchmark enables a fair comparison of quantum processors based solely on their ability to perform the prescribed task, irrespective of their underlying hardware design.
- 4. Verifiability:** The benchmark procedure is well-defined, as it is grounded in rigorously established mathematical tools. The lower bounds provided for the benchmark parameters ensure confidence in the measured results through statistical analysis. Furthermore, the methodology is transparent and

precisely specified, with each step clearly stated to avoid ambiguity or subjective interpretation.

5. **Usability:** This benchmark is practically feasible because the target state to be prepared on the quantum processor is a well-studied stabilizer state, for which numerous efficient preparation circuits are known and can be readily implemented on most current quantum architectures. Moreover, the generation of random Pauli matrices on a classical computer is computationally efficient under the specified procedure. The number of Pauli operators and measurement shots required to estimate the state fidelity scales quadratically with the desired precision, allowing the benchmark to achieve low error rates while remaining computationally tractable.

Using the data obtained from the quantum device, the metric defined in Sec. III B 2c is computed classically. This metric is analyzed with respect to the following properties, as shown in Table IV:

1. **Practical:** The metric is practical because computing sample means is computationally scalable. Moreover, the number of times we need to run the benchmark and evaluate the sample mean to calculate the metric grows only linearly with the number of qubits.
2. **Repeatable:** The metric is repeatable because both the computation of the sample mean and the procedure for determining whether to extend the benchmark to additional qubits are fully deterministic.
3. **Reliable:** When assessing the largest number of qubits for which a quantum computer can generate entanglement in a GHZ state, this metric is reliable, as it directly measures this quantity. However, this does not imply that the metric is reliable for comparing which device is better at generating entanglement more generally.
4. **Consistent:** No hardware-specific bias is introduced, and the metric is computed identically across all architectures. Therefore, the metric is consistent.

C. TFIM Hamiltonian Simulation Benchmark

1. Background and motivation

Hamiltonian simulation is a relevant application of quantum computing [96], which aims to reproduce the time evolution of quantum systems governed by a Hamiltonian \hat{H} . Specifically, given an initial state $|\psi(0)\rangle$, the objective is to efficiently approximate the evolved state $|\psi(t)\rangle = \hat{U}(t)|\psi(0)\rangle$ using a quantum circuit, where the time-evolution operator $\hat{U}(t)$ for a time-independent

Hamiltonian is described by $e^{-i\hat{H}t}$. This problem has a broad range of scientific and technological domains, including quantum chemistry [97–101], materials science [102–104], condensed matter physics [105, 106], among others.

Several quantum algorithms have been proposed to simulate Hamiltonian dynamics with different accuracy and resource requirements, including Trotter-Suzuki decomposition [107], quantum walk [108], linear combination of unitaries (LCU) [109], quantum signal processing (QSP) [110–112]. Among these, Quantum Signal Processing (QSP) stands out as a powerful technique, which we employ in this work.

Quantum Signal Processing (QSP) is a powerful quantum algorithm that enables the implementation of polynomial approximations of matrices using a sequence of single-qubit rotations controlled by an ancilla qubit [110–112]. In the context of Hamiltonian simulation, QSP can be used to approximate the time-evolution operator $e^{-i\hat{H}t}$ through a polynomial transformation of the Hamiltonian. This is achieved by employing the block encoding technique to embed the Hamiltonian \hat{H} into a larger unitary matrix

$$\hat{U}_H = \begin{pmatrix} \hat{H}/\alpha & * \\ * & * \end{pmatrix}, \quad (9)$$

where $*$ denotes matrix elements and α is a normalization factor. The block-encoding \hat{U}_H can be constructed using the Linear Combination of Unitaries (LCU) technique. This technique provides a method to implement block-encodings of non-unitary operators, such as Hamiltonians, by expressing them as a linear combination of K unitary operators:

$$\hat{H} = \sum_{i=1}^K \alpha_i \hat{U}_i, \quad (10)$$

where each \hat{U}_i is a unitary operator acting on the main system qubits and the coefficients α_i are real numbers. The LCU technique requires m ancillary qubits, where $m = \lceil \log_2 K \rceil$. To embed the Hamiltonian into a larger unitary matrix, we employ two operators known as \hat{U}_{Prep} and \hat{U}_{Select} .

The operator \hat{U}_{Prep} prepares m ancillary qubits in a superposition state that encodes the coefficients α_i of the Hamiltonian decomposition, while the operator \hat{U}_{Select} applies the unitary operators \hat{U}_i on s qubits conditioned on the state of the ancillary qubits. Here, s denotes the number of qubits needed to represent the Hamiltonian of interest. These operators are defined as follows

$$\hat{U}_{\text{Prep}}|0\rangle^{\otimes m} = \sum_i \sqrt{\frac{\alpha_i}{\alpha}} |i\rangle, \quad (11)$$

where $\alpha = \sum_i |\alpha_i|$. The operator \hat{U}_{Select} is described as follows

$$\hat{U}_{\text{Select}} = \sum_i^K |i\rangle\langle i| \otimes \hat{U}_i. \quad (12)$$

Using these two operators, the Hamiltonian can be embedded into a larger unitary matrix as

$$\hat{U}_H = \begin{pmatrix} \hat{H}/\alpha & * \\ * & * \end{pmatrix} = (\hat{U}_{\text{Prep}}^\dagger \otimes \mathbb{I}_{s \times s}) \hat{U}_{\text{Select}} (\hat{U}_{\text{Prep}} \otimes \mathbb{I}_{s \times s}). \quad (13)$$

Then, an extra ancillary qubit q_A is introduced to implement a sequence of single-qubit rotations that approximate the exponential function. The phase angles of these rotations are determined through classical processing.

To implement a polynomial function P of degree d on the block encoding defined in Eq. 13 using QSP, the polynomial must satisfy the following conditions

1. P has parity $d \bmod 2$.
2. $|P(x)| \leq 1$ for all $x \in [-1, 1]$.

The corresponding QSP operator acting on the block encoding of Eq. 13 is defined as

$$\hat{U}_{\text{QSP}} = \begin{pmatrix} P(\hat{H}/\alpha) & * \\ * & * \end{pmatrix} = \Pi_{\phi_0} \prod_{j=1}^d \hat{U}_H \Pi_{\phi_j}, \quad (14)$$

where $\Pi_{\phi_k} = e^{i\phi_k \Pi}$ with $k = 0, \dots, d$ are phase-controlled projectors acting on ancillary qubits q_A and q_m , $\Pi = 2|0\rangle\langle 0| - \mathbb{I}$ is a reflection, and $\phi = \{\phi_0, \phi_1, \dots, \phi_d\} \in \mathbb{R}$ are phases classically computed such that the upper left block of the unitary \hat{U}_{QSP} embed the target polynomial $P(\hat{H}/\alpha)$. The circuit implementing the unitary \hat{U}_{QSP} , as defined in Eq. 14, is shown in Fig. 4.

In the context of Hamiltonian simulation, the evolution operator $e^{i\hat{H}t}$ for a given t is approximated by a degree- d polynomial $P(t\hat{H})$ that satisfies

$$\|P(t\hat{H}) - e^{-i\hat{H}t}\|_2 \leq \epsilon_0, \quad (15)$$

where ϵ_0 denotes the tolerated error. However, since the exponential function does not possess a definite parity, it does not satisfy Condition 1. To overcome this issue, the exponential can be expressed as

$$e^{-ixt} = \cos(xt) - i \sin(xt) \quad (16)$$

and two separate polynomial approximations can be used: one even polynomial to approximate $\cos(xt)$ and one odd polynomial to approximate $\sin(xt)$, both of which have definite parity. The approximation of this polynomials can be done through the Jacobi–Anger expansion in terms of Chebyshev polynomials of the first kind. For $x \in [-1, 1]$, this expansion reads as

$$\begin{aligned} \cos(xt) &= J_0(t) + 2 \sum_{k=1}^{\infty} (-1)^k J_{2k}(t) T_{2k}(x), \\ \sin(xt) &= 2 \sum_{k=0}^{\infty} (-1)^k J_{2k+1}(t) T_{2k+1}(x), \end{aligned} \quad (17)$$

where $J_k(t)$ denotes the Bessel function of the first kind of order k and $T_k(x)$ denotes the Chebyshev polynomial

of the first kind of order k . Truncating each expansion at $k = d/2$ yields polynomial approximations $P_{\cos}(xt)$ and $P_{\sin}(xt)$, both with an error ϵ that depends on d . To implement QSP with these two polynomials, they must satisfy Condition 2. Since $\cos(xt)$ and $\sin(xt)$ are both bounded in magnitude by 1, and $P_{\cos}(xt)$ and $P_{\sin}(xt)$ are ϵ -approximations of these functions, the condition can be ensured by rescaling the polynomials as $P_{\cos}(xt)/(1+\epsilon)$ and $P_{\sin}(xt)/(1+\epsilon)$. This rescaling increases the approximation error of both polynomials by at most a factor of 2. Taking this into account, in order to achieve a total error ϵ_0 in Eq. 15, we implement the polynomials

$$P_{\cos}^{\epsilon_0}(xt) := \frac{P_{\cos}(xt)}{1 + \epsilon_0/4} \text{ and } P_{\sin}^{\epsilon_0}(xt) := \frac{P_{\sin}(xt)}{1 + \epsilon_0/4}, \quad (18)$$

of degrees d and $d+1$, respectively, where d is the truncation order given by

$$d = 2 \left\lceil \frac{\log\left(\frac{16}{5\epsilon_0}\right)}{2W\left(\frac{2}{\epsilon|t|} \log\left(\frac{16}{5\epsilon_0}\right)\right)} \right\rceil, \quad (19)$$

with W denoting the Lambert function [112, 113]. Notice that the parameter d directly affects the depth of the quantum circuit, as shown in Eq. 14. To implement the approximation polynomial $P(t\hat{H})$ on a quantum computer, given a block encoding of \hat{H}/α , one can realize $P((\alpha t)\hat{H}/\alpha)$ by encoding the real and imaginary components of the evolution operator separately. These correspond to $P_{\cos}^{\epsilon_0}((\alpha t)\hat{H}/\alpha)$ and $-iP_{\sin}^{\epsilon_0}((\alpha t)\hat{H}/\alpha)$, respectively. The two components are then combined using an ancillary qubit that controls the application of the corresponding operators, as illustrated in Fig. 3.

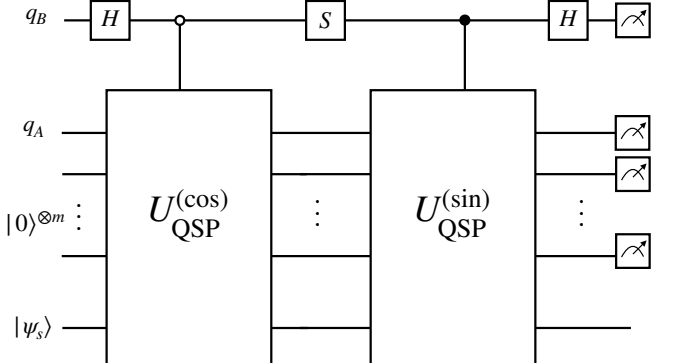


FIG. 3 Quantum circuit representation of the QSP implementation used to approximate the time-evolution operator $e^{-i\hat{H}t}$. The block $\hat{U}_{\text{QSP}}^{(\cos)}$ and $\hat{U}_{\text{QSP}}^{(\sin)}$ denotes the quantum circuit used to implement $P_{\cos}^{\epsilon_0}((\alpha t)\hat{H}/\alpha)$ and $P_{\sin}^{\epsilon_0}((\alpha t)\hat{H}/\alpha)$ respectively using quantum signal processing. The evolved quantum state $|\psi(t)\rangle$ is obtained upon post-selection of the ancillary qubit q_B in the state $|1\rangle$, while q_A and all m ancilla qubits in the state $|0\rangle$.

Having established the general formalism of Quantum Signal Processing for Hamiltonian simulation, we now apply it to a specific and physically relevant model. For the

purposes of this benchmark, we focus on a paradigmatic Hamiltonian widely used in condensed matter physics and quantum simulation, the transverse-field Ising model (TFIM).

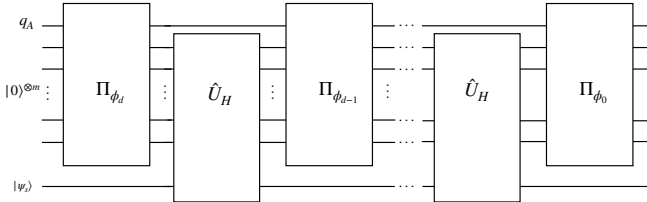


FIG. 4 Circuit representation of the QSP sequence described in Eq. (14), consisting of alternating phase-controlled projectors Π_{ϕ_k} with $k = 0, \dots, d$ and the block-encoding unitary \hat{U}_H . The circuit uses a single ancilla qubit q_A for controlled operations, m ancillary qubits to implement the block encoding of the Hamiltonian, and the qubits encoding the system state $|\psi_s\rangle$.

Ising Model.— The transverse-field Ising model (TFIM) is one of the most fundamental Hamiltonians in condensed matter physics [114], which describes L interacting spin- $\frac{1}{2}$ particles and is widely used to study magnetism, phase transitions, and critical phenomena. Considering periodic boundary conditions, the Hamiltonian reads as

$$\hat{H}_{\text{TFIM}} = \hat{H}_0 + J \sum_{j=1}^L \hat{\sigma}_j^x \hat{\sigma}_{j+1}^x, \quad (20)$$

where $\hat{H}_0 = g \sum_{j=1}^L \hat{\sigma}_j^z$ represents the local energy term and periodic boundary conditions are given by $\hat{\sigma}_{L+1}^x = \hat{\sigma}_1^x$. The transverse magnetic field and the bare exchange coupling are denoted by g , J , respectively. The operators $\hat{\sigma}_j^\alpha$ with $\alpha = x, z$, denote the Pauli matrices at lattice site

j . An analytical solution of the TFIM can be obtained by mapping the model to free fermions via the Jordan-Wigner and Bogoliubov transformations, as detailed in Ref. [115]. This solution enables the derivation of an analytical expression for the expectation value of the total magnetization $\hat{M}_z(t) = \frac{1}{L} \sum_i^L \hat{\sigma}_i^z$, providing an exact reference for benchmarking and ensuring the scalability of this benchmark. Moreover, due to the periodic boundary condition, the expectation value of the local magnetization $\hat{\sigma}_j^z$ is identical at every site.

From this analytical reference, the aim of the benchmark is to quantify how accurately the quantum processor reproduces the dynamics of the TFIM Hamiltonian. To this end, we consider all sources of error that contribute to deviations of the total magnetization estimate from its analytical value, excluding hardware errors. These include statistical sampling error, QSP approximation error, and observable estimation error. The expectation value of the magnetization is estimated using Hoeffding's inequality for a given accuracy ε and confidence level $1 - \delta$, which quantify the statistical precision and reliability of the measurement results. The remaining two error sources, the QSP approximation error and the observable estimation error, are discussed in detail in Appendix C.

2. Benchmark description

The Hamiltonian simulation benchmark aims to assess the capability of the quantum processor to simulate the time evolution by measuring the expectation value of magnetization $M_z(t)$ in the one-dimensional Transverse-Field Ising Model (TFIM) with periodic boundary conditions (PBC).

a. Stepwise instructions. A detailed description of the benchmark is provided in the following box, and a flow chart of the procedure is shown in Fig 5.

Protocol 3: TFIM Hamiltonian simulation benchmark protocol

Initialization: Set the time evolution $t > 0$, choose the number of spins $L \geq 3$, the tolerance error $\epsilon_0 \leq 7 \cdot 10^{-5}$ and fix the parameters $\varepsilon \leq 0.01$ and $\delta \leq 0.1$.

Return: The maximum evolution time t_{\max} for which the quantum hardware reproduces the global magnetization $M_z(t)$ with a bounded error.

Procedure:

1. **Initial condition of the system:** The initial condition of the system is given by

$$|\psi(0)\rangle = \bigotimes_{j=1}^L |0\rangle_j.$$

2. **Construct the quantum circuit.** The Fig. 4 shows the quantum circuit that approximates the time-evolution operator $e^{-i\hat{H}t}$ using the QSP technique.

(a) **Quantum circuit to implement the operator \hat{U}_H .** Considering the Transverse Field Ising Hamiltonian

$$\hat{H}_{\text{TFIM}} = \sum_{j=1}^L g \hat{Z}_j + \sum_{j=1}^L J \hat{X}_j \hat{X}_{j+1}, = \sum_{k=1}^{2L} \alpha_k \hat{U}_k, \quad \hat{U}_k \in \{\hat{Z}_j, \hat{X}_j \hat{X}_{j+1}\}.$$

with $J = g = \frac{1}{L \cdot e}$, so every $\alpha_k = \frac{1}{L \cdot e}$ and $\alpha = \sum_{k=1}^{2L} |\alpha_k| = \frac{2}{e}$. Define the vectors

$$\mathbf{P} = (\sqrt{\alpha_1/\alpha}, \dots, \sqrt{\alpha_{2L}/\alpha}) = \left(\sqrt{\frac{1}{2L}}, \dots, \sqrt{\frac{1}{2L}} \right) \quad \text{and} \quad \mathbf{U} = (\hat{U}_1, \dots, \hat{U}_{2L}).$$

Using the vectors \mathbf{P} and \mathbf{U} construct the quantum circuit implementing \hat{U}_{Prep} and \hat{U}_{Select} following the protocols described in the Appendices B 1a and B 1b, respectively. Then, use these quantum circuits to construct the quantum circuit implementing the operator \hat{U}_H as in Eq. 13.

(b) **Quantum circuit to implement the phase-controlled projector Π_{ϕ_i} .** Expand the functions $\cos(xt)$ and $\sin(xt)$ in the Chebyshev basis up to order $d/2$:

$$\cos(xt) \approx J_0(t) + 2 \sum_{k=1}^{d/2} (-1)^k J_{2k}(t) T_{2k}(x), \quad \sin(xt) \approx 2 \sum_{k=0}^{d/2} (-1)^k J_{2k+1}(t) T_{2k+1}(x), \quad (21)$$

where

$$d = 2 \left\lfloor \frac{\log(\frac{16}{5\epsilon_0})}{2W\left(\frac{1}{|t|} \log(\frac{16}{5\epsilon_0})\right)} \right\rfloor. \quad (22)$$

Store the coefficients of the Chebyshev expansion divided by $(1+\epsilon_0/4)$ in the vectors \mathbf{C}^{\cos} and \mathbf{C}^{\sin} , ordered from lowest to highest degree. Using the above vectors, compute the phase angles $\{\phi_k^{\cos}\}_{k=0,\dots,d}$ and $\{\phi_k^{\sin}\}_{k=0,\dots,d+1}$ using the procedure described in Appendix B 1c. Then, using procedure described in Appendix B 1d, construct the quantum circuits to implement the phase-controlled projector Π_{ϕ} .

(c) **Quantum circuit to implement QSP.** Construct the quantum circuit using Quantum Signal Processing to approximate the functions $\cos(\hat{H}t)$ and $\sin(\hat{H}t)$ with polynomials of degree d and $d+1$ respectively

$$U_{\text{QSP}}^{(\cos)} = \Pi_{\phi_0} \prod_{k=1}^d \hat{U}_H \Pi_{\phi_k^{\cos}}, \quad U_{\text{QSP}}^{(\sin)} = \Pi_{\phi_0} \prod_{k=1}^{d+1} \hat{U}_H \Pi_{\phi_k^{\sin}}.$$

With these two circuits and using an ancillary qubit q_b , construct the quantum circuit shown in Fig. 3.

3. Measurement of total magnetization $\langle M_z \rangle$.

(a) *Measurement basis.* All qubits are measured in the computational basis, and only shots with q_b in $|1\rangle$ state, and all other ancilla qubits in $|0\rangle$ state are selected. It can be seen that the probability of finding the ancillary qubits in these states is lower bounded by $\frac{(1-\epsilon_0)^2}{2}$. The resulting subset of measurements is denoted by S_{eff} .

(b) *Shot setting.* The total number of effective shots is computed using Hoeffding's inequality for a given ϵ and δ :

$$|S_{\text{eff}}| = \frac{2}{\epsilon^2} \ln \frac{2}{\delta}.$$

(c) *Estimator.* For each shot $s \in S_{\text{eff}}$, obtain a bitstring $b^{(s)} = (b_1^{(s)}, \dots, b_L^{(s)}) \in \{0, 1\}^L$ and map each bit to

$$z_i^{(s)} = (-1)^{b_i^{(s)}} \in \{1, -1\},$$

where $z_i^{(s)}$ denotes the sample value for the qubit i in shot s . The expectation value of the magnetization of each qubit is estimated as follows

$$\mu_i = \frac{1}{|S_{\text{eff}}|} \sum_{s \in S_{\text{eff}}} z_i^{(s)},$$

where μ_i is the mean value of the shots. We finally compute the total magnetization of the system, i.e, the mean over all the qubits as

$$\mu = \frac{1}{L} \sum_{i=1}^L \mu_i. \quad (23)$$

4. Compute analytical value. Compute the analytical expectation value of the total magnetization at time t as follows

$$M_z(t) = 1 - \frac{2}{L} \sum_{m=0}^{L-1} \frac{\Delta_m^2}{\epsilon_m^2 + \Delta_m^2} \sin^2(E_m t), \quad (24)$$

where

$$\epsilon_m = \frac{1}{eL} - \cos\left(\frac{2\pi m}{L}\right), \quad \Delta_m = \sin\left(\frac{2\pi m}{L}\right), \quad E_m = \frac{2}{eL} \sqrt{\epsilon_m^2 + \Delta_m^2}. \quad (25)$$

5. Evaluate the estimator. If the calculated total magnetization μ lies inside the interval

$$C = [M_z(t) - 10(2\epsilon_0 + \varepsilon), M_z(t) + 10(2\epsilon_0 + \varepsilon)],$$

where $2\epsilon_0 + \varepsilon$ accounts for the method and measurement errors, respectively, and is independent of noise, see Appendix C.

6. Increment time. If $\epsilon_{t,\min} < 7 \cdot 10^{-5}$, increment t ; otherwise, decrement t , and repeat from Step 1. Continue this procedure until a value of t is found such that $\epsilon_{t,\min} < 7 \cdot 10^{-5}$ and $\epsilon_{t+s,\min} \geq 7 \cdot 10^{-5}$, where s is a user-selected small increment satisfying $s < 0.01$.

b. Selection of parameters and strategies. The strategies and parameters restrictions are as follows:

- The choice $L \geq 3$ guarantees a non-trivial TFIM instance under periodic boundary conditions. The total number of qubits required to execute the TFIM Hamiltonian simulation benchmark protocol is

$$N_T = L + \lceil \log_2(2L) \rceil + 2.$$

- The transverse magnetic field and the bare exchange coupling are fixed $g = J = (Le)^{-1}$. With this choice, the normalization factor is given by $\alpha = 2/e$. As a consequence, the degree of the polynomial approximations d used in QSP depend on integer evolution times, simplifying the analysis and allowing the benchmark to simulate the dynamics by incrementing $t \in \mathbb{N}$. It also simplifies the determination of t_{\max} , since we avoid searching over real-valued times that may satisfy the error condition but produce negligible changes in circuit depth.

- The strategy for selecting and updating ϵ_0 in order to determine $\epsilon_{t,\min}$ for a given evolution time t is left to the user. However, we recommend employing a binary-search procedure, which requires only a logarithmic number of iterations to achieve the desired precision. To further reduce the number of updates of this parameter, one may initialize ϵ_0 using information obtained from executions at other values of t , or even from classical simulations when the parameter L is sufficiently small.
- The strategy for updating t in Step 6 is left to the user; however, a binary search is recommended, as it scales logarithmically with the desired precision s . The precision s , which determines the accuracy in identifying the largest admissible value of t , is user-defined and must satisfy $s \leq 0.01$.
- By setting $\varepsilon \leq 0.01$ and $\delta \leq 0.1$, we ensure high-precision results and mitigate large fluctuations in the metric arising from statistical variability. With

Parameters and strategies	Rules
L	≥ 3
δ	≤ 0.1
ε	≤ 0.01
g	$\frac{1}{L\varepsilon}$
J	$\frac{1}{L\varepsilon}$
ϵ_0	$\leq 7 \cdot 10^{-5}$
q_A	1
q_B	1
q_m	$[\log_2 2L]$
t	> 0
s	≤ 0.01
Strategy to update t	The choice is left to the user; however, a binary search is recommended.
Strategy to update ϵ_0	The choice is left to the user; however, a binary search is recommended.
Select initial ϵ_0	While the choice is left to the user, leveraging information from the benchmark execution with fewer qubits or from classical simulations is recommended.

TABLE III Summary of the parameters and strategies for the TFIM Hamiltonian simulation benchmark. The table includes the rules for the system size L , the confidence level δ , the accuracy ε , the transverse field g and the exchange coupling J in the TFIM Hamiltonian, the tolerance ϵ_0 , the ancillary qubits q_A, q_B, q_m , the evolution time t , and the precision parameter s . Furthermore, the table includes strategies for selecting and updating t and ϵ_0 .

these two parameters, the number of effective shots remains below $6 \cdot 10^4$, which is a reasonable scale for current quantum hardware.

- Although we provide complete circuits and a detailed methodology for constructing the final quantum circuit, these should be regarded as recommendations rather than strict requirements. The only mandatory aspect is that the circuit must employ QSP using the constructions shown in Fig. 3 and Fig. 4. The implementations of the block encoding and the phase-controlled projectors may be freely adapted by the user, provided that they perform the same operations as the reference constructions.

A summary of the parameters and execution strategies for this benchmark is provided in Table III.

c. Metric definition The metric of the TFIM Hamiltonian simulation benchmark reports for a selected number of spins L , the maximum evolution time, denoted t_{\max} . It is defined as the largest evolution time for which

the quantum hardware can successfully reproduce the global magnetization $M_z(t)$ of the Ising model with an error not exceeding certain quantity. Although t_{\max} is the primary metric for comparison, the vector of approximation errors $\epsilon_{t,\min}$ for each evolution time $t \in [1, t_{\max}]$ provides valuable information and can serve as a secondary metric to further characterize the quantum computer's ability to reproduce the global magnetization $M_z(t)$ of the Ising model. This metric provides insight into how well the quantum computer can perform Hamiltonian simulation using the QSP technique.

d. Reporting requirements. For the TFIM Hamiltonian simulation benchmark experimental teams or hardware providers are required to submit a comprehensive report that includes the elements specified in Section II, as well as the following additional items

- The estimated observables $\hat{\mu}_i$ and its mean μ_i of Step 3c for each qubit i , time t and ϵ_0 .
- The strategy used to update t in Step 6.
- The strategy used to update ϵ_0 in Step 5.
- Methods and circuits for implementing the block encoding and the phase-controlled projector in QSP.

3. Benchmark and metric property analysis

1. Relevance: The Hamiltonian simulation Benchmark is relevant because simulating Hamiltonian dynamics represents one of the most fundamental and meaningful workloads in quantum computing. It is directly applicable to both scientific and industrial domains, including condensed matter physics, quantum chemistry, and materials science. Comparing the measured values with an exact analytical solution of the total magnetization validates the simulated dynamics along this observable, but does not certify the full quantum state. However, this validation provides confidence that the same QSP framework can be extended to probe additional observables of the TFIM. Furthermore, the use of Quantum Signal Processing as the underlying simulation technique makes this benchmark advanced, as QSP is one of the most powerful and algorithmically optimal methods for implementing Hamiltonian dynamics on quantum devices.

2. Reproducibility: The benchmark is reproducible because the entire procedure can be repeated under identical conditions using the same qubits, circuit construction and parameter settings. Together, these well-defined steps yield consistent estimates of t_{\max} . Although small deviations may arise from calibration drift or quantum-hardware noise. Consequently, independent repetitions of the benchmark are expected to produce closely aligned out-

comes, demonstrating that the procedure is stable and repeatable across multiple runs.

3. **Fairness:** This benchmark is fair because the quantum circuit used to simulate the dynamics of the transverse-field Ising model can be directly transpiled into the native gate set of any quantum computing platform. In addition, users are free to choose their own strategy for updating ϵ_0 , thereby reducing potential bias toward specific hardware platforms. The use of Quantum Signal Processing (QSP) ensures that all architectures execute the same workload, independent of their technological details. Moreover, the compilation rules and reporting avoid architecture-specific optimizations, guaranteeing that performance differences arise solely from hardware quality rather than implementation choices.
4. **Verifiability:** The benchmark is verifiable because every component of the procedure is well defined, from the quantum circuit to implement the QSP technique and observable estimation. The experimental measurement of magnetization is accompanied by explicit statistical guarantees via Hoeffding's inequality, ensuring controlled and quantifiable uncertainty. Moreover, the reference value for the TFIM magnetization is obtained from an exact analytical solution, enabling a direct comparison between hardware outputs and the theoretical prediction. Together, these features ensure that independent implementations can reliably reproduce and validate the benchmark outcomes

5. **Usability:** The Hamiltonian simulation benchmark is easy to use because its procedure is fully specified and can be implemented directly on any quantum computing platform. The construction of the block encoding, the generation of QSP phases, and the measurement protocol are classical efficient. In addition, the availability of an exact analytical solution for the magnetization makes the benchmark scalable: the reference value can be computed efficiently for any system size, enabling straightforward comparison between theoretical and experimental results. The design ensures that both experimental teams and hardware providers can apply the benchmark across devices of different sizes and connectivity.

Using the data obtained from the quantum device, the metric defined in Sec. III C 2c is computed classically. This metric is analyzed with respect to the following properties, as shown in Table IV:

1. **Practical:** The metric is practical, as computing sample means from the bitstrings and evaluating the analytical solution of the TFIM magnetization are both computationally scalable. Moreover, the

determination of the parameter $\epsilon_{t,\min}$ can be performed using an efficient strategy, such as a binary search, ensuring that the required accuracy is found without incurring computational overhead.

2. **Repeatable:** The metric is repeatable, since given the same set of bitstrings obtained from the quantum device, the procedure used to compute the metric produces the same value.
3. **Reliable:** The metric is reliable in the sense that a higher value for a given quantum device indicates its ability to simulate the global magnetization of the Ising model for longer times. However, it is not a reliable measure of the device's overall capability to perform Hamiltonian simulation.
4. **Consistent:** The metric is consistent, as it preserves the same meaning across different hardware platforms.

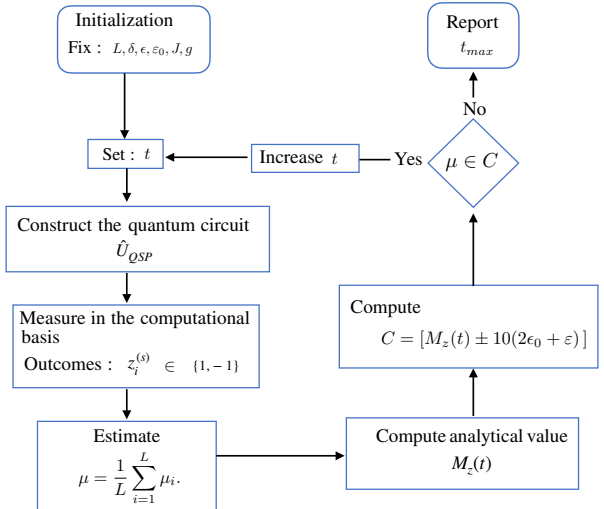


FIG. 5 Flow chart of the TFIM Hamiltonian simulation benchmark following the steps described in Protocol 3. The diagram illustrates the iterative procedure used to determine the maximum evolution time t_{\max} for which the estimated total magnetization μ remains within the interval $C = [M_z(t) - 10(2\epsilon_0 + \epsilon), M_z(t) + 10(2\epsilon_0 + \epsilon)]$

D. Data Re-uploading QNN Benchmark

1. Background and motivation

Quantum Machine Learning (QML) is a research field at the intersection of quantum computing and machine learning that explores algorithms and models leveraging quantum mechanical principles to perform learning tasks, with the potential to outperform classical methods [116–118]. QML has been applied across a wide range of do-

mains, including image recognition [119], computer vision [120], natural language processing [121], quantum chemistry [122], materials science [123], finance [124] and medical applications [125].

Within QML, several model classes have been proposed to address different learning paradigms, including Quantum Kernel Methods [126, 127], Quantum Reinforcement Learning [128], Quantum Generative Models [129], and Quantum Neural Networks (QNNs) [130, 131], among others. QNNs, in particular, have emerged as one of the most prominent models due to their structural similarity to classical neural networks and their adaptability to the variational hybrid framework suitable for Noisy Intermediate-Scale Quantum (NISQ) devices. QNNs are based on parameterized quantum circuits (PQCs), which are trained through classical or quantum optimization routines to minimize a cost function. However, this training process is often challenging due to the barren plateau phenomenon [132, 133]. One approach to mitigate this issue is the data re-uploading QNN architecture [130], in which data-encoding unitaries are interleaved with trainable unitaries. This technique is particularly effective because it introduces nonlinearities into the model, enabling it to capture complex patterns in data. Moreover, it has been shown to possess universal approximation capabilities for a single-qubit quantum classifier [134]. Owing to these properties, data re-uploading QNNs are strong candidates for near-term quantum applications in classification tasks. For this reason, we adopt a binary classifier as the basis for our benchmark.

The simplest encoding strategy for this architecture, in the single-qubit case, is given by

$$\text{QNN}_{\theta}(\mathbf{x}) := \prod_{l=1}^L U(\theta_l)U(\mathbf{x}) \quad (26)$$

where L denotes the number of layers, U represent generic SU(2) unitary, \mathbf{x} encodes classical input data, and the vector $\theta = \{\theta_1 \dots \theta_L\}$ encompasses the trainable parameters. This model can be used to construct a binary classifier by selecting two label states that are maximally separated in Hilbert space. The training objective is to adjust the parameters so that the model rotates data points from each class toward their corresponding label state, thereby enabling effective classification.

This class of QNNs can be extended beyond the single-qubit setting by employing multi-qubit parameterized circuits with entangling layers, which increase the number of trainable parameters per layer and enhance the expressivity of the model through entanglement [135]. The multi-qubit extension of the data re-uploading architecture can be written as

$$\begin{aligned} \text{QNN}_{\theta, \varphi}(\mathbf{x}) := & \\ \prod_{l=1}^L \left(\prod_{s=1}^{N-1} \text{CU}_{s+1}(\varphi_l^{(s)}) \left(\bigotimes_{r=1}^N U(\theta_l^{(r)}) \right) U(\mathbf{x})^{\otimes N} \right), \quad (27) \end{aligned}$$

where L denotes the number of layers and N the number of qubits, $U(\theta_l^{(r)})$ represents single-qubit trainable unitary applied to qubit r in layer l . The unitary $\text{CU}_{s+1}(\varphi_l^{(s)})$ denotes the controlled version of the general SU(2) unitary where the $(s+1)$ -th qubit acts as the control and the s -th qubit as the target. The parameter sets θ and φ denote the trainable parameters associated with the single-qubit and two-qubit gates, respectively. The total number of trainable parameters in this architecture is $3(2N-1)L$ [136]. Figure 6 shows the quantum circuit representation of a multi-qubit quantum neural network with data re-uploading.

This multi-qubit QNN, when applied to classification tasks and binary classification in particular, can improve upon the performance of its single-qubit counterpart [136]. The construction and training procedure follows a progressive strategy: starting from the one-qubit QNN, the architecture is expanded by adding qubits incrementally. When a new qubit is introduced, the corresponding entangling gates are initialized as identity operations, and training begins from the optimal parameters obtained in the previous stage. This structured, qubit-by-qubit scaling enables a systematic and hardware-efficient extension of the QNN, while mitigating the onset of barren plateaus.

The training process optimizes the parameters θ and φ through an iterative procedure that minimizes a cost function quantifying the discrepancy between the QNN output and the target labels. Parameter updates are performed by computing the gradient of the cost function with respect to θ and φ . These partial derivatives can be efficiently estimated using the parameter-shift rule [137, 138], a technique that evaluates each derivative by executing the same quantum circuit twice, with the parameter of interest shifted by fixed amounts. This enables gradient-based training without requiring access to the full analytical form of the cost function.

One limitation of these QNN architectures arises from the fact that a general single-qubit unitary can be parametrized by at most three rotation angles. Consequently, each data-encoding unitary can encode at most three features of the input data. The same restriction applies to controlled unitaries, which also allow encoding only up to three features. Therefore, when working with data sets that have more than three features, a classical preprocessing step (e.g., feature selection or dimensionality reduction) becomes necessary to reduce the dimensionality of the input. This ensures that the data can be efficiently mapped into a feature space compatible with the quantum encoding capabilities of the available qubits.

2. Benchmark description

The Data Re-uploading QNN Benchmark aims to evaluate how effectively a quantum computer can perform binary classification tasks, i.e., classify input data into two categories. To this end, the benchmark uses several

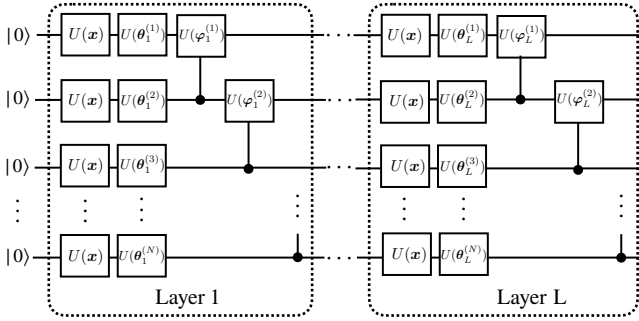


FIG. 6 Circuit representation of the multi-qubit quantum neural network with data re-uploading described in Eq. (27). Here, $U(\mathbf{x})$ denotes the data-encoding unitary, while $U(\boldsymbol{\theta}_l^{(r)})$ and $U(\boldsymbol{\varphi}_l^{(s)})$ represent the single-qubit trainable unitaries and the controlled trainable unitaries, respectively, with $r = 1, \dots, N$, $s = 1, \dots, N-1$, and $l = 1, \dots, L$.

binary datasets with assigned labels. For each dataset, we construct a multi-qubit data-reuploading QNN as defined in Eq. 27, train the network using a subset of the dataset (the training set), and then evaluate its performance on a separate subset (the test set). The test accuracy is computed as the number of correct predictions divided by the total number of test samples. Finally, the benchmark metric is obtained by averaging the test accuracies across all datasets, providing an overall indicator of how well the quantum computer can perform binary classification tasks.

The circuit we employ corresponds to a particular instance of the QNN architecture in Eq. 27, where each data-encoding unitary is decomposed as

$$U(\mathbf{x}) = R_z(\pi x_1) R_y(\pi x_2) R_z(\pi x_3), \quad (28)$$

with $\mathbf{x} = \{x_1, x_2, x_3\}$ denoting the input classical data

consisting of three features that ranges from -1 to 1. Similarly, each trainable single-qubit unitary is decomposed as

$$U(\boldsymbol{\theta}_l^{(r)}) = R_z(\theta_{l,1}^{(r)}) R_y(\theta_{l,2}^{(r)}) R_z(\theta_{l,3}^{(r)}), \quad (29)$$

where the parameters $\boldsymbol{\theta}_l^{(r)} = \{\theta_{l,1}^{(r)}, \theta_{l,2}^{(r)}, \theta_{l,3}^{(r)}\}$ that moves from $[-\pi, \pi]$, are optimized during the training process. Finally, the controlled unitaries, where qubit $s+1$ acts as the control and qubit s as the target, are defined as

$$\text{CU}_{s+1}(\boldsymbol{\varphi}_l^{(s)}) = |0\rangle\langle 0|_{s+1} \otimes \mathbb{I}_s + |1\rangle\langle 1|_{s+1} \otimes U(\varphi_{l,1}^{(s)}, \varphi_{l,2}^{(s)}, \varphi_{l,3}^{(s)}), \quad (30)$$

where the single-qubit rotation applied to the target qubit is given by

$$U(\varphi_{l,1}^{(s)}, \varphi_{l,2}^{(s)}, \varphi_{l,3}^{(s)}) = \begin{bmatrix} e^{-i(\varphi_{l,1}^{(s)} + \varphi_{l,3}^{(s)})/2} \cos(\frac{\varphi_{l,2}^{(s)}}{2}) & -e^{i(\varphi_{l,1}^{(s)} - \varphi_{l,3}^{(s)})/2} \sin(\frac{\varphi_{l,2}^{(s)}}{2}) \\ e^{-i(\varphi_{l,1}^{(s)} - \varphi_{l,3}^{(s)})/2} \sin(\frac{\varphi_{l,2}^{(s)}}{2}) & e^{i(\varphi_{l,1}^{(s)} + \varphi_{l,3}^{(s)})/2} \cos(\frac{\varphi_{l,2}^{(s)}}{2}) \end{bmatrix}. \quad (31)$$

The parameters $\boldsymbol{\varphi}_l^{(s)} = \{\varphi_{l,1}^{(s)}, \varphi_{l,2}^{(s)}, \varphi_{l,3}^{(s)}\}$ that moves from $[-\pi, \pi]$, are optimized during the training process.

To maintain a fair and hardware-focused benchmark, we use synthetic datasets with exactly three features so that no classical dimensionality-reduction techniques are necessary. Additionally, to obtain reliable performance estimates, each dataset is partitioned multiple times into training and test sets using a 70/30 split, where 70% of the samples are used for training and 30% for testing.

a. Stepwise instructions. A detailed description of the benchmark is provided in the following box, and a flow chart of the procedure is shown in Fig 7.

Protocol 4: Data Re-Uploading QNN Benchmark Protocol

Initialization: Choose the maximum number of qubits N_{\max} , the layer depth L , and the parameters $\varepsilon \leq 0.05$ and $\delta \leq 0.1$, which denote the allowed classification error and the confidence level of the estimation, respectively. For each dataset indexed by k , the training dataset $\mathcal{X}^{(k)}$ and test dataset $\mathcal{T}^{(k)}$ contain features rescaled to the interval $[-1, 1]$, which are defined as follows

$$\mathcal{X}^{(k)} = \{(\mathbf{x}^{(i)}, y_x^{(i)})\}_{i=1}^{M_x}, \quad \mathcal{T}^{(k)} = \{(\mathbf{t}^{(i)}, y_t^{(i)})\}_{i=1}^{M_t}, \quad (32)$$

where M_x and M_t represent the number of training and test samples in the k -th dataset split, respectively. The vectors $\mathbf{x}^{(i)}$ and $\mathbf{t}^{(i)}$ denote the i -th input samples used for training and testing, and $y_x^{(i)}$ and $y_t^{(i)}$ are their corresponding labels that belongs to the set $\{-1, 1\}$.

Return: For each N -qubit QNN architecture with $N = 1, \dots, N_{\max}$, return the average test accuracy $\overline{\text{Acc}}_{\text{test}}(N, L)$ computed over all dataset partitions, together with its sampled standard deviation $\sigma_{\text{Acc}}(N, L)$.

Procedure:

1. **Training and testing.** For each dataset indexed by k :

(a) For each number of qubits N from 1 to N_{\max} :

- i. **Circuit construction.** Construct the quantum circuit to implement the N -qubit QNN architecture composed of L layers, see Fig 6. Notice that for $N = 1$, the same circuit is implemented, but without the controlled gates.
- ii. **Train N -qubit QNN architecture.** Obtain the optimal parameters $\{\theta^*, \varphi^*\}_k^N$ training the N -qubit QNN architecture following the Protocol 9 if $N = 1$, or Protocol 10 if $N > 1$.
- iii. **Test N -qubit QNN architecture.** Evaluate the performance of the trained N -qubit QNN architecture on the test dataset $\mathcal{T}^{(k)} = \{(\mathbf{t}^{(i)}, y_t^{(i)})\}_{i=1}^{M_t}$ using its corresponding optimal parameters $\{\theta^*, \varphi^*\}_k^N$. For each input $\mathbf{t}^{(i)}$, measure the first qubit in the computational basis

$$\frac{2}{\varepsilon^2} \log \left(\frac{2}{\delta} \right), \quad (33)$$

times and compute the sample mean $\hat{\mu}^{(i)}$ that estimates the expectation value of the Pauli Z operator, as we described in Step 1(b)ii of Protocol 10. Estimate the fidelity with respect to the corresponding label $y_t^{(i)}$ as follows

$$F^{(i)}(\mathbf{t}^{(i)}; \theta) = \frac{1 + y_t^{(i)} \hat{\mu}^{(i)}}{2}, \quad y_t^{(i)} \in \{-1, 1\}.$$

A test sample is considered correctly classified if its fidelity satisfies $F^{(i)} \geq 0.5$; otherwise, it is considered incorrectly classified.

- iv. **Compute test accuracy.** The test accuracy is given by

$$\text{Acc}_{\text{test}}^{(k)}(N, L) = \frac{M_c}{M_t},$$

where M_c denotes the number of correctly classified test samples and M_t the total number of test samples.

2. **Compute the average test accuracy.** For each N -qubit QNN architecture for N from 1 to N_{\max} , compute the average accuracy by averaging over all dataset partitions

$$\overline{\text{Acc}}_{\text{test}}(N, L) = \frac{1}{K} \sum_{k=1}^K \text{Acc}_{\text{test}}^{(k)}(N, L), \quad (34)$$

and its sample standard deviation

$$\sigma_{\text{Acc}}(N, L) = \sqrt{\frac{1}{K} \sum_{k=1}^K \left(\text{Acc}_{\text{test}}^{(k)}(N, L) - \overline{\text{Acc}}_{\text{test}}(N, L) \right)^2}. \quad (35)$$

where K denotes the total number of datasets, and return both.

b. *Selection of parameters and strategies* The strategies and parameter restrictions are as follows:

- Setting $\varepsilon \leq 0.05$ and $\delta \leq 0.1$ yields accurate estimates with limited statistical fluctuations. These parameters keep the effective shot count below $3 \cdot 10^3$, which is practical for current quantum hardware.
- The datasets referenced in the initialization phase of Protocol 4 are publicly available at [139]. To

construct the training and test sets, users should randomly partition the data such that 30% of the samples are assigned to the test set and the remaining 70% to the training set. Despite the random selection, both subsets should maintain an approximately balanced distribution of samples belonging to classes -1 and 1. While the use of these datasets is mandatory, users may additionally incorporate their own datasets, provided that these are clearly described and properly documented.

Benchmarking Metrics Properties Analysis				
Metric	Practical	Repeatable	Reliable	Consistent
Partial Clifford	✓	✓	✓	✓
Multipartite Entanglement	✓	✓	✓	✓
TFIM Hamiltonian Simulation	✓	✓	✓/✗	✓
Data Re-uploading QNN	✓	✓	✓/✗	✓

TABLE IV Summary of the properties satisfied by the metrics used in each benchmark in the QuSquare suite. The table indicates whether each metric is practical, repeatable, reliable, and consistent. The check mark indicates that the metric satisfies the attributes; otherwise, we use the cross mark.

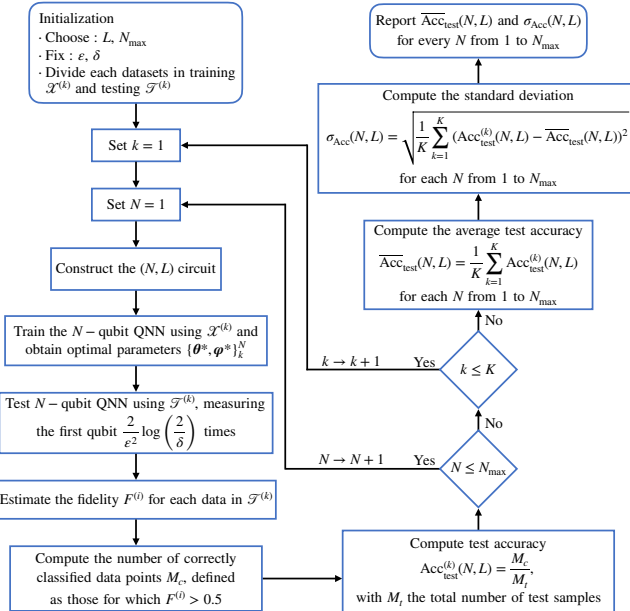


FIG. 7 Flowchart of the Data Re-Uploading QNN Benchmark. The diagram summarizes the steps described in Protocol 4, including the construction, training, and testing of the N -qubit QNN architecture, the computation of the test accuracy for each dataset, and the evaluation of the average test accuracy $\text{Acc}_{\text{test}}(N, L)$ and its sample standard deviation $\sigma_{\text{Acc}}(N, L)$ across all datasets.

- Before initiating the training of the single-qubit QNN, the user must first choose the initial values of the trainable parameters. The strategy for selecting these initial values is left to the user. Once the initialization is chosen, the QNN is trained as described in Appendix D to obtain the optimal parameters for the one-qubit model. The user may repeat this procedure multiple times with different initializations in order to search for better optima, provided that all runs are properly reported.
- The number of training epochs for each QNN is defined by the user and must be properly reported. For example, training may stop when the gradient of the cost function falls below a chosen threshold, or after a fixed number of epochs selected by the user.

Parameters and strategies	Rules
δ	≤ 0.1
ε	≤ 0.05
$\mathcal{X}^{(k)}$ and $\mathcal{T}^{(k)}$	The datasets from [139] and any user added datasets.
Strategy for one-qubit parameter initialization	Is left to the user.
Number of initialization and training rounds for the one-qubit QNN	Is left to the user.
The strategy for selecting the training epoch	Is left to the user.
The learning rate parameter η	Is left to the user.

TABLE V Summary of the parameters and strategies for the Data Re-Uploading QNN Benchmark. The table includes the rules for the confidence level δ , the accuracy ε , and the datasets $\mathcal{X}^{(k)}$ and $\mathcal{T}^{(k)}$. The strategies for choosing the one-qubit parameter initialization, the number of training rounds, the selection of the training epoch, and the learning rate parameter η are left to the user.

- The learning rate parameter η used to update the parameters during the training process as described in Appendix D, may be freely chosen by the user. Moreover, η does not need to remain fixed throughout training: the user may adopt any scheduling or adaptive strategy for selecting η , provided that the chosen approach is reported.

A summary of the parameters and execution strategies for this benchmark is provided in Table V.

c. Metric definition. The metric reported by the Data Re-uploading QNN Benchmark for a given number of qubits N and circuit depth L is the average test accuracy over all dataset partitions, denoted $\text{Acc}_{\text{test}}(N, L)$, together with its corresponding standard deviation $\sigma_{\text{Acc}}(N, L)$. This metric is intended to quantify the capability of the quantum computer to perform binary classification tasks.

d. Reporting requirements. To ensure reproducibility, experimental groups or providers must report sufficient information about their implementation. In partic-

ular, they are required to submit a comprehensive report that includes the elements specified in Section II, as well as the following additional items, for each N -qubit QNN architecture with L layers:

- The test accuracy of every dataset, $\text{Acc}_{\text{test}}^{(k)}(N, L)$.
- The optimized parameters for each dataset and number of qubits $\{\boldsymbol{\theta}^*, \boldsymbol{\varphi}^*\}_k^N$.

3. Benchmark and metric property analysis

1. **Relevance:** This benchmark is relevant because it evaluates one of the most widely used QML architectures in the quantum-computing field. These architectures are applied to binary classification, supervised learning, and regression tasks, and serve as a natural reference point for assessing the capability of quantum processors in machine-learning applications. In addition, data re-uploading QNNs have well-established universality and expressivity properties, and have been proposed as natural candidates for demonstrating potential advantages in classification tasks. Consequently, the benchmark captures a practically meaningful and technologically significant dimension of quantum-hardware performance.
2. **Reproducibility:** The benchmark is reproducible because the entire training–testing workflow can be executed under identical conditions using the same qubits, circuit architecture, datasets, and parameter settings. These well-defined steps ensure that the resulting test accuracies are statistically consistent across repeated runs. Although small fluctuations may arise due to both statistical estimation error and hardware-effects such as calibration drift or noise, independent executions of the protocol are expected to yield closely aligned accuracy values. This demonstrates that the method remains stable and repeatable across multiple trials within the expected statistical uncertainty.
3. **Fairness:** The benchmark does not favor any particular quantum-hardware architecture. Providers are free to choose many parameters and strategies such as, the learning rate, the transpilation strategy, the native-gate decomposition, or the initial parameters before training, enabling each platform to achieve its best possible performance. However, the datasets, training/testing methodology, and protocol rules cannot be modified, preventing device-specific optimizations that would introduce bias. This guarantees that the benchmark enables fair comparison across platforms.
4. **Verifiability:** The benchmark is verifiable because the quantum circuit of each N -qubit QNN architectures are well defined. Moreover, the reported

test accuracy depends solely on single-qubit Pauli- Z measurements, whose statistical uncertainty is characterized by ε and δ .

5. **Usability:** The benchmark is practical to implement on current quantum devices. It requires only multi-qubit parameterized quantum circuits with standard single-qubit rotations and controlled gates, three-feature datasets that avoid high-dimensional encodings, and gradient estimation via the parameter-shift rule, which is widely supported on existing platforms. Because the number of qubits N and the circuit depth L are user-configurable, the benchmark scales to devices of different sizes. This makes the benchmark suitable both for small NISQ processors and for larger systems, as increasing N and L adds layers of the same circuit structure. Moreover, the total number of trainable parameters grows linearly with the number of qubits, $3(2N - 1)L$, which makes the training overhead manageable even as the architecture increases in size. Consequently, the benchmark is easy to implement and scalable, allowing evaluation of hardware performance as system size grows.

Using the data obtained from the quantum device, the metric defined in Sec. III D 2 c is computed classically. This metric is analyzed with respect to the following properties, as shown in Table IV:

1. **Practical:** The metric is practical because all the steps required for its evaluation, such as computing the fidelity and the test accuracy, can be carried out efficiently.
2. **Repeatable:** The metric is repeatable because all computations are deterministic, provided that the same measurement data are obtained from the device.
3. **Reliable:** The metric is reliable for the task of binary classification when a sufficient number of initial points are used to mitigate convergence to local minima. However, it is not reliable for determining which device is less noisy for this type of circuit, since noise can, in some cases, facilitate the training of the QNN [140, 141].
4. **Consistent:** No hardware-specific bias is introduced, and the metric is computed identically across all architectures; therefore, the metric is consistent.

IV. CONCLUSION & OUTLOOK

We have introduced the QuSquare benchmark suite designed to provide a rigorous and well-defined methodology for evaluating the performance of pre-fault-tolerant quantum devices. The suite encompasses both system-

and application-level benchmarks, such as Partial Clifford Randomized, Multipartite Entanglement, TFIM Hamiltonian Simulation, and Data Re-Uploading Quantum Neural Network. At the system level, the Partial Clifford Randomized benchmark stands out for its scalability and independence from the native gate set, while the Multipartite Entanglement benchmark assesses the ability of quantum processors to generate genuine multipartite entanglement and provides an efficient procedure for its estimation. At the application level, the TFIM Hamiltonian Simulation benchmark employs quantum signal processing, a cutting-edge approach for simulating quantum many-body dynamics. The Data Re-Uploading QNN benchmark offers a scalable and adaptable model that can be efficiently mapped onto different quantum hardware architectures and provides provable performance in classification tasks.

QuSquare has been designed to satisfy key quality attributes such as scalability, fairness, relevance, verifiability, and reproducibility. Subsequently, the quality attributes of the associated metrics have also been analyzed and discussed.

Scalability is ensured by design across all benchmarks through the use of protocols and metrics that remain efficient as the number of qubits increases. At the system level, this includes benchmarks based on quantum circuits that are efficiently simulatable on classical hardware, as well as fidelity estimation procedures that scale efficiently with system size. At the application level, scalability is supported by an analytical reference solution and an efficiently trainable model, enabling meaningful performance evaluation as quantum processors grow.

Fairness is achieved by controlling the influence of hardware-specific optimizations and by reducing ambiguities in benchmark protocols. While certain parameters and selection strategies are *intentionally* left flexible to avoid bias between quantum hardware, clear compilation/transpilation rules are enforced to prevent artificial shortcuts that could otherwise lead to overestimated performance. Furthermore, QuSquare generally specifies benchmarks at the algorithmic level while allowing flexibility in their implementation at the specific gate-decomposition level, provided that the algorithmic structure is preserved. This balance ensures fair and meaningful comparisons across quantum computing platforms.

The relevance of QuSquare is reflected in the choice of benchmarks that target both fundamental resources and novel promising applications in quantum computing. At the system level, the benchmarks are designed to evaluate the quantum processor through resources that play a crucial role in quantum computing, such as entanglement generation and the implementation of Clifford gate oper-

ations. At the application level, the benchmarks assess the capabilities of quantum devices through applications that are promising for quantum computing, including the simulation of quantum many-body dynamics and the use of quantum processors for classification tasks.

Finally, verifiability and reproducibility are ensured through clearly defined reporting requirements that specify the data, the results of the metrics, and execution details to be provided for each benchmark. By enforcing standardized reporting practices, QuSquare enables benchmark results to be independently reproduced and verified by users and providers.

Overall, QuSquare establishes a rigorous and hardware-agnostic framework for the evaluation of pre-fault-tolerant quantum processors. It addresses key limitations of existing benchmarking approaches, which are often based on a single test and ambiguously defined protocols. Looking ahead, this framework provides a core to which additional benchmarks may be incorporated in the future, extending the range of hardware capabilities that can be assessed.

V. ACKNOWLEDGMENT

The authors thank R. Ibarrondo, X. Gutierrez de la Cal and C. Cristiano Romero for useful discussions. We acknowledge financial support from Open-SuperQ+100 (Grant No. 101113946) of the EU Flagship on Quantum Technologies, from Project Grant No. PID2024-156808NB-I00 and Spanish Ramón y Cajal Grant No. RYC-2020-030503-I funded by MICI-U/AEI/10.13039/501100011033 and by “ERDF A way of making Europe” and “ERDF Invest in your Future”, from the Spanish Ministry for Digital Transformation and of Civil Service of the Spanish Government through the QUANTUM ENIA project call-Quantum Spain, and by the EU through the Recovery, Transformation and Resilience Plan–NextGenerationEU within the framework of the Digital Spain 2026 Agenda, and from Basque Government through Grant No. IT1470-22, and the Elkartek project KUBIBIT - kuantikaren berrikuntzarako ibilbide teknologikoak (ELKARTEK25/79). Grant FPU23/02196 funded by MCIN/AEI/ 10.13039/501100011033 and, as appropriate, by “ESF Investing in your future” or by “European Union NextGenerationEU/PRTR”. This research is supported by the Basque Government through the BERC 2022-2025 program and by the Ministry of Science and Innovation: BCAM Severo Ochoa accreditation CEX2021-001142-S / MICIN / AEI / 10.13039/501100011033.

[1] A. Acuaviva, D. Aguirre, R. Peña, and M. Sanz, Benchmarking quantum computers: Towards a standard

performance evaluation approach, [arXiv:2407.10941](https://arxiv.org/abs/2407.10941) (2024), available at [arXiv.2407.10941](https://arxiv.org/abs/2407.10941).

[2] C. Hempel, C. Maier, J. Romero, J. McClean, T. Monz, H. Shen, P. Jurcevic, B. P. Lanyon, P. Love, R. Babbush, A. Aspuru-Guzik, R. Blatt, and C. F. Roos, Quantum chemistry calculations on a trapped-ion quantum simulator, *Physical Review X* **8**, [10.1103/physrevx.8.031022](https://doi.org/10.1103/physrevx.8.031022) (2018).

[3] P. O’Malley, R. Babbush, I. Kivlichan, J. Romero, J. McClean, R. Barends, J. Kelly, P. Roushan, A. Tranter, N. Ding, B. Campbell, Y. Chen, Z. Chen, B. Chiaro, A. Dunsworth, A. Fowler, E. Jeffrey, E. Lucero, A. Megrant, J. Mutus, M. Neeley, C. Neill, C. Quintana, D. Sank, A. Vainsencher, J. Wenner, T. White, P. Coveney, P. Love, H. Neven, A. Aspuru-Guzik, and J. Martinis, Scalable quantum simulation of molecular energies, *Physical Review X* **6**, [10.1103/physrevx.6.031007](https://doi.org/10.1103/physrevx.6.031007) (2016).

[4] A. Peruzzo, J. McClean, P. Shadbolt, M.-H. Yung, X.-Q. Zhou, P. J. Love, A. Aspuru-Guzik, and J. L. O’Brien, A variational eigenvalue solver on a photonic quantum processor, *Nature Communications* **5**, [10.1038/ncomms5213](https://doi.org/10.1038/ncomms5213) (2014).

[5] A. J. McCaskey, Z. P. Parks, J. Jakowski, S. V. Moore, T. D. Morris, T. S. Humble, and R. C. Pooser, Quantum chemistry as a benchmark for near-term quantum computers, *npj Quantum Information* **5** (2019).

[6] K. Mesman, Z. Al-Ars, and M. Möller, Qpack: Quantum approximate optimization algorithms as universal benchmark for quantum computers (2022), [arXiv:2103.17193](https://arxiv.org/abs/2103.17193) [cs.ET].

[7] D. Mills, S. Sivarajah, T. L. Scholten, and R. Duncan, Application-motivated, holistic benchmarking of a full quantum computing stack, *Quantum* **5**, 415 (2021).

[8] R. Hamerly, T. Inagaki, P. L. McMahon, D. Venturelli, A. Marandi, T. Onodera, E. Ng, C. Langrock, K. Inaba, T. Honjo, K. Enbutsu, T. Umeki, R. Kasahara, S. Utsunomiya, S. Kako, K.-i. Kawarabayashi, R. L. Byer, M. M. Fejer, H. Mabuchi, D. Englund, E. Rieffel, H. Takesue, and Y. Yamamoto, Experimental investigation of performance differences between coherent ising machines and a quantum annealer, *Science Advances* **5**, [10.1126/sciadv.aau0823](https://doi.org/10.1126/sciadv.aau0823) (2019).

[9] D. C. McKay, I. Hincks, E. J. Pritchett, M. Carroll, L. C. G. Govia, and S. T. Merkel, Benchmarking quantum processor performance at scale (2023), [arXiv:2311.05933](https://arxiv.org/abs/2311.05933) [quant-ph].

[10] J.-S. Chen, E. Nielsen, M. Ebert, V. Inlek, K. Wright, V. Chaplin, A. Maksymov, E. Páez, A. Poudel, P. Maunz, and J. Gamble, Benchmarking a trapped-ion quantum computer with 30 qubits, *Quantum* **8**, 1516 (2024).

[11] K. Wright, K. M. Beck, S. Debnath, J. M. Amini, Y. Nam, N. Grzesiak, J.-S. Chen, N. C. Pisenti, M. Chmielewski, C. Collins, K. M. Hudek, J. Mizrahi, J. D. Wong-Campos, S. Allen, J. Apisdorf, P. Solomon, M. Williams, A. M. Ducore, A. Blinov, S. M. Kreikemeier, V. Chaplin, M. Keesan, C. Monroe, and J. Kim, Benchmarking an 11-qubit quantum computer, *Nature Communications* **10**, [10.1038/s41467-019-13534-2](https://doi.org/10.1038/s41467-019-13534-2) (2019).

[12] P. Jurcevic, A. Javadi-Abhari, L. S. Bishop, I. Lauer, D. F. Bogorin, M. Brink, L. Capelluto, O. Günlük, T. Itoko, N. Kanazawa, A. Kandala, G. A. Keefe, K. Kruslich, W. Landers, E. P. Lewandowski, D. T. McClure, G. Nannicini, A. Narasgond, H. M. Nayfeh, E. Pritchett, M. B. Rothwell, S. Srinivasan, N. Sundaresan, C. Wang, K. X. Wei, C. J. Wood, J.-B. Yau, E. J. Zhang, O. E. Dial, J. M. Chow, and J. M. Gambetta, Demonstration of quantum volume 64 on a superconducting quantum computing system, *Quantum Science and Technology* **6**, [025020](https://doi.org/10.1088/2515-7691/abf300) (2021).

[13] N. M. Linke, D. Maslov, M. Roetteler, S. Debnath, C. Figgatt, K. A. Landsman, K. Wright, and C. Monroe, Experimental comparison of two quantum computing architectures, *Proceedings of the National Academy of Sciences* **114**, 3305–3310 (2017).

[14] L. Abdurakhimov, J. Adam, H. Ahmad, O. Ahonen, M. Algaba, G. Alonso, V. Bergholm, R. Berival, M. Beuerle, C. Bockstiegel, A. Calzona, C. F. Chan, D. Cucurachi, S. Dahl, R. Davletkaliyev, O. Fedorets, A. G. Frieiro, Z. Gao, J. Guldmyr, A. Guthrie, J. Hassel, H. Heimonen, J. Heinsoo, T. Hiltunen, K. Holland, J. Hotari, H. Hsu, A. Huhtala, E. Hyppä, A. Hämäläinen, J. Ikonen, S. Inel, D. Janzso, T. Jaakkola, M. Jenei, S. Jolin, K. Juliusson, J. Jussila, S. Khalid, S.-G. Kim, M. Koistinen, R. Kokkonieti, A. Komlev, C. Ockeloen-Korppi, O. Koskinen, J. Kotilahti, T. Kuisma, V. Kukushkin, K. Kumpulainen, I. Kuronen, J. Kylmälä, N. Lampinen, J. Lamprich, A. Landra, M. Leib, T. Li, P. Liebermann, A. Lintunen, W. Liu, J. Luus, F. Marxer, A. M. van de Griend, K. Mitra, J. K. Moqadam, J. Mrožek, H. Mäkinen, J. Mäntylä, T. Naaranoja, F. Nappi, J. Niemi, L. Ortega, M. Palma, M. Papič, M. Partanen, J. Penttilä, A. Plyushch, W. Qiu, A. Rath, K. Repo, T. Riipinen, J. Ritvas, P. F. Romero, J. Ruoho, J. Räbinä, S. Saarinen, I. Sagar, H. Sargsyan, M. Sarsby, N. Savola, M. Savytskyi, V. Selinmaa, P. Smirnov, M. M. Suárez, L. Sundström, S. Ślupińska, E. Takala, I. Takmakov, B. Tarasinski, M. Thapa, J. Tiainen, F. Tosto, J. Tuorila, C. Valenzuela, D. Vasey, E. Vehmaanperä, A. Vepsäläinen, A. Vienamo, P. Vesanan, A. Välimäa, J. Wesdorp, N. Wurz, E. Wybo, L. Yang, and A. Yurtalan, Technology and performance benchmarks of iqm’s 20-qubit quantum computer (2024), [arXiv:2408.12433](https://arxiv.org/abs/2408.12433) [quant-ph].

[15] N. Wagner, C. Poole, T. M. Graham, and M. Saffman, Benchmarking a neutral-atom quantum computer, *International Journal of Quantum Information* **22**, [10.1142/s0219749924500011](https://doi.org/10.1142/s0219749924500011) (2024).

[16] V. Galetsky, P. Kohl, and J. Nötzel, Photonic processor benchmarking for variational quantum process tomography (2025), [arXiv:2507.08570](https://arxiv.org/abs/2507.08570) [quant-ph].

[17] J. T. Selvam and S. S. Veni, Quantum circuit benchmarking on ibm brisbane: Performance insights from superconducting qubit models (2025), [arXiv:2508.05331](https://arxiv.org/abs/2508.05331) [quant-ph].

[18] G. J. Mooney, G. A. L. White, C. D. Hill, and L. C. L. Hollenberg, Generation and verification of 27-qubit greenberger-horne-zeilinger states in a superconducting quantum computer, *Journal of Physics Communications* **5**, 095004 (2021).

[19] S. Moses, C. Baldwin, M. Allman, R. Ancona, L. Ascarunz, C. Barnes, J. Bartolotta, B. Bjork, P. Blanchard, M. Bohn, J. Bohnet, N. Brown, N. Burdick, W. Burton, S. Campbell, J. Campora, C. Carron, J. Chambers, J. Chan, Y. Chen, A. Chernoguzov, E. Chertkov, J. Colina, J. Curtis, R. Daniel, M. DeCross, D. Deen, C. Delaney, J. Dreiling, C. Erts-

gaard, J. Esposito, B. Estey, M. Fabrikant, C. Figgatt, C. Foltz, M. Foss-Feig, D. Francois, J. Gaebler, T. Gatterman, C. Gilbreth, J. Giles, E. Glynn, A. Hall, A. Hankin, A. Hansen, D. Hayes, B. Higashi, I. Hoffman, B. Horning, J. Hout, R. Jacobs, J. Johansen, L. Jones, J. Karcz, T. Klein, P. Lauria, P. Lee, D. Liefer, S. Lu, D. Lucchetti, C. Lytle, A. Malm, M. Matheny, B. Mathewson, K. Mayer, D. Miller, M. Mills, B. Neyenhuis, L. Nugent, S. Olson, J. Parks, G. Price, Z. Price, M. Pugh, A. Ransford, A. Reed, C. Roman, M. Rowe, C. Ryan-Anderson, S. Sanders, J. Sedlacek, P. Shevchuk, P. Siegfried, T. Skripka, B. Spaun, R. Sprenkle, R. Stutz, M. Swallows, R. Tobey, A. Tran, T. Tran, E. Vogt, C. Volin, J. Walker, A. Zolot, and J. Pino, A race-track trapped-ion quantum processor, *Physical Review X* **13**, 10.1103/physrevx.13.041052 (2023).

[20] A. Chatterjee, S. Rappaport, A. Giri, S. Johri, T. Proctor, D. E. B. Neira, P. Sathe, and T. Lubinski, A comprehensive cross-model framework for benchmarking the performance of quantum hamiltonian simulations, *IEEE Transactions on Quantum Engineering* **6**, 1–26 (2025).

[21] H. Donkers, K. Mesman, Z. Al-Ars, and M. Möller, Qpack scores: Quantitative performance metrics for application-oriented quantum computer benchmarking (2022), arXiv:2205.12142 [quant-ph].

[22] A. Rozanov, B. Bantysh, I. Bobrov, G. Struchalin, and S. Straupe, Benchmarking single-qubit gates on a neutral atom quantum processor (2025), arXiv:2509.06881 [quant-ph].

[23] K. J. Mesman, W. van der Schoot, M. Möller, and N. M. P. Neumann, Quas: Quantum application score for benchmarking the utility of quantum computers (2024), arXiv:2406.03905 [quant-ph].

[24] T. Tomesh, P. Gokhale, V. Omole, G. Ravi, K. N. Smith, J. Viszlai, X. Wu, N. Hardavellas, M. R. Martonosi, and F. T. Chong, Supermarq: A scalable quantum benchmark suite, in *2022 IEEE International Symposium on High-Performance Computer Architecture (HPCA)* (IEEE Computer Society, Los Alamitos, CA, USA, 2022) pp. 587–603.

[25] E. Granet and H. Dreyer, AppQSim: Application-oriented benchmarks for Hamiltonian simulation on a quantum computer, arXiv:2503.04298 [quant-ph] (2025), available at arXiv:2503.04298.

[26] T. Lubinski, S. Johri, P. Varosy, J. Coleman, L. Zhao, J. Necaise, C. H. Baldwin, K. Mayer, and T. Proctor, Application-oriented performance benchmarks for quantum computing, *IEEE Transactions on Quantum Engineering* **4**, 1–32 (2023).

[27] T. Lubinski, J. J. Goings, K. Mayer, S. Johri, N. Reddy, A. Mehta, N. Bhatia, S. Rappaport, D. Mills, C. H. Baldwin, L. Zhao, A. Barbosa, S. Maity, and P. S. Mundada, Quantum algorithm exploration using application-oriented performance benchmarks (2024), arXiv:2402.08985 [quant-ph].

[28] N. Quetschlich, L. Burgholzer, and R. Wille, MQT Bench: Benchmarking Software and Design Automation Tools for Quantum Computing, *Quantum* **7**, 1062 (2023).

[29] F. Barbaresco, L. Rioux, C. Labreuche, M. Nowak, N. Olivier, D. Nicolazic, O. Hess, A.-L. Guilmot, R. Wang, T. Sassolas, S. Louise, K. Snizhko, G. Misguich, A. Auffèves, R. Whitney, E. Vergnaud, and F. Schopfer, Bacq – application-oriented benchmarks for quantum computing (2024), arXiv:2403.12205 [quant-ph].

[30] T. Patel, A. Potharaju, B. Li, R. B. Roy, and D. Tiwari, Experimental evaluation of nisq quantum computers: Error measurement, characterization, and implications, in *SC20: International Conference for High Performance Computing, Networking, Storage and Analysis* (2020) pp. 1–15.

[31] P. Murali, N. M. Linke, M. Martonosi, A. Javadi-Abhari, N. H. Nguyen, and C. H. Alderete, Full-stack, real-system quantum computer studies: Architectural comparisons and design insights, *2019 ACM/IEEE 46th Annual International Symposium on Computer Architecture (ISCA)* , 527 (2019).

[32] G. Ferro, O. Odubanjo, D. Andrade, and A. Gómez, Tnbs: A kernel-based benchmarking for digital quantum computers, in *Euro-Par 2024: Parallel Processing Workshops: Euro-Par 2024 International Workshops, Madrid, Spain, August 26–30, 2024, Proceedings, Part I* (Springer-Verlag, Berlin, Heidelberg, 2025) p. 28–39.

[33] N. P. Sawaya, D. Marti-Dafcik, Y. Ho, D. P. Tabor, D. E. B. Neira, A. B. Magann, S. Premaratne, P. Dubey, A. Matsuura, N. Bishop, W. A. d. Jong, S. Benjamin, O. Parekh, N. Tubman, K. Klymko, and D. Camps, Hamlib: A library of hamiltonians for benchmarking quantum algorithms and hardware, *Quantum* **8**, 1559 (2024).

[34] K. Kurowski, P. Rydlichowski, K. Wojciechowski, T. Pecyna, and M. Słysz, Application performance benchmarks for quantum computers (2023), arXiv:2310.13637 [cs.PF].

[35] T. Proctor, K. Young, A. D. Baczewski, and R. Blume-Kohout, Benchmarking quantum computers, *Nature Reviews Physics* **7**, 105 (2025), perspective, Published: 07 January 2025.

[36] M. Amico, H. Zhang, P. Jurcevic, L. S. Bishop, P. Nation, A. Wack, and D. C. McKay, Defining standard strategies for quantum benchmarks (2023), arXiv:2303.02108 [quant-ph].

[37] A. Hashim, L. B. Nguyen, N. Goss, B. Marinelli, R. K. Naik, T. Chistolini, J. Hines, J. P. Marceaux, Y. Kim, P. Gokhale, T. Tomesh, S. Chen, L. Jiang, S. Ferreacin, K. Rudinger, T. Proctor, K. C. Young, R. Blume-Kohout, and I. Siddiqi, A practical introduction to benchmarking and characterization of quantum computers (2024), arXiv:2408.12064 [quant-ph].

[38] J. M. Lorenz, T. Monz, J. Eisert, D. Reitzner, F. Schopfer, F. Barbaresco, K. Kurowski, W. van der Schoot, T. Strohm, J. Senellart, C. M. Perrault, M. Knufinke, Z. Amodjee, and M. Giardini, Systematic benchmarking of quantum computers: status and recommendations (2025), arXiv:2503.04905 [quant-ph].

[39] C. Kai-Uwe Becker, N. Tcholtchev, I.-D. Gheorghe-Pop, S. Bock, R. Seidel, and M. Hauswirth, Towards a quantum benchmark suite with standardized kpis, in *2022 IEEE 19th International Conference on Software Architecture Companion (ICSA-C)* (2022) pp. 160–163.

[40] IEEE - P7131. Standard for Quantum Computing Performance Metrics & Performance Benchmarking (2021).

[41] D. Gottesman, Theory of fault-tolerant quantum computation, *Phys. Rev. A* **57**, 127 (1998).

[42] Oeis sequence a003956, <https://oeis.org/A003956> (1964), Último acceso: 2025-10-03.

[43] D. Gottesman, *The heisenberg representation of quantum computers* (1998), arXiv:quant-ph/9807006 [quant-ph].

[44] N. Rengaswamy, R. Calderbank, S. Kadhe, and H. D. Pfister, Logical clifford synthesis for stabilizer codes, *IEEE Transactions on Quantum Engineering* **1**, 1–17 (2020).

[45] H.-Y. Huang, R. Kueng, and J. Preskill, Predicting many properties of a quantum system from very few measurements, *Nature Physics* **16**, 1050–1057 (2020).

[46] M. West, A. A. Mele, M. Larocca, and M. Cerezo, *Real classical shadows* (2025), arXiv:2410.23481 [quant-ph].

[47] C. H. Bennett, G. Brassard, S. Popescu, B. Schumacher, J. A. Smolin, and W. K. Wootters, Purification of noisy entanglement and faithful teleportation via noisy channels, *Physical Review Letters* **76**, 722–725 (1996).

[48] D. Bruß, Optimal eavesdropping in quantum cryptography with six states, *Physical Review Letters* **81**, 3018–3021 (1998).

[49] M. Hillery, V. Bužek, and A. Berthiaume, Quantum secret sharing, *Physical Review A* **59**, 1829–1834 (1999).

[50] J. Emerson, R. Alicki, and K. Życzkowski, Scalable noise estimation with random unitary operators, *Journal of Optics B: Quantum and Semiclassical Optics* **7**, S347–S352 (2005).

[51] C. Dankert, R. Cleve, J. Emerson, and E. Livine, Exact and approximate unitary 2-designs and their application to fidelity estimation, *Phys. Rev. A* **80**, 012304 (2009).

[52] E. Knill, D. Leibfried, R. Reichle, J. Britton, R. B. Blakestad, J. D. Jost, C. Langer, R. Ozeri, S. Seidelin, and D. J. Wineland, Randomized benchmarking of quantum gates, *Phys. Rev. A* **77**, 012307 (2008).

[53] I. L. Chuang and M. A. Nielsen, Prescription for experimental determination of the dynamics of a quantum black box, *Journal of Modern Optics* **44**, 2455–2467 (1997).

[54] J. F. Poyatos, J. I. Cirac, and P. Zoller, Complete characterization of a quantum process: The two-bit quantum gate, *Phys. Rev. Lett.* **78**, 390 (1997).

[55] E. Magesan, J. M. Gambetta, and J. Emerson, Scalable and robust randomized benchmarking of quantum processes, *Phys. Rev. Lett.* **106**, 180504 (2011).

[56] A. M. Polloreno, A. Carignan-Dugas, J. Hines, R. Blume-Kohout, K. Young, and T. Proctor, *A theory of direct randomized benchmarking* (2023), arXiv:2302.13853 [quant-ph].

[57] J. Hines, D. Hothem, R. Blume-Kohout, B. Whaley, and T. Proctor, Fully scalable randomized benchmarking without motion reversal, *PRX Quantum* **5**, 030334 (2024).

[58] T. Proctor, S. Seritan, K. Rudinger, E. Nielsen, R. Blume-Kohout, and K. Young, Scalable randomized benchmarking of quantum computers using mirror circuits, *Phys. Rev. Lett.* **129**, 150502 (2022).

[59] F. Arute, K. Arya, R. Babbush, D. Bacon, J. C. Bardin, R. Barends, R. Biswas, S. Boixo, F. G. S. L. Brando, D. A. Buell, B. Burkett, Y. Chen, Z. Chen, B. Chiaro, R. Collins, W. Courtney, A. Dunsworth, E. Farhi, B. Foxen, A. Fowler, C. Gidney, M. Giustina, R. Graff, K. Guerin, S. Habegger, M. P. Harrigan, M. J. Hartmann, A. Ho, M. Hoffmann, T. Huang, T. S. Humble, S. V. Isakov, E. Jeffrey, Z. Jiang, D. Kafri, K. Kechedzhi, J. Kelly, P. V. Klimov, S. Knysh, A. Korotkov, F. Kostritsa, D. Landhuis, M. Lindmark, E. Lucero, D. Lyakh, S. Mandrà, J. R. McClean, M. McEwen, A. Megrant, X. Mi, K. Michielsen, M. Mohseni, J. Mutus, O. Naaman, M. Neeley, C. Neill, M. Y. Niu, E. Ostby, A. Petukhov, J. C. Platt, C. Quintana, E. G. Rieffel, P. Roushan, N. C. Rubin, D. Sank, K. J. Satzinger, V. Smelyanskiy, K. J. Sung, M. D. Trevithick, A. Vainsencher, B. Villalonga, T. White, Z. J. Yao, P. Yeh, A. Zalcman, H. Neven, and J. M. Martinis, Quantum supremacy using a programmable superconducting processor, *Nature* **574**, 505–510 (2019).

[60] A. Carignan-Dugas, J. J. Wallman, and J. Emerson, Characterizing universal gate sets via dihedral benchmarking, *Phys. Rev. A* **92**, 060302 (2015).

[61] J. Helsen, X. Xue, L. M. K. Vandersypen, and S. Wehner, A new class of efficient randomized benchmarking protocols (2019), arXiv:1806.02048 [quant-ph].

[62] J. M. Gambetta, A. D. Córcoles, S. T. Merkel, B. R. Johnson, J. A. Smolin, J. M. Chow, C. A. Ryan, C. Rigetti, S. Poletto, T. A. Ohki, M. B. Ketchen, and M. Steffen, Characterization of addressability by simultaneous randomized benchmarking, *Phys. Rev. Lett.* **109**, 240504 (2012).

[63] E. Magesan, J. M. Gambetta, B. R. Johnson, C. A. Ryan, J. M. Chow, S. T. Merkel, M. P. da Silva, G. A. Keefe, M. B. Rothwell, T. A. Ohki, M. B. Ketchen, and M. Steffen, Efficient measurement of quantum gate error by interleaved randomized benchmarking, *Phys. Rev. Lett.* **109**, 080505 (2012).

[64] A. Erhard, J. J. Wallman, L. Postler, M. Meth, R. Stricker, E. A. Martinez, P. Schindler, T. Monz, J. Emerson, and R. Blatt, Characterizing large-scale quantum computers via cycle benchmarking, *Nature Communications* **10**, 10.1038/s41467-019-13068-7 (2019).

[65] J. Wallman, C. Granade, R. Harper, and S. T. Flammia, Estimating the coherence of noise, *New Journal of Physics* **17**, 113020 (2015).

[66] G. Feng, J. J. Wallman, B. Buonacorsi, F. H. Cho, D. K. Park, T. Xin, D. Lu, J. Baugh, and R. Laflamme, Estimating the coherence of noise in quantum control of a solid-state qubit, *Phys. Rev. Lett.* **117**, 260501 (2016).

[67] J. J. Wallman, M. Barnhill, and J. Emerson, Robust characterization of leakage errors, *New Journal of Physics* **18**, 043021 (2016).

[68] S. T. Flammia and Y.-K. Liu, Direct fidelity estimation from few pauli measurements, *Physical Review Letters* **106**, 10.1103/physrevlett.106.230501 (2011).

[69] J. Hines, M. Lu, R. K. Naik, A. Hashim, J.-L. Ville, B. Mitchell, J. M. Kriekbaum, D. I. Santiago, S. Seritan, E. Nielsen, R. Blume-Kohout, K. Young, I. Siddiqi, B. Whaley, and T. Proctor, Demonstrating scalable randomized benchmarking of universal gate sets, *Phys. Rev. X* **13**, 041030 (2023).

[70] J. Richard and L. Noah, On the role of entanglement in quantum-computational speed-up, *Proceedings of the Royal Society A* **459**, 2011 (2003).

[71] D. M. Greenberger, M. A. Horne, and A. Zeilinger, Going Beyond Bell's Theorem, in *Bell's Theorem, Quantum Theory and Conceptions of the Universe*, Fundamental Theories of Physics, Vol. 37, edited by M. Kafatos (Springer Dordrecht, 1989) pp. 69–72.

[72] E. Knill, Quantum computing with realistically noisy devices, *Nature* **434**, 39 (2005).

[73] L. Pezzè, A. Smerzi, M. K. Oberthaler, R. Schmied, and P. Treutlein, Quantum metrology with nonclassical states of atomic ensembles, *Reviews of Modern Physics* **90**, 035005 (2018).

[74] P. Espoukeh and P. Pedram, Quantum teleportation through noisy channels with multi-qubit GHZ states, *Quantum Information Processing* **13**, 1789 (2014).

[75] S. A. Moses *et al.*, A Race-Track Trapped-Ion Quantum Processor, *Physical Review X* **13**, 041052 (2023).

[76] T. Monz, P. Schindler, J. T. Barreiro, M. Chwalla, D. Nigg, W. A. Coish, M. Harlander, W. Hänsel, M. Hennrich, and R. Blatt, 14-Qubit Entanglement: Creation and Coherence, *Physical Review Letters* **106**, 130506 (2011).

[77] C. Song, K. Xu, H. Li, Y.-R. Zhang, X. Zhang, W. Liu, Q. Guo, Z. Wang, W. Ren, J. Hao, H. Feng, H. Fan, D. Zheng, D.-W. Wang, H. Wang, and S.-Y. Zhu, Generation of multicomponent atomic Schrödinger cat states of up to 20 qubits, *Science* **365**, 574 (2019).

[78] C. Song, K. Xu, W. Liu, C.-p. Yang, S.-B. Zheng, H. Deng, Q. Xie, K. Huang, Q. Guo, L. Zhang, P. Zhang, D. Xu, D. Zheng, X. Zhu, H. Wang, Y.-A. Chen, C.-Y. Lu, S. Han, and J.-W. Pan, 10-Qubit Entanglement and Parallel Logic Operations with a Superconducting Circuit, *Physical Review Letters* **119**, 180511 (2017).

[79] R. Barends, J. Kelly, A. Megrant, and *et al.*, Superconducting quantum circuits at the surface code threshold for fault tolerance, *Nature* **508**, 500 (2014).

[80] J. F. Kam, H. Kang, C. D. Hill, G. J. Mooney, and L. C. L. Hollenberg, Characterization of entanglement on superconducting quantum computers of up to 414 qubits, *Phys. Rev. Res.* **6**, 033155 (2024).

[81] A. Omran, H. Levine, A. Keesling, G. Semeghini, T. T. Wang, S. Ebadi, H. Bernien, A. S. Zibrov, H. Pichler, S. Choi, J. Cui, M. Rossignolo, P. Rembold, S. Montangero, T. Calarco, M. Endres, M. Greiner, V. Vuletić, and M. D. Lukin, Generation and manipulation of Schrödinger cat states in Rydberg atom arrays, *Science* **365**, 570 (2019).

[82] T. M. Graham, Y. Song, J. Scott, *et al.*, Multi-qubit entanglement and algorithms on a neutral-atom quantum computer, *Nature* **604**, 457 (2022).

[83] H.-S. Zhong, Y. Li, W. Li, L.-C. Peng, Z.-E. Su, Y. Hu, Y.-M. He, X. Ding, W. Zhang, H. Li, L. Zhang, Z. Wang, L. You, X.-L. Wang, X. Jiang, L. Li, Y.-A. Chen, N.-L. Liu, C.-Y. Lu, and J.-W. Pan, 12-Photon Entanglement and Scalable Scattershot Boson Sampling with Optimal Entangled-Photon Pairs from Parametric Down-Conversion, *Physical Review Letters* **121**, 250505 (2018).

[84] X.-L. Wang, L.-K. Chen, W. Li, H.-L. Huang, C. Liu, C. Chen, Y.-H. Luo, Z.-E. Su, D. Wu, Z.-D. Li, H. Lu, Y. Hu, X. Jiang, C.-Z. Peng, L. Li, N.-L. Liu, Y.-A. Chen, C.-Y. Lu, and J.-W. Pan, Experimental Ten-Photon Entanglement, *Physical Review Letters* **117**, 210502 (2016).

[85] K. Takeda, A. Noiri, T. Nakajima, T. Kobayashi, and S. Tarucha, Quantum error correction with silicon spin qubits, *Nature* **608**, 682 (2022).

[86] A. Ozaeta and P. L. McMahon, Decoherence of up to 8-qubit entangled states in a 16-qubit superconducting quantum processor, *Quantum Science and Technology* **4**, 025015 (2019).

[87] D. Cruz, R. Fournier, F. Gremion, A. Jeannerot, K. Komagata, T. Tasic, J. Thiesbrummel, C. L. Chan, N. Macris, M.-A. Dupertuis, and C. Javerzac-Galy, Efficient Quantum Algorithms for GHZ and W States, and Implementation on the IBM Quantum Computer, *Advanced Quantum Technologies* **2**, 1900015 (2019).

[88] R. Blatt and D. Wineland, Entangled states of trapped atomic ions, *Nature* **453**, 1008 (2008).

[89] G. J. Mooney, G. A. L. White, C. D. Hill, and L. C. L. Hollenberg, Generation and verification of 27-qubit Greenberger–Horne–Zeilinger states in a superconducting quantum computer, *Journal of Physics Communications* **5**, 095004 (2021).

[90] D. Leibfried, E. Knill, S. Seidelin, and *et al.*, Creation of a six-atom ‘Schrödinger cat’ state, *Nature* **438**, 639 (2005).

[91] K. X. Wei, I. Lauer, S. Srinivasan, N. Sundaresan, D. T. McClure, D. Toyli, D. C. McKay, J. M. Gambetta, and S. Sheldon, Verifying multipartite entangled Greenberger–Horne–Zeilinger states via multiple quantum coherences, *Physical Review A* **101**, 032343 (2020).

[92] H.-Y. Huang, R. Kueng, and J. Preskill, Predicting many properties of a quantum system from very few measurements, *Nature Physics* **16**, 1050 (2020).

[93] H.-Y. Huang, J. Preskill, and M. Soleimanifar, Certifying almost all quantum states with few single-qubit measurements, *Nat. Phys.* (2025).

[94] D. Gottesman, The heisenberg representation of quantum computers, in *Group 22: Proceedings of the 12th International Colloquium on Group Theoretical Methods in Physics*, edited by S. P. Corney, R. Delbourgo, and P. D. Jarvis (International Press of Boston, Cambridge, Massachusetts, 1999) pp. 32–43.

[95] O. Gühne and M. Seevinck, Separability criteria for genuine multiparticle entanglement, *New Journal of Physics* **12**, 053002 (2010).

[96] R. P. Feynman, Simulating physics with computers, *International journal of theoretical physics* **21**, 467 (1982).

[97] S. McArdle, S. Endo, A. Aspuru-Guzik, S. C. Benjamin, and X. Yuan, Quantum computational chemistry, *Rev. Mod. Phys.* **92**, 015003 (2020).

[98] Y. Cao, J. Romero, J. P. Olson, M. Degroote, P. D. Johnson, M. Kieferová, I. D. Kivlichan, T. Menke, B. Peropadre, N. P. D. Sawaya, S. Sim, L. Veis, and A. Aspuru-Guzik, Quantum chemistry in the age of quantum computing, *Chemical Reviews* **119**, 10856–10915 (2019).

[99] B. Bauer, S. Bravyi, M. Motta, and G. K.-L. Chan, Quantum algorithms for quantum chemistry and quantum materials science, *Chemical Reviews* **120**, 12685–12717 (2020).

[100] P. J. Ollitrault, A. Miessen, and I. Tavernelli, Molecular quantum dynamics: A quantum computing perspective, *Accounts of Chemical Research* **54**, 4229 (2021).

[101] A. B. Magann, M. D. Grace, H. A. Rabitz, and M. Sarovar, Digital quantum simulation of molecular dynamics and control, *Phys. Rev. Res.* **3**, 023165 (2021).

[102] L. Bassman Oftelie, M. Urbanek, M. Metcalf, J. Carter, A. F. Kemper, and W. A. de Jong, Simulating quantum materials with digital quantum computers, *Quantum Science and Technology* **6**, 043002 (2021).

[103] L. Bassman Oftelie, K. Liu, A. Krishnamoorthy, T. Linker, Y. Geng, D. Shebib, S. Fukushima, F. Shi-

mojo, R. K. Kalia, A. Nakano, and P. Vashishta, Towards simulation of the dynamics of materials on quantum computers, *Physical Review B* **101**, 10.1103/physrevb.101.184305 (2020).

[104] N. Maskara, S. Ostermann, J. Shee, M. Kalinowski, A. McClain Gomez, R. Araiza Bravo, D. S. Wang, A. I. Krylov, N. Y. Yao, M. Head-Gordon, M. D. Lukin, S. F. Yelin, *et al.*, Programmable simulations of molecules and materials with reconfigurable quantum processors, *Nature Physics* **21**, 289 (2025).

[105] B. Fausewöh, Quantum many-body simulations on digital quantum computers: State-of-the-art and future challenges, *Nature Communications* **15**, 2123 (2024).

[106] J. Tilly, H. Chen, *et al.*, Simulating quantum many-body dynamics on a current digital quantum computer, *npj Quantum Information* **5**, 79 (2019).

[107] S. Lloyd, Universal quantum simulators, *Science* **273**, 1073 (1996).

[108] W. T. Buttler, S. K. Lamoreaux, and J. R. Torgerson, Practical four-dimensional quantum key distribution without entanglement, *Quantum Information and Computation* **12**, 1–8 (2012).

[109] A. M. Childs and N. Wiebe, Hamiltonian simulation using linear combinations of unitary operations, *Quantum Info. Comput.* **12**, 901–924 (2012).

[110] G. H. Low and I. L. Chuang, Optimal hamiltonian simulation by quantum signal processing, *Physical Review Letters* **118**, 10.1103/physrevlett.118.010501 (2017).

[111] G. H. Low and I. L. Chuang, Hamiltonian simulation by qubitization, *Quantum* **3**, 163 (2019).

[112] J. M. Martyn, Z. M. Rossi, A. K. Tan, and I. L. Chuang, Grand unification of quantum algorithms, *PRX Quantum* **2**, 10.1103/prxquantum.2.040203 (2021).

[113] A. Gilyén, Y. Su, G. H. Low, and N. Wiebe, Quantum singular value transformation and beyond: exponential improvements for quantum matrix arithmetics, in *Proceedings of the 51st Annual ACM SIGACT Symposium on Theory of Computing*, STOC 2019 (Association for Computing Machinery, New York, NY, USA, 2019) p. 193–204.

[114] P. Pfeuty, The one-dimensional ising model with a transverse field, *Annals of Physics* **57**, 79 (1970).

[115] M. Farreras and A. Cervera-Lierta, Simulation of the 1d xy model on a quantum computer, *SciPost Physics Lecture Notes* **10.21468/scipostphyslectnotes.95** (2025).

[116] J. Biamonte, P. Wittek, N. Pancotti, P. Rebentrost, N. Wiebe, and S. Lloyd, Quantum machine learning, *Nature* **549**, 195–202 (2017).

[117] A. Abbas, D. Sutter, C. Zoufal, A. Lucchi, A. Figalli, and S. Woerner, The power of quantum neural networks, *Nature Computational Science* **1**, 403–409 (2021).

[118] Y. Du, Y. Yang, D. Tao, and M.-H. Hsieh, Problem-dependent power of quantum neural networks on multi-class classification, *Phys. Rev. Lett.* **131**, 140601 (2023).

[119] A. Senokosov, A. Sedykh, A. Sagingalieva, B. Kyriacou, and A. Melnikov, Quantum machine learning for image classification, *Machine Learning: Science and Technology* **5**, 015040 (2024).

[120] M. P. Henderson, S. Shakya, S. Pradhan, and T. Cook, Quanvolutional neural networks: powering image recognition with quantum circuits, *Quantum Machine Intelligence* **2** (2019).

[121] G. Li, X. Zhao, and X. Wang, Quantum self-attention neural networks for text classification, *Science China Information Sciences* **67** (2022).

[122] Y. Couzinié, S. Daimon, H. Nishi, N. Ito, Y. Harazono, and Y. ichiro Matsushita, Towards improved quantum machine learning for molecular force fields (2025), [arXiv:2505.03213 \[physics.chem-ph\]](https://arxiv.org/abs/2505.03213).

[123] M. Vitz, H. Mohammadbagherpoor, S. Sandeep, A. Vlasic, R. Padbury, and A. Pham, Hybrid quantum graph neural network for molecular property prediction (2024), [arXiv:2405.05205 \[quant-ph\]](https://arxiv.org/abs/2405.05205).

[124] S. Mourya, H. Leipold, and B. Adhikari, Contextual quantum neural networks for stock price prediction (2025), [arXiv:2503.01884 \[cs.LG\]](https://arxiv.org/abs/2503.01884).

[125] J. Landman, N. Mathur, Y. Y. Li, M. Strahm, S. Kazdaghli, A. Prakash, and I. Kerenidis, Quantum Methods for Neural Networks and Application to Medical Image Classification, *Quantum* **6**, 881 (2022).

[126] J. M. Kübler, S. Buchholz, and B. Schölkopf, The inductive bias of quantum kernels (2021), [arXiv:2106.03747 \[quant-ph\]](https://arxiv.org/abs/2106.03747).

[127] S. Naguleswaran, Quantum machine learning: Quantum kernel methods (2024), [arXiv:2405.01780 \[quant-ph\]](https://arxiv.org/abs/2405.01780).

[128] N. Meyer, C. Ufrecht, M. Periyasamy, D. D. Scherer, A. Plinge, and C. Mutschler, A survey on quantum reinforcement learning (2024), [arXiv:2211.03464 \[quant-ph\]](https://arxiv.org/abs/2211.03464).

[129] M. Islam, S. Turkeli, and F. Ozaydin, A survey of quantum generative adversarial networks: Architectures, use cases, and real-world implementations (2025), [arXiv:2506.18002 \[quant-ph\]](https://arxiv.org/abs/2506.18002).

[130] A. Pérez-Salinas, A. Cervera-Lierta, E. Gil-Fuster, and J. I. Latorre, Data re-uploading for a universal quantum classifier, *Quantum* **4**, 226 (2020).

[131] M.-G. Zhou, Z.-P. Liu, H.-L. Yin, C.-L. Li, T.-K. Xu, and Z.-B. Chen, Quantum neural network for quantum neural computing, *Research* **6**, 10.34133/research.0134 (2023).

[132] J. R. McClean, S. Boixo, V. N. Smelyanskiy, R. Babbush, and H. Neven, Barren plateaus in quantum neural network training landscapes, *Nature Communications* **9**, 10.1038/s41467-018-07090-4 (2018).

[133] M. Ragone, B. N. Bakalov, F. Sauvage, A. F. Kemper, C. Ortiz Marrero, M. Larocca, and M. Cerezo, A lie algebraic theory of barren plateaus for deep parameterized quantum circuits, *Nature Communications* **15**, 10.1038/s41467-024-49909-3 (2024).

[134] A. Pérez-Salinas, D. López-Núñez, A. García-Sáez, P. Forn-Díaz, and J. I. Latorre, One qubit as a universal approximant, *Physical Review A* **104**, 10.1103/physreva.104.012405 (2021).

[135] I. Panadero, Y. Ban, H. Espinós, R. Puebla, J. Casanova, and E. Torrontegui, Regressions on quantum neural networks at maximal expressivity (2023), [arXiv:2311.06090 \[quant-ph\]](https://arxiv.org/abs/2311.06090).

[136] P. Rodriguez-Grasa, Y. Ban, and M. Sanz, Neural quantum kernels: Training quantum kernels with quantum neural networks, *Phys. Rev. Res.* **7**, 023269 (2025).

[137] M. Schuld, V. Bergholm, C. Gogolin, J. Izaac, and N. Killoran, Evaluating analytic gradients on quantum hardware, *Physical Review A* **99**, 10.1103/physreva.99.032331 (2019).

[138] D. Wierichs, J. Izaac, C. Wang, and C. Y.-Y. Lin, General parameter-shift rules for quantum gradients, *Quantum* **6**, 677 (2022).

[139] D. A. Escarabajal, Data re-uploading quantum neural network binary datasets, Zenodo (2025), doi: <https://doi.org/10.5281/zenodo.5900000>

10.5281/zenodo.17966787.

[140] D. S. Bagaev, M. A. Gavreev, A. S. Mastiukova, A. K. Fedorov, and N. A. Nemkov, [Regularizing quantum loss landscapes by noise injection](#) (2025), arXiv:2505.08759 [quant-ph].

[141] W. Somogyi, E. Pankovets, V. Kuzmin, and A. Melnikov, [Method for noise-induced regularization in quantum neural networks](#) (2024), arXiv:2410.19921 [quant-ph].

[142] M. Mottonen, J. J. Vartiainen, V. Bergholm, and M. M. Salomaa, [Transformation of quantum states using uniformly controlled rotations](#) (2004), arXiv:quant-ph/0407010 [quant-ph].

[143] Y. Dong, L. Lin, H. Ni, and J. Wang, [Robust iterative method for symmetric quantum signal processing in all parameter regimes](#) (2023), arXiv:2307.12468 [quant-ph].

Appendix A: Partial Clifford Randomized Benchmark is reliable if the probability of error cancellation is negligible

We follow the same ideas as in section IV of Ref. [56]. For this analysis, we make two assumptions. First, we neglect state-preparation and measurement (SPAM) errors, and focus exclusively on the errors introduced by the circuit implementation. Second, we assume that stochastic Pauli errors are dominant. In particular, we assume that after the application of one layer L of a μ -fraction random Clifford circuit, a Pauli error may occur with some probability. Formally, let $\{\epsilon_{L,P}\}_{P \in \mathcal{P}_N}$ denote the probability distribution over all Pauli strings $P \in \mathcal{P}_N$ acting on N qubits, where $\epsilon_{L,P}$ is the probability that P occurs after the application of layer L . For fixed L , this distribution satisfies

$$\sum_{P \in \mathcal{P}_N} \epsilon_{L,P} = 1. \quad (\text{A1})$$

The probability that no error occurs after the application of layer L is given by $\epsilon_{L,I}$. Consequently, the probability of an error is

$$\sum_{P \in \mathcal{P}_N, P \neq I} \epsilon_{L,P} = \epsilon_L. \quad (\text{A2})$$

It is straightforward to show that ϵ_L corresponds to the entanglement infidelity between the ideal and noisy implementations of $U(L)$ under this error model. Specifically,

$$\epsilon_L = 1 - F_e(\mathcal{U}(L), \Phi(L)) = 1 - \frac{1}{4^N} \text{Tr}(\mathcal{U}(L)^\dagger \Phi(L)), \quad (\text{A3})$$

where $\mathcal{U}(L)$ is the superoperator representing the ideal implementation of $U(L)$, and $\Phi(L)$ is the noisy superoperator incorporating the Pauli errors. We define the mean entanglement infidelity as

$$\epsilon_\mu = \mathbb{E}_{L \in C_\mu}(\epsilon_L), \quad (\text{A4})$$

where C_μ denotes the set of all μ -fraction circuits for a fixed μ .

Consider the n -qubit circuit defined in Protocol 1. Assuming perfect state preparation and measurement, and a total of d layers, the outcome under the stochastic Pauli error model is given by

$$B_d = \text{Tr}\left(U(L_1 \cdots L_d) P U(L_1 \cdots L_d)^\dagger \tilde{U}(L_1 \cdots L_d) |\psi(P)\rangle\langle\psi(P)| \tilde{U}(L_1 \cdots L_d)^\dagger\right) \quad (\text{A5})$$

$$= \langle\psi(P)| \tilde{U}(L_1 \cdots L_d)^\dagger U(L_1 \cdots L_d) P U(L_1 \cdots L_d)^\dagger \tilde{U}(L_1 \cdots L_d) |\psi(P)\rangle. \quad (\text{A6})$$

Here,

$$U(L_1 \cdots L_d) = U(L_d) \cdots U(L_1), \quad \tilde{U}(L_1 \cdots L_d) = P_d U(L_d) P_{d-1} U(L_{d-1}) \cdots P_1 U(L_1), \quad (\text{A7})$$

where each $U(L_i)$ is drawn at random and each P_i is a Pauli string occurring with probability ϵ_{L_i, P_i} , which depends on L_i . The operator P is a Pauli string chosen uniformly at random (with a random \pm sign), and $|\psi(P)\rangle$ is a stabilizer state of P , modeled as a random variable independent of the circuit layers.

We now compute the expected value of B_d with respect to the choice of layers L_1, \dots, L_d , the initial Pauli string P , and the stabilizer state $|\psi(P)\rangle$.

$$F_d = \mathbb{E}_{L_1, \dots, L_d, P, |\psi(P)\rangle}(B_d). \quad (\text{A8})$$

The quantity F_d is the value estimated by repeating the experiment multiple times. In what follows, we show that F_d can be used to estimate ϵ_μ under certain conditions.

Since all the $U(L_i)$ are Clifford unitaries, we can express

$$\tilde{U}(L_1 \cdots L_d) = \tilde{P}U(L_1 \cdots L_d), \quad (\text{A9})$$

where \tilde{P} is a Pauli-operator-valued random variable. The operator \tilde{P} is obtained by commuting each P_i through the subsequent Clifford layers and then multiplying all the resulting operators together. Therefore, we can write

$$B_d = \langle \psi(P) | U(L_1 \cdots L_d)^\dagger \tilde{P}U(L_1 \cdots L_d) PU(L_1 \cdots L_d)^\dagger \tilde{P}U(L_1 \cdots L_d) | \psi(P) \rangle \quad (\text{A10})$$

$$= \langle \psi(P) | \tilde{P}'P\tilde{P}' | \psi(P) \rangle \quad (\text{A11})$$

where $\tilde{P}' = U(L_1 \cdots L_d)^\dagger \tilde{P}U(L_1 \cdots L_d)$. The quantity B_d equals 1 whenever at least one of the following situations occurs:

S1 All the $P_i = I$ which implies that $\tilde{P} = I$ and finally $\tilde{P}' = I$.

S2 Not all P_i are equal to I , but they cancel each other out, so that ultimately $\tilde{P} = I$ and $\tilde{P}' = I$.

S3 \tilde{P}' and P commutes.

If we denote by S the event that $B_d = 1$, then we can see that

$$F_d = \mathbb{E}_{L_1, \dots, L_d, P, |\psi(P)\rangle} (B_d) = \Pr_d(S) - (1 - \Pr_d(S)) = 2\Pr_d(S) - 1 \quad (\text{A12})$$

where the probability of S can be expressed in terms of the events *S1*, *S2*, and *S3* as

$$\Pr(S) = \Pr_d(S1) + \Pr_d(S2) + \Pr_d(S3) \quad (\text{A13})$$

Using basic probability theory we have that

$$\Pr_d(S) = s_1 + s_2 + (1 - s_1 - s_2)s_3 \quad (\text{A14})$$

where

$$s_1 = \Pr_d(S1), s_2 = \Pr_d(S2), s_3 = \Pr_d(S3 | \overline{S1} \cap \overline{S2}) \quad (\text{A15})$$

We now proceed to analyze each term, beginning with s_3 . By definition of s_3 , we have $\tilde{P}' \neq I$. Here, \tilde{P}' represents a Pauli operator resulting from the random errors P_i and can thus be treated as a random variable independent of the Pauli operator P . Since P is selected uniformly at random, the probability that two randomly chosen Pauli operators commute is $\frac{1}{2}$; this follows from the fact that, for any fixed Pauli operator, exactly half of all Paulis commute with it while the other half anticommute. Consequently, the contribution of s_3 is

$$s_3 = \frac{1}{2}. \quad (\text{A16})$$

The analysis of S_1 is also straightforward. The probability of no error occurring in a single layer is $1 - \epsilon_\mu$, so the probability of no errors over d layers is given by

$$s_1 = (1 - \epsilon_\mu)^d. \quad (\text{A17})$$

Substituting this expression into equation A14, and then using the result in equation A12, we obtain

$$F_d = \mathbb{E}_{L_1, \dots, L_d, P, |\psi(P)\rangle} (B_d) = 2\Pr_d(S) - 1 = 2(s_1 + s_2 + (1 - s_1 - s_2)s_3) - 1 \quad (\text{A18})$$

$$= s_1 + s_2 \quad (\text{A19})$$

$$= (1 - \epsilon_\mu)^d + s_2. \quad (\text{A20})$$

If $s_2 \approx 0$, then F_d will decay exponentially with d , allowing us to estimate ϵ_μ from this behavior. We note that this analysis does not account for state preparation and measurement errors. Since these errors are independent of the circuit depth d , they remain constant as the depth increases. Therefore, the final expression for the fidelity, including these errors, is

$$F = AF_d = A(1 - \epsilon_\mu)^d = Ap^d \quad (\text{A21})$$

This is the curve that we ultimately obtain with our procedure, from which we can estimate ϵ_μ .

We now analyze how s_2 can be upper-bounded in order to determine the conditions under which the obtained results are reliable.

1. Deriving a formula for error cancellation

We begin by analyzing the probability of observing exactly l errors in the noisy evolution $\tilde{U}(L_1 \cdots L_d)$. Since the probability of an error occurring after a single layer is ϵ_μ , the probability of obtaining l errors and $d - l$ error-free layers is given by

$$\Pr[l \text{ errors in } d \text{ layers}] = (1 - \epsilon_\mu)^{d-l} \epsilon_\mu^l \binom{d}{l}. \quad (\text{A22})$$

where the binomial coefficient accounts for the number of possible positions at which the errors can occur. To study error cancellation, we will reformulate this expression. First, observe that when a single error occurs, it cannot be canceled

$$U(L_d \cdots L_i) P_{i-1} U(L_{i-1} \cdots L_1) = U(L_d \cdots L_1) \implies P_{i-1} = I \quad (\text{A23})$$

where the equalities hold up to an overall phase factor.

We now assume that at least two errors occur, i.e., $l > 1$. To analyze this case, we reorganize the possible error configurations into groups according to the separation between the first and last errors in $\tilde{U}(L_1 \cdots L_d)$. Let this separation be k layers, with k ranging from $l - 1$ to $d - 1$.

First, consider fixing the positions of the first and last errors such that they are separated by k layers. It is straightforward to verify that there are $d - k$ possible choices for these two positions. Next, there are $k - 1$ intermediate positions available in which to place the remaining $l - 2$ errors, which can be done in $\binom{k-1}{l-2}$ distinct ways. Considering all possible separations k , the probability of observing $l > 1$ errors whose first and last occurrences are separated by k layers can be expressed as

$$(1 - \epsilon_\mu)^{d-l} \epsilon_\mu^l \sum_{k=l-1}^{d-1} (d - k) \binom{k-1}{l-2}. \quad (\text{A24})$$

Consider now the case where l errors occur and the two extreme errors, P_1 and P_{k+1} , which are both different from the identity, are separated by k layers. In this case, the evolution can be written as

$$U(L_d \cdots L_{i+k+1}) P_{k+1} U(L_{i+k}) P_k U(L_{i+k-1}) \cdots U(L_{i+2}) P_2 U(L_{i+1}) P_1 U(L_i \cdots L_1), \quad (\text{A25})$$

where only $l - 2$ of the operators P_2, \dots, P_k are non-identity Paulis. By commuting these $l - 2$ Pauli operators through the Clifford unitaries, they can be shifted to the left, resulting in an effective Pauli operator \tilde{P} acting at the same position as P_{k+1} , so that the expression becomes

$$U(L_d \cdots L_{i+k+1}) P_{k+1} \tilde{P} U(L_{i+k} \cdots L_{i+1}) P_1 U(L_i \cdots L_1). \quad (\text{A26})$$

Let us denote $P = P_1$ and $Q = P_{k+1} \tilde{P}$. In this notation, all of these gates cancel if and only if

$$U(L_d \cdots L_{i+k+1}) Q U(L_{i+k} \cdots L_{i+1}) P U(L_i \cdots L_1) = U(L_d \cdots L_1) \quad (\text{A27})$$

$$\iff U(L_{i+k} \cdots L_{i+1})^\dagger Q U(L_{i+k} \cdots L_{i+1}) = P, \quad (\text{A28})$$

up to an overall phase.

Since Q depends on the unitary block $U(L_{i+k} \cdots L_{i+1})$, while P depends only on $U(L_i)$, and these unitaries are chosen independently at random, $U(L_{i+k} \cdots L_{i+1})^\dagger Q U(L_{i+k} \cdots L_{i+1})$ and P can be regarded as independent. Hence, we can bound the probability of error cancellation between errors separated by k layers by computing

$$M_k = \max_{P, Q \in \mathcal{P} \setminus \{I\}} \left\{ \Pr_{L_1, \dots, L_k \mid \text{supp}(Q) \subseteq \text{supp}(U(L_1 \cdots L_k))} [U(L_k \cdots L_1)^\dagger Q U(L_k \cdots L_1) = \pm P] \right\}, \quad (\text{A29})$$

where $\text{supp}(U) = \{i \in \{1, \dots, n\} \mid U \text{ acts non-trivially on qubit } i\}$. The reasoning for this assumption is that if the sequence $L_1 \cdots L_k$ does not act on a given qubit, then that qubit cannot incur an error.

The quantity M_k provides an upper bound on the probability that errors whose first and last occurrences are separated by k layers cancel. Using the combinatorial decomposition introduced above, the probability that exactly $l > 1$ errors occur and that the two extreme errors (separated by k layers) cancel is bounded by

$$(1 - \epsilon_\mu)^{d-l} \epsilon_\mu^l (d - k) \binom{k-1}{l-2} M_k,$$

since there are $(d - k)$ choices for the positions of the first and last error and $\binom{k-1}{l-2}$ ways to place the remaining $l - 2$ errors between them. Consequently, the probability that $l > 1$ errors produce cancellation (for any allowed separation k) satisfies

$$\Pr[\text{cancellation} \mid l \text{ errors}] \leq (1 - \epsilon_\mu)^{d-l} \epsilon_\mu^l \sum_{k=l-1}^{d-1} (d-k) \binom{k-1}{l-2} M_k. \quad (\text{A30})$$

Finally, summing over all possible numbers of errors $l \geq 2$ yields an upper bound on the total cancellation probability (the contribution that we called s_2):

$$s_2 \leq \sum_{l=2}^d (1 - \epsilon_\mu)^{d-l} \epsilon_\mu^l \sum_{k=l-1}^{d-1} (d-k) \binom{k-1}{l-2} M_k. \quad (\text{A31})$$

Equations (A30) and (A31) are the desired bounds expressing how the separation-dependent cancellation probabilities M_k control the overall cancellation contribution s_2 . We can reorganize the expression so that the summation over k appears first. In this way, we obtain

$$s_2 \leq \sum_{k=1}^{d-1} M_k (d-k) \sum_{j=0}^{k-1} \binom{k-1}{j} (1 - \epsilon_\mu)^{d-j-2} \epsilon_\mu^{2+j} = \epsilon_\mu^2 \sum_{k=1}^{d-1} M_k (d-k) (1 - \epsilon_\mu)^{d-1-k}. \quad (\text{A32})$$

Therefore, given an estimate of M_k for every k , we obtain a bound on the probability of error cancellation as a function of ϵ_μ . This bound characterizes the regime in which our procedure can provide a reliable estimate of s_1 .

2. Verification of Conditions via Simulations

To evaluate the reliability of our procedure, we need to estimate M_k for different values of k , ranging from 1 up to one less than the maximum number of layers considered in the protocol. This can be achieved through classical simulations designed to approximate M_k efficiently. The simulation procedure for a given k consists of randomly selecting L_1, \dots, L_k μ -fraction circuits a total of R times, and computing

$$P = U(L_1 \cdots L_k) Q U(L_1 \cdots L_k)^\dagger, \quad (\text{A33})$$

with global phases removed, for all $Q \in \mathcal{P}$ such that $\text{supp}(Q) \subseteq \text{supp}(U(L_1 \cdots L_k))$. Each resulting Pauli operator P is then recorded. Among the R trials, we identify the pair (Q, P) that occurs most frequently.

A direct implementation of this procedure is not scalable, since the Pauli group contains 4^N elements. However, scalability can be achieved by restricting the analysis to Pauli operators of small weight, e.g., weight less than 4. Intuitively, this restriction corresponds to the worst-case scenario, as low-weight errors cannot fully spread across all qubits. For higher-weight Paulis, errors tend to delocalize more efficiently and the probability of cancellation decreases, as discussed in [56]. This intuition is supported by numerical simulations showing that the probability of error cancellation decreases with increasing Pauli weight, as we can see in Fig. 8. Restricting the analysis to Pauli operators of weight 1, 2, and 3 yields a simulation that scales as $O(N^3)$ in the number of qubits, making the procedure computationally efficient. Examples of these simulations for different numbers of qubits and values of μ are presented in Fig. 8

3. A Trivial Upper Bound

Even without resorting to simulations, we can derive an upper bound on the cancellation error. This bound allows us to predict, for a given value of ϵ_μ , the regime in which our protocol is guaranteed to operate reliably. The worst-case scenario, corresponding to the maximum probability of error cancellation, occurs when there is only a single layer $U(L)$ between two errors, and this layer acts on a single qubit where both errors occur. Since $U(L)$ acts on only one qubit, and every single-qubit Clifford gate can be decomposed into a small set of basic gates, we can model $U(L)$ as a uniformly random single-qubit Clifford gate.

Under this assumption, conjugation by a Clifford maps each non-identity Pauli operator uniformly to every other non-identity Pauli operator. Consequently, the probability of error cancellation is simply $\frac{1}{3}$, as all non-identity Paulis

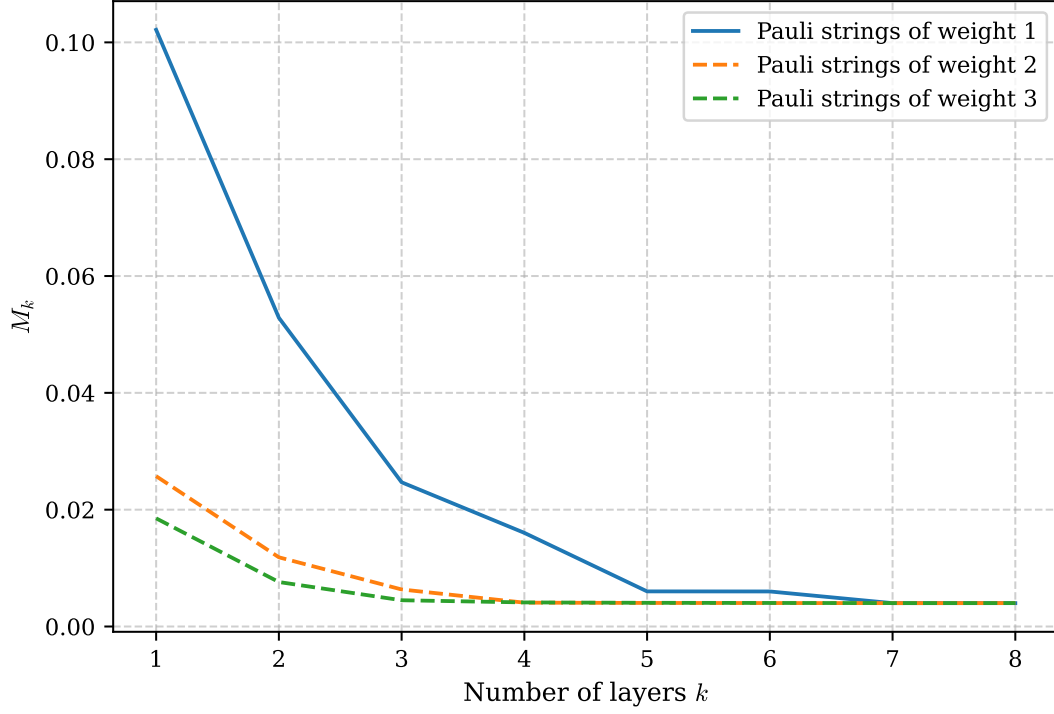


FIG. 8 Estimation of the values M_k defined in Eq. A29, which bound the probability that errors whose first and last occurrences are separated by k layers cancel. For each value of k , the quantities M_k are estimated using 500 different unitaries $U(L_k \cdots L_1)$, where each layer is constructed by taking 20% of the circuit obtained by compiling, with Qiskit 2.0.0, a fully random Clifford unitary acting on 10 qubits.

are equally likely. By setting all $M_k = \frac{1}{3}$, we obtain a conservative upper bound

$$s_2 \leq \epsilon_\mu^2 \sum_{k=1}^{d-1} \frac{1}{3} (d-k)(1-\epsilon_\mu)^{d-1-k} = \frac{1}{3} [1 - (1-\epsilon_\mu)^d - d \epsilon_\mu (1-\epsilon_\mu)^{d-1}]. \quad (\text{A34})$$

We now attempt to fit a curve of the form Af^d to the data obtained from

$$F_d = (1-\epsilon_\mu)^d + \frac{1}{3} [1 - (1-\epsilon_\mu)^d - d \epsilon_\mu (1-\epsilon_\mu)^{d-1}], \quad (\text{A35})$$

where s_2 is evaluated using the worst-case formula (A34). This allows us to assess the range of ϵ_μ for which this approximation is reasonable.

To perform the fitting, we apply linear regression to the logarithm of the data:

$$\log(F_d) \approx \log(Af^d) = \log(A) + d \log(f). \quad (\text{A36})$$

From this, the slope of the regression line provides an estimate of $\log(f)$, from which we define an approximate error rate

$$\tilde{\epsilon}_\mu = 1 - f \approx \epsilon_\mu. \quad (\text{A37})$$

If we try to estimate f using that F_d is defined as in (A34), the formula for the slope of linear regression using d continuous points (corresponding to d layers) is

$$f = \exp \left[\frac{d \sum_{k=1}^d k y_k - \sum_{k=1}^d k \sum_{k=1}^d y_k}{d \sum_{k=1}^d k^2 - \left(\sum_{k=1}^d k \right)^2} \right] = \exp \left[\frac{12 \sum_{k=1}^d k y_k}{d(d^2 - 1)} - \frac{6 \sum_{k=1}^d y_k}{d(d-1)} \right], \quad (\text{A38})$$

where $y_k = \log(F_k)$.

Using $d = 10$ total layers for estimating ϵ_μ and assuming $\epsilon_\mu \leq 0.1$, our predictions of $\tilde{\epsilon}_\mu$ are reasonably close to the true ϵ_μ as we can see in Fig. 9. For a larger number of layers, however, this approximation becomes less accurate. This suggests that, at least for $\epsilon_\mu \leq 0.1$ and a moderate number of layers, we have analytically shown that our protocol can provide a reliable estimate of ϵ_μ . In practice, the actual error is even smaller, as our bound is tighter, a fact confirmed by numerical simulations and illustrated, for example, in Fig. 10.

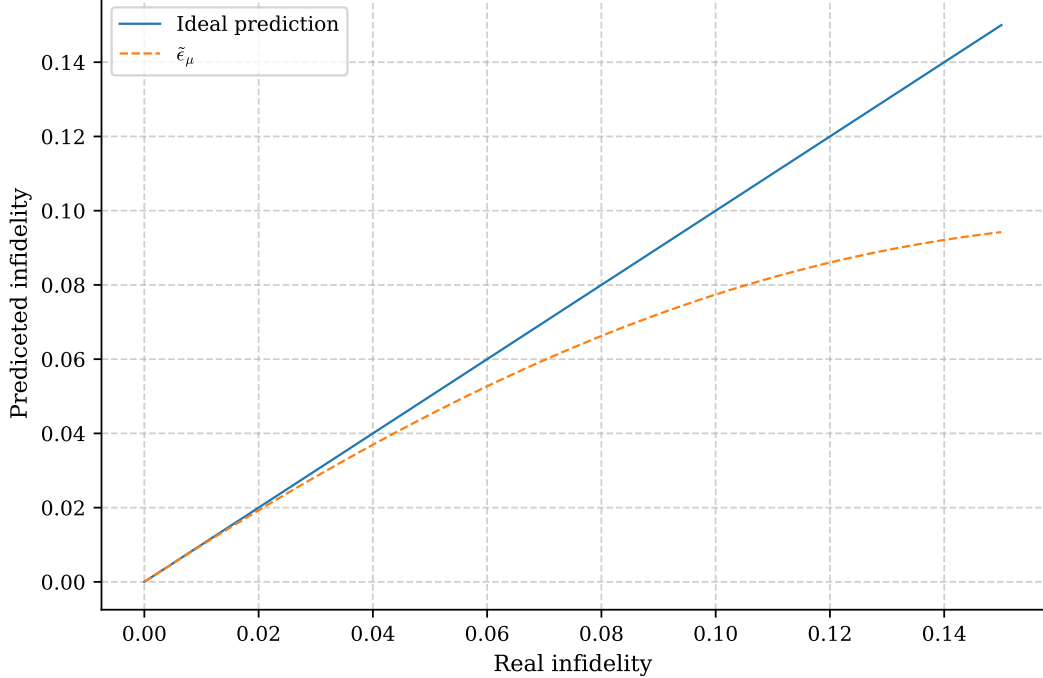


FIG. 9 Prediction of the device infidelity using 10 layers under the worst-case cancellation assumption where the probability of error cancellation is bounded by Eq. A34. The blue curve represents the prediction assuming no error cancellation, while $\tilde{\epsilon}_\mu$ correspond to the predicted values of the real infidelities, considering error cancellation. For infidelities below 0.1, the predicted values deviate by less than 0.025 from the true infidelity, consistently underestimating the actual error.

Appendix B: Quantum circuit to implement Quantum Signal processing

This appendix details the construction of the quantum circuits used in the TFIM Hamiltonian simulation benchmark protocol described in Sec. 3.

1. Quantum circuit for the block-encoding of the Hamiltonian

Here, we describe the construction of the operators \hat{U}_{Prep} and \hat{U}_{Select} required for the block-encoding of the Hamiltonian, defined as

$$\hat{U}_H = \begin{pmatrix} \hat{H}/\alpha & * \\ * & * \end{pmatrix} = (\hat{U}_{\text{Prep}}^\dagger \otimes \mathbb{I}_{s \times s}) \hat{U}_{\text{Select}} (\hat{U}_{\text{Prep}} \otimes \mathbb{I}_{s \times s}). \quad (\text{B1})$$

This decomposition allows the Hamiltonian to be encoded in the upper-left block of the unitary operator \hat{U}_H . In the following subsections, we introduce the protocols used to construct the quantum circuits.

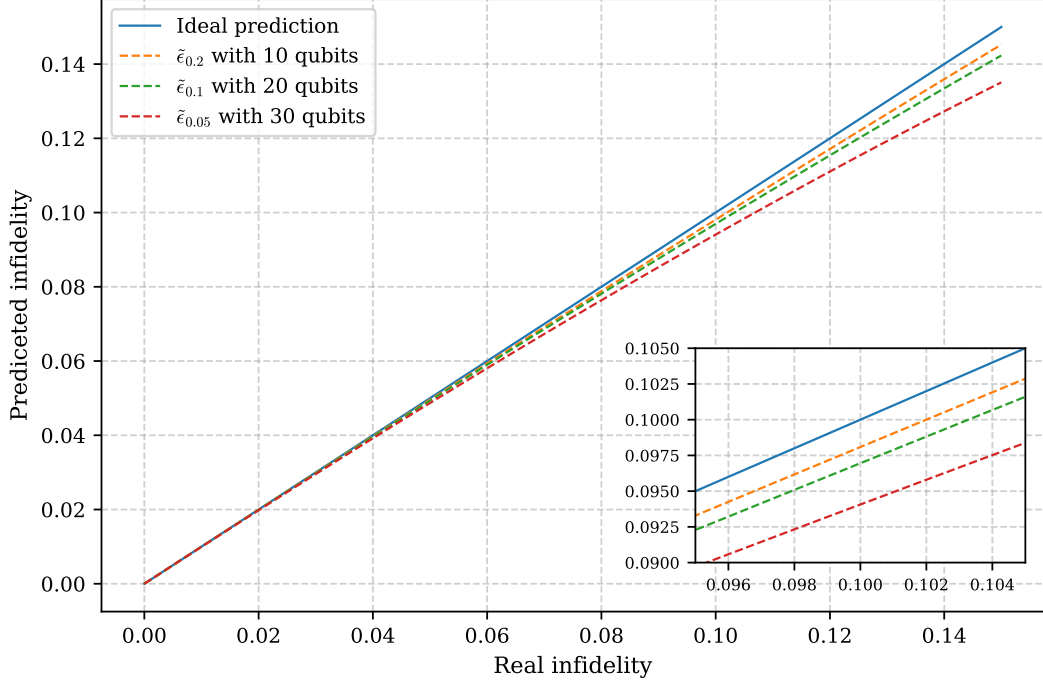


FIG. 10 Prediction of the device infidelity using 12 layers where the probability of error cancellation is computed according to Eq. A32. The values of M_k are estimated via simulations using pauli strings of weight 1, and the final prediction is obtained using linear regression. The blue curve represents the prediction assuming no error cancellation, while $\tilde{\epsilon}_\mu$ corresponds to the predicted values of the real infidelity for different numbers of qubits and μ , considering error cancellation.

a. *Quantum circuit implementing the operator \hat{U}_{Prep}*

The purpose of \hat{U}_{Prep} is to load the normalized coefficients of the Hamiltonian into the amplitudes of a quantum state. We employ the quantum state preparation algorithm proposed in Ref. [142], which constructs arbitrary quantum states through a recursive sequence of R_y and controlled- R_y rotations. Fig. 11 illustrates the general structure of the circuit. The protocol is described as follows:

Protocol 5: Quantum circuit implementing \hat{U}_{Prep} .

Initialization: Vector \mathbf{P} with dimension $2L$.
Return: Quantum circuit implementing \hat{U}_{Prep} .
Procedure:

1. **Dimension normalization:** Let $d = 2L$ and define

$$m = \lceil \log_2 d \rceil, \quad D = 2^m.$$
 If $d < D$, extend vector \mathbf{P} by padding with zeros,

$$\mathbf{P}[j] = \begin{cases} \mathbf{P}[j], & 0 \leq j < d, \\ 0, & d \leq j < D. \end{cases}$$

2. **First level of norms and angles computation:** For each $s \in \left\{0, 1, \dots, \frac{\dim(\mathbf{P})}{2} - 1\right\}$, compute the norms

as follows:

$$\text{norm}_1[s] = \sqrt{\mathbf{P}[2s]^2 + \mathbf{P}[2s+1]^2}.$$

Then, compute the rotation angles:

$$\text{angles}_1[s] = 2 \arccos \left(\frac{\mathbf{P}[2s]}{\text{norm}_1[s]} \right).$$

Notice that, if $\text{norm}_1[s] = 0$, the corresponding angle is set to 0.

3. Recursive norm calculation: Repeat the same procedure recursively using vectors obtained in the previous step. At the k -th level, compute the norms as follows:

$$\text{norm}_k[s] = \sqrt{\text{norm}_{k-1}[2s]^2 + \text{norm}_{k-1}[2s+1]^2}, \quad (\text{B2})$$

$$\text{angles}_k[s] = 2 \arccos \left(\frac{\text{norm}_{k-1}[2s]}{\text{norm}_k[s]} \right), \quad (\text{B3})$$

for $k = 2, \dots, m$ and $s \in \left\{0, 1, \dots, \frac{\dim(\text{norm}_{k-1})}{2} - 1\right\}$.

Notice that, if $\text{norm}_k[s] = 0$, the corresponding angle is set to 0.

4. Circuit construction: Consider a quantum circuit with m ancillary qubits, labeled q_0, \dots, q_{m-1} . The circuit is built as a sequence of controlled- R_y rotations. Each rotation is written as $R_y^{\theta_{k,s}}$, where $\theta_{k,s}$ denotes the angle computed at level k for index s . The quantum circuit implementing \hat{U}_{Prep} is described as follows:

- Apply the quantum gate $R_y^{\theta_{m,0}}$ to qubit q_0 .
- Then, for each level $k = m-1, \dots, 1$, apply the controlled- $R_y^{\theta_{k,s}}$ rotations to the ancillary qubit q_{m-k} , covering all possible controlled conditions of the ancillary qubits q_0, \dots, q_{m-k-1} . Fig. 11 shows the quantum circuits to implement \hat{U}_{Prep} .

b. Quantum circuit implementing the operator \hat{U}_{Select}

The operator \hat{U}_{Select} is implemented using multi-controlled Pauli operators acting on main system, conditioned on the state of the m ancillary qubits. Fig. 12 shows the quantum circuit used to implement \hat{U}_{Select} , where each unitary \hat{U}_i corresponds to a Pauli operator acting on the main system, conditioned on the ancilla register being in the state $|i\rangle$. The black circle denotes a control on the ancillary qubit being in the state $|1\rangle$ while denotes a control on the ancillary qubit being in the state $|0\rangle$. The protocol used to construct the quantum circuit is described as follows:

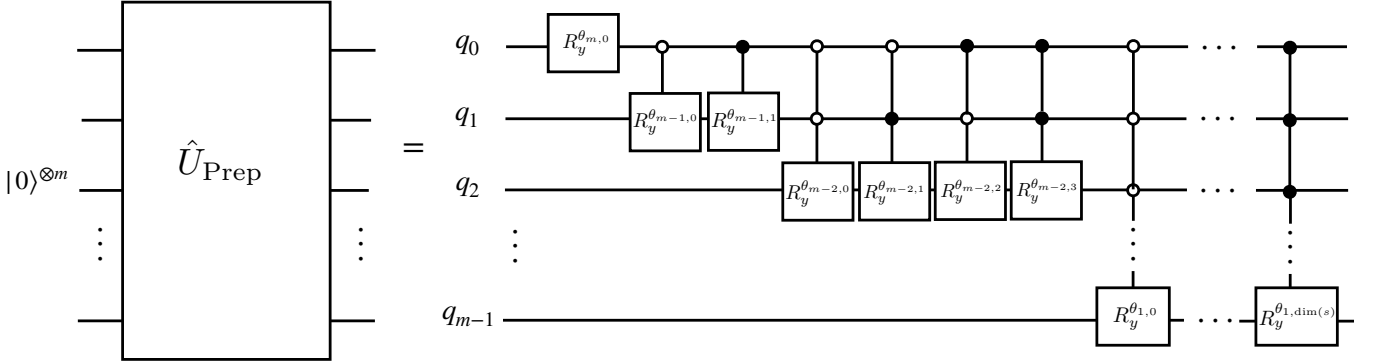


FIG. 11 Construction of the Quantum circuit to implement \hat{U}_{Prep} following the Protocol 5. The circuit consists of a sequence of controlled R_y rotations, where each rotation angle is obtained recursively from the vector \mathbf{P} . The R_y rotations are denoted by $R_y^{\theta_{k,s}}$, where $\theta_{k,s}$ are the angles computed at the k -th level for index s .

Protocol 6: Quantum circuit implementing \hat{U}_{Select}

Initialization: Vector $\mathbf{U} = [\hat{U}_0, \hat{U}_1, \dots, \hat{U}_{2L-1}]$ with dimension $2L$.

Return: Quantum circuit implementing \hat{U}_{Select} .

Procedure:

1. **Dimension normalization:** Let $d = 2L$ and define

$$m = \lceil \log_2 d \rceil, \quad D = 2^m.$$

If $d < D$, extend the vector \mathbf{U} by padding with identity operators,

$$\mathbf{U}[j] = \begin{cases} \mathbf{U}[j], & 0 \leq j < d, \\ \mathbb{I}_{2L}, & d \leq j < D. \end{cases}$$

2. **Circuit construction:** Consider a quantum circuit with m ancillary qubits labeled q_0, \dots, q_{m-1} . For each $i = 0, \dots, D-1$, apply the controlled operator \hat{U}_i to the system register, where \hat{U}_i is conditioned on the state of the ancillary qubits, as illustrated in Fig. 12. A black circle indicates conditioning on the ancillary qubit being in the state $|1\rangle$, whereas a white circle indicates conditioning on the state $|0\rangle$.

c. Protocol to compute phase angles

In the TFIM Hamiltonian simulation benchmark, we employ the Fixed-Point Iteration method to compute the phase angles [143]. The algorithm used to compute the phases is described as follows:

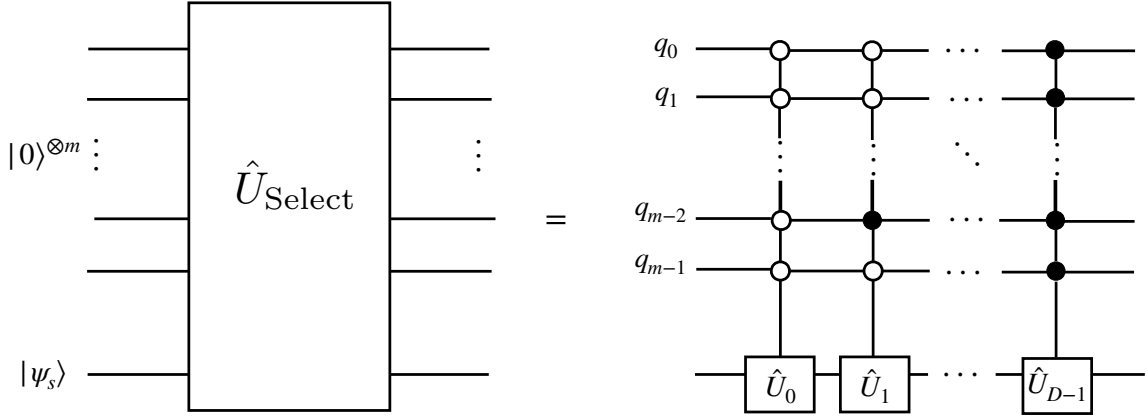


FIG. 12 Quantum circuit implementing the operator \hat{U}_{Select} . Each controlled operator \hat{U}_i (for $i = 0, \dots, D - 1$) acts on the system register and is applied conditionally on the state of the m ancillary qubits. Black and white control circles indicate conditioning on the $|1\rangle$ and $|0\rangle$ states of the ancilla qubits, respectively.

Protocol 7: Algorithm for Computing Phase angles

Initialization: Vector \mathbf{C} containing the coefficients of the Chebyshev expansion and the parity $p \in \{0, 1\}$ of the target function, where $p = 0$ corresponds to an even function and $p = 1$ to an odd function.

Return: Sequence of phase angles ϕ .

Procedure:

1. **Apply fixed-point iteration:** Initialize the phase vector as $\phi^{(0)} = 0$ and set the iteration counter $t = 0$. Iteratively update the phase vector according to

$$\phi^{(t+1)} = \phi^{(t)} - \frac{1}{2} \left[F(\phi^{(t)}) - \mathbf{C} \right], \quad (\text{B4})$$

where $F(\phi^{(t)})$ returns the Chebyshev coefficients generated by the current phase vector. If $\|F(\phi^{(t)}) - \mathbf{C}\|_1 < \epsilon$ with $\epsilon = 10^{-10}$, stop the iteration and return the phase vector.

The Chebyshev coefficients, $F(\phi^{(t)})$, generated by the phase vector are computed as follows:

- (a) **Evaluate $P_{\text{im}}(x_j)$ at Chebyshev nodes:** Given the phase vector $\phi^{(t)}$ and the parity p of the target function, evaluate the imaginary part of the $(1, 1)$ element of the QSP unitary at the Chebyshev nodes

$$x_j = \cos(\theta_j), \quad j = 0, 1, \dots, \ell.$$

where $\theta_j = \frac{j\pi}{2\ell}$ and ℓ denotes the length of the phase vector ϕ .

Then, compute the imaginary component as follows:

$$P_{\text{im}}(x_j) = \Pi_\ell \left(\prod_{k=1}^{\ell-1} B(\theta_j) R_z(2\phi_k) \right) R_0(\theta_j),$$

where the initial vector is defined as

$$R_0(\theta_j) = \begin{cases} (1, 0, 0)^\top, & \text{if } p = 0 \text{ (even),} \\ (\cos \theta_j, 0, \sin \theta_j)^\top, & \text{if } p = 1 \text{ (odd).} \end{cases}$$

The rotation matrices are defined as

$$R_z(2\phi_k) = \begin{pmatrix} \cos(2\phi_k) & -\sin(2\phi_k) & 0 \\ \sin(2\phi_k) & \cos(2\phi_k) & 0 \\ 0 & 0 & 1 \end{pmatrix},$$

and

$$B(\theta_j) = \begin{pmatrix} \cos(2\theta_j) & 0 & -\sin(2\theta_j) \\ 0 & 1 & 0 \\ \sin(2\theta_j) & 0 & \cos(2\theta_j) \end{pmatrix}.$$

The projection vector is defined as

$$\Pi_\ell = (\sin(2\phi_\ell), \cos(2\phi_\ell), 0).$$

(b) **Extend the sequence with parity symmetry:** Build the vector $\{y_j\}_{j=0}^{2\ell}$ by reflecting the imaginary component with the required parity,

$$y_j = \begin{cases} S_j, & j = 0, 1, \dots, \ell, \\ (-1)^p S_{2\ell-j}, & j = \ell + 1, \dots, 2\ell, \end{cases}$$

where $S_j = P_{\text{im}}(x_j)$. This even/odd symmetric extension enforces the desired parity in the Chebyshev expansion.

(c) **Compute Chebyshev coefficients via Discrete Cosine Transform (DCT):** The DCT is defined by

$$Y_k = \sum_{j=0}^{2\ell} y_j \cos\left(\frac{\pi j k}{2\ell}\right), \quad k = 0, 1, \dots, 2\ell.$$

Normalize the first and last coefficients of the vector $\{Y_k\}_{k=0}^{2\ell}$ by $\frac{1}{4\ell}$ and all intermediate coefficients by $\frac{1}{2\ell}$.

(d) **Select coefficients matching the parity:** Extract the subsequence depending of the parity

$$F(\phi^{(t)}) = \begin{cases} (Y_0, Y_2, Y_4, \dots)_{[0:\ell-1]}, & p = 0 \text{ (even)}, \\ (Y_1, Y_3, Y_5, \dots)_{[0:\ell-1]}, & p = 1 \text{ (odd)}. \end{cases}$$

2. **Construct the full phase sequence.** After convergence of the fixed-point iteration, the reduced phase vector $\phi = (\phi_1, \phi_2, \dots, \phi_\ell)$ is obtained. The full complete QSP sequence is generated as follows:

$$\phi = (\phi_\ell + \frac{\pi}{4}, \dots, \phi_1, \phi_1, \dots, \phi_\ell + \frac{\pi}{4}).$$

d. Quantum circuit to implement the projector-controlled phase gate Π_{ϕ_k}

The quantum circuit to implement the phase-controlled projector Π_{ϕ_k} is described as follows:

Protocol 8: Quantum circuit to implement the projector Π_{ϕ_k}

Initialization: Sequence of phase angles ϕ .
Return: Quantum circuit implementing Π_{ϕ_k} .
Procedure:

1. **Circuit construction:** For each ϕ_k , apply the following quantum gates consecutively:

(a) **Apply the controlled C_PNOT gate:** Apply a multi-controlled NOT gate defined as

$$C_P\text{NOT} = X \otimes P + \mathbb{I} \otimes (\mathbb{I} - P),$$

where $P = |0\rangle^{\otimes m}\langle 0|^{\otimes m}$ projects onto the all-zero m -qubit ancilla state.

(b) **Apply the phase rotation:** Apply a single-qubit rotation around the Z axis on the ancilla qubit q_A :

$$R_Z(2\phi_k).$$

(c) **Reapply the controlled C_PNOT gate:** Apply again the same multi-controlled NOT gate:

$$C_P\text{NOT} = X \otimes P + \mathbb{I} \otimes (\mathbb{I} - P).$$

Fig. 13 shows the quantum circuits to implement Π_{ϕ_k} .

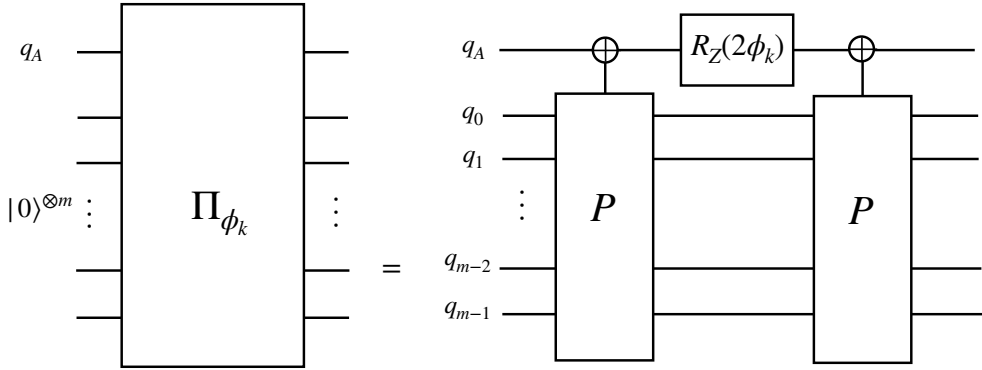


FIG. 13 Quantum circuit implementing the projector Π_{ϕ_k} using multi-controlled phase operations. The circuit applies a controlled projector $P = |0\rangle^{\otimes m}\langle 0|^{\otimes m}$ onto the ancillary register, followed by a single-qubit rotation $R_Z(2\phi_k)$ on the ancilla qubit q_A , and a second controlled application of P .

Appendix C: Error Bounds and Success Probability in QSP method for Hamiltonian Simulation

1. Polynomial Approximation Error in QSP

Quantum Signal Processing (QSP) is a powerful technique that enables the implementation of polynomial approximations of matrix functions using a sequence of single-qubit rotations controlled by an ancilla qubit [110]. In the context of Hamiltonian simulation, given a target function $e^{-i\hat{H}t/\alpha}$, QSP constructs a polynomial $P(t\hat{H}/\alpha)$ that approximates this target operator over the normalized spectral domain $\lambda_k \in [-1, 1]$, where λ_k denotes an eigenvalue of the rescaled Hamiltonian \hat{H}/α . The approximation error is bounded by

$$\| P(t\hat{H}/\alpha) - e^{-i\hat{H}t/\alpha} \|_2 \leq \varepsilon_0, \quad (\text{C1})$$

where $\| \cdot \|_2$ denotes the spectral norm. Since any Hamiltonian can be diagonalized in its eigenbasis as

$$\hat{H} = \sum_k \lambda_k |\lambda_k\rangle\langle\lambda_k|, \quad (\text{C2})$$

the functions $P(t\hat{H}/\alpha)$ and $e^{-i\hat{H}t/\alpha}$ can be expressed in terms of their eigenvalues as

$$P(t\hat{H}/\alpha) = \sum_k P(t\lambda_k/\alpha) |\lambda_k\rangle\langle\lambda_k|, \quad e^{-i\hat{H}t/\alpha} = \sum_k e^{-i\lambda_k t/\alpha} |\lambda_k\rangle\langle\lambda_k|. \quad (\text{C3})$$

Therefore, the operator norm in Eq. (C1) is equivalently given by the maximum deviation between the two complex functions evaluated on the eigenvalue spectrum of the Hamiltonian:

$$\| P(t\hat{H}/\alpha) - e^{-i\hat{H}t/\alpha} \|_2 = \max_{\lambda_k \in \text{spec}(\hat{H})} | P(t\lambda_k/\alpha) - e^{-i\lambda_k t/\alpha} | \leq \varepsilon_0. \quad (\text{C4})$$

This definition ensures that the polynomial approximation holds uniformly for all eigenvalues of the rescaled Hamiltonian

$$| P(t\lambda_k/\alpha) - e^{-i\lambda_k t/\alpha} | \leq \varepsilon_0, \quad \forall \lambda_k \in [-1, 1]. \quad (\text{C5})$$

2. Success Probability in the QSP Circuit

To implement the polynomial $P(t\hat{H}/\alpha)$, QSP constructs a unitary operator represented as

$$\hat{U}_{\text{QSP}} = \begin{pmatrix} P(t\hat{H}/\alpha) & * \\ * & * \end{pmatrix}, \quad (\text{C6})$$

which acts on the main system and ancilla qubits. As we discussed in the main text, to implement the approximation of the time-evolution operator $e^{-i\hat{H}t/\alpha}$ we use two polynomials that approximate $\cos(t\hat{H}/\alpha)$ and $\sin(t\hat{H}/\alpha)$. Figure 3 shows the quantum circuit used to approximate the time-evolution operator. The Hadamard gates acting on the ancillary qubit q_B enable the coherent implementation of both $U_{\text{QSP}}^{(\cos)}$ and $U_{\text{QSP}}^{(\sin)}$. After applying the full quantum circuit, the resulting quantum state is given by

$$|\psi\rangle = \frac{1}{2} \left[|0\rangle_B |0\rangle_A |0\rangle^{\otimes m} (P_{\cos}(t\hat{H}/\alpha) + P_{\sin}(t\hat{H}/\alpha)) |\psi_s\rangle + |1\rangle_B |0\rangle_A |0\rangle^{\otimes m} (P_{\cos}(t\hat{H}/\alpha) - iP_{\sin}(t\hat{H}/\alpha)) |\psi_s\rangle \right] + |\psi'_\perp\rangle, \quad (\text{C7})$$

where $|\psi'_\perp\rangle$ is an orthogonal state. Measuring the ancilla qubits and post-selecting the measurement outcome $|1\rangle_B |0\rangle_A |0\rangle^{\otimes m}$ projects the main system onto the state

$$\frac{P(t\hat{H}/\alpha) |\psi_s\rangle}{\|P(t\hat{H}/\alpha) |\psi_s\rangle\|}, \quad (\text{C8})$$

where $\|P(t\hat{H}/\alpha) |\psi_s\rangle\|$ is lower bounded by $1 - \varepsilon_0$. Here $P(t\hat{H}/\alpha) = P_{\cos}(t\hat{H}/\alpha) - iP_{\sin}(t\hat{H}/\alpha)$ denotes the QSP polynomial approximation of $e^{-i\hat{H}t/\alpha}$. The success probability P_{succ} to obtain this outcome reads

$$P_{\text{succ}} = \frac{1}{4} \|P(t\hat{H}/\alpha) |\psi_s\rangle\|^2. \quad (\text{C9})$$

Using triangular inequality and the Eq. (C1), the success probability is lower bounded by

$$P_{\text{succ}} \geq \frac{1}{4} (1 - \varepsilon_0)^2. \quad (\text{C10})$$

This result provides a direct connection between the polynomial approximation error ε_0 and the success probability of the Hamiltonian simulation.

3. Error in expectation values

In the TFIM Hamiltonian simulation benchmark, the observable of interest is the average total magnetization, defined as

$$\hat{M}_z = \frac{1}{L} \sum_{j=1}^L \hat{Z}_j, \quad (\text{C11})$$

where \hat{Z}_j denotes the local Pauli-Z operator acting on qubit j . Since the quantum state prepared on the quantum processor using the Quantum Signal Processing (QSP) technique is an approximation of the exact time-evolved state, the estimated magnetization deviates from the exact value. Using the triangle inequality and the Cauchy–Schwarz inequality, the deviation in the expectation value of the average magnetization can be upper bounded as follows:

$$\|\langle \psi' | \hat{M}_z | \psi' \rangle - \langle \psi | \hat{M}_z | \psi \rangle\| \leq 2 \|\hat{M}_z\| \|\psi' - \psi\|, \quad (\text{C12})$$

where $\|\hat{M}_z\| = 1$, the states $|\psi\rangle$ and $|\psi'\rangle$ denote the exact time-evolved state $e^{-i\hat{H}t/\alpha}|\psi(0)\rangle$ and the approximate state $P(t\hat{H}/\alpha)|\psi(0)\rangle$ obtained through the QSP implementation, respectively. Using the bound in Eq. (C1) and the triangle inequality, the norm of the distances between the exact and approximate state can be bounded in terms of the polynomial approximation error ε_0 as follows:

$$\|\psi' - \psi\| = \|P(t\hat{H}/\alpha)|\psi(0)\rangle - e^{-i\hat{H}t/\alpha}|\psi(0)\rangle\| \leq \varepsilon_0. \quad (\text{C13})$$

Therefore, the deviation in the expectation value of the average magnetization can be upper bounded by

$$\|\langle \psi' | \hat{M}_z | \psi' \rangle - \langle \psi | \hat{M}_z | \psi \rangle\| \leq 2\varepsilon_0. \quad (\text{C14})$$

Appendix D: Iterative training of the multi-qubit QNN architecture

In this appendix, we describe the protocol used to train the one-qubit QNN and the multi-qubit QNN architectures employing data re-uploading. The protocols are described as follow:

Protocol 9: Train the one-qubit QNN architecture

Initialization: Training dataset $\mathcal{X} = \{(\mathbf{x}^{(i)}, y_x^{(i)})\}_{i=1}^{M_x}$.

Return: The optimized parameters $\{\boldsymbol{\theta}^*\}$ ¹ for one-qubit QNN architecture where $\boldsymbol{\theta}^*$ contains the parameters $\{\theta_{l,1}^{(1)}, \theta_{l,2}^{(1)}, \theta_{l,3}^{(1)}\}$ for $l \in \{1, \dots, L\}$.

Procedure:

1. For $t = 1$ to the number of attempts chosen by the user.

(a) **Initialize parameters.** The parameters $\boldsymbol{\theta} = \{\boldsymbol{\theta}_l^{(1)}\} = \{\theta_{l,1}^{(1)}, \theta_{l,2}^{(1)}, \theta_{l,3}^{(1)}\}$ are initialized within range $[-\pi, \pi]$, for all $l \in \{1, \dots, L\}$, according to a strategy selected by the user.

(b) **Train the QNN architecture.** For each input $\mathbf{x}^{(i)} \in \mathcal{X}$:

- i. **Construct the circuit.** Implement the circuit given by the Eq. 26, where the data encoding of $\mathbf{x}^{(i)}$ is given by Eq. 28 and the parameters encoding is given by Eq. 29.
- ii. **Measure.** Measure the qubit in the computational basis and estimate the expectation value of the Pauli Z operator. This is achieved by repeatedly measuring in the computational basis, assigning the value $+1$ to outcome $|0\rangle$ and -1 to outcome $|1\rangle$, and computing the sample mean $\hat{\mu}_{\boldsymbol{\theta}}^{(i)}$. The total number of shots required depends on the desired estimation precision: to guarantee a maximum error ε with confidence $1 - \delta$, one requires

$$\frac{2}{\varepsilon^2} \log\left(\frac{2}{\delta}\right) \quad (\text{D1})$$

shots.

- iii. **Cost function evaluation.** Compute the cost function:

$$\mathcal{L}(\boldsymbol{\theta}) = 1 - \frac{1}{M_x} \sum_{i=1}^{M_x} F^{(i)}(\hat{\mu}_{\boldsymbol{\theta}}^{(i)}),$$

where $F^{(i)}$ denotes the fidelity with respect to the corresponding label $y_x^{(i)}$ as follows

$$F^{(i)}(\mu) = \frac{1 + y_x^{(i)}\mu}{2}, \quad y_x^{(i)} \in \{-1, 1\}.$$

iv. **Gradient estimation.** For each parameter $\theta_{l,j}^{(1)} \in \boldsymbol{\theta}$ with $j \in \{1, 2, 3\}$ and $l \in \{1, \dots, L\}$, the gradient of the cost function is estimated using the parameter-shift rule [137]. This requires estimate the expectation value of the Pauli Z operator after shifting only the parameter by $\theta_{l,j}^{(1)} \pm \frac{\pi}{2}$, while keeping all other parameters fixed (see Fig. 14).

$$\frac{\partial \mathcal{L}}{\partial \theta_{l,j}^{(1)}} = -\frac{1}{M_x} \sum_{i=1}^{M_x} \frac{y_x^{(i)}}{4} \left(\langle Z \rangle_+ - \langle Z \rangle_- \right),$$

where $\langle Z \rangle_{\pm}$ denote the expectation values of Pauli Z operator after running the QNN architecture with $\theta_{l,j}^{(1)} \pm \frac{\pi}{2}$ respectively. These expectation values are estimated according to the procedure described in the previous step.

v. **Parameter update.** Update all the parameters as follows

$$\theta_{l,j}^{(1)} = \theta_{l,j}^{(1)} - \eta \frac{\partial \mathcal{L}}{\partial \theta_{l,j}^{(1)}},$$

denotes the learning rate, selected by the user, which may vary across training rounds. Go to Step 1b and repeat with the new parameters, until the convergence criterion chose by the user is satisfied.

(c) **Optimal parameter update.** If $t = 1$, or if $t > 1$ and $\mathcal{L}(\boldsymbol{\theta}) < \mathcal{L}(\boldsymbol{\theta}^*)$ then update $\boldsymbol{\theta}^* = \boldsymbol{\theta}$.

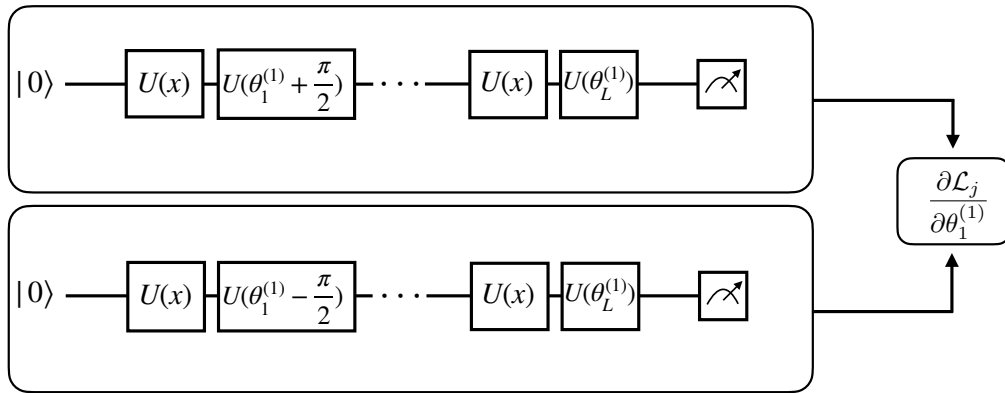


FIG. 14 Gradient estimation using the parameter-shift rule. The QNN architecture is evaluated twice with the parameter $\theta_1^{(1)}$ shifted by $\pm \frac{\pi}{2}$, while all other parameters are kept fixed.

Protocol 10: Train the N-qubit QNN architecture

Initialization: Training dataset $\mathcal{X} = \{(\mathbf{x}^{(i)}, y_x^{(i)})\}_{i=1}^{M_x}$, and the optimal parameters of the $(N - 1)$ -QNN $\{\boldsymbol{\theta}^*, \boldsymbol{\varphi}^*\}_{N-1}^N$.

Return: The optimized parameters $\{\boldsymbol{\theta}^*, \boldsymbol{\varphi}^*\}^N$ for the N -QNN architecture where $\boldsymbol{\theta}^*$ contains the parameters $\{\theta_{l,1}^{(r)}, \theta_{l,2}^{(r)}, \theta_{l,3}^{(r)}\}$ for $r \in \{1, \dots, N\}$ and $l \in \{1, \dots, L\}$; and $\boldsymbol{\varphi}^*$ contains the parameters $\{\varphi_{l,1}^{(s)}, \varphi_{l,2}^{(s)}, \varphi_{l,3}^{(s)}\}$ for $s \in \{1, \dots, N - 1\}$ and $l \in \{1, \dots, L\}$.

Procedure:

1. Initialize parameters. The parameters of the N -QNN will be $\boldsymbol{\theta} = \{\boldsymbol{\theta}_l^{(1)}, \dots, \boldsymbol{\theta}_l^{(N)}\}$ where $\boldsymbol{\theta}_l^{(r)} = \{\theta_{l,1}^{(r)}, \theta_{l,2}^{(r)}, \theta_{l,3}^{(r)}\}$ and $\boldsymbol{\varphi} = \{\boldsymbol{\varphi}_l^{(1)}, \dots, \boldsymbol{\varphi}_l^{(N-1)}\}$ where $\boldsymbol{\varphi}_l^{(s)} = \{\varphi_{l,1}^{(s)}, \varphi_{l,2}^{(s)}, \varphi_{l,3}^{(s)}\}$ for all $l \in \{1, \dots, L\}$. The parameters of the N -QNN acting on qubits from 1 to $N-1$ will be equals to the optimal parameters of the $(N-1)$ -QNN; and the parameters of the new qubit will be initialized to 0, i.e.

- $\theta_{l,j}^{(r)} = \theta_{l,j}^{*(r)}$, $\forall j \in \{1, 2, 3\}$, $r \in \{1, \dots, N-1\}$, $l \in \{1, \dots, L\}$.
- $\varphi_{l,j}^{(r)} = \varphi_{l,j}^{*(r)}$, $\forall j \in \{1, 2, 3\}$, $r \in \{1, \dots, N-2\}$, $l \in \{1, \dots, L\}$.
- $\theta_{l,j}^{(N)} = 0$, $\forall j \in \{1, 2, 3\}$, $l \in \{1, \dots, L\}$.
- $\varphi_{l,j}^{(N-1)} = 0$, $\forall j \in \{1, 2, 3\}$, $l \in \{1, \dots, L\}$.

where $\theta_{l,j}^{*(r)}$ and $\varphi_{l,j}^{*(r)}$ are the optimal parameters of the $(N-1)$ -QNN, $\{\boldsymbol{\theta}^*, \boldsymbol{\varphi}^*\}^{N-1}$.

2. Train the QNN architecture. For each input $\mathbf{x}^{(i)} \in \mathcal{X}$:

- Construct the circuit.** Implement the circuit given by the Eq. 26, where the data encoding of $\mathbf{x}^{(i)}$ is given by Eq. 28 and the parameters encoding is given by Eq. 29 and Eq. 30.
- Measure.** Measure the first qubit in the computational basis and estimate the expectation value of the Pauli Z operator, calculating $\hat{\mu}_{\boldsymbol{\theta}, \boldsymbol{\varphi}}^{(i)}$ as in Step 1(b)ii of the one-qubit QNN training protocol.
- Cost function evaluation.** Compute the cost function:

$$\mathcal{L}(\boldsymbol{\theta}) = 1 - \frac{1}{M_x} \sum_{i=1}^{M_x} F^{(i)}(\hat{\mu}_{\boldsymbol{\theta}, \boldsymbol{\varphi}}^{(i)}),$$

where $F^{(i)}$ is the same as in Step 1(b)iii of the one-qubit QNN training protocol.

- Gradient estimation.** For each parameter $\theta_{l,j}^{(r)} \in \boldsymbol{\theta}$ and $\varphi_{l,j}^{(s)} \in \boldsymbol{\varphi}$ with $j \in \{1, 2, 3\}$, $l \in \{1, \dots, L\}$, $r \in \{1, \dots, N\}$ and $s \in \{1, \dots, N-1\}$, the gradient of the cost function is estimated using the parameter-shift rule [137] following the procedure described in Step 1(b)iv, but extended to account for the increased number of parameters in the N -qubit QNN

$$\frac{\partial \mathcal{L}}{\partial \theta_{l,j}^{(r)}} = -\frac{1}{M_x} \sum_{i=1}^{M_x} \frac{y_x^{(i)}}{4} \left(\langle Z \rangle_+ - \langle Z \rangle_- \right), \quad (\text{D2})$$

$$\frac{\partial \mathcal{L}}{\partial \varphi_{l,j}^{(s)}} = -\frac{1}{M_x} \sum_{i=1}^{M_x} \frac{y_x^{(i)}}{4} \left(\langle Z \rangle_+ - \langle Z \rangle_- \right), \quad (\text{D3})$$

where $\langle Z \rangle_{\pm}$ denote the expectation values of Pauli Z operator after running the QNN architecture with $\theta_{l,j}^{(r)} \pm \frac{\pi}{2}$ respectively, in Eq. D2 and with $\varphi_{l,j}^{(s)} \pm \frac{\pi}{2}$ respectively, in Eq. D3. These expectation values are estimated according to the procedure described in the previous step.

- Parameter update.** Update all the parameters as follows

$$\theta_{l,j}^{(r)} = \theta_{l,j}^{(r)} - \eta \frac{\partial \mathcal{L}}{\partial \theta_{l,j}^{(r)}}, \quad (\text{D4})$$

$$\varphi_{l,j}^{(s)} = \varphi_{l,j}^{(s)} - \eta \frac{\partial \mathcal{L}}{\partial \varphi_{l,j}^{(s)}}, \quad (\text{D5})$$

where η denotes the learning rate, selected by the user, which may vary across training rounds. Go to Step 2 and repeat with the new parameters, until the convergence criterion chose by the user is satisfied.

- Return optimal parameters.** Store and return the parameters $\boldsymbol{\theta}, \boldsymbol{\varphi}$ as the optimal parameters $\{\boldsymbol{\theta}^*, \boldsymbol{\varphi}^*\}^N$ of the N -QNN.

Figure 15 illustrates the iterative training procedure of a two-qubit QNN architecture.

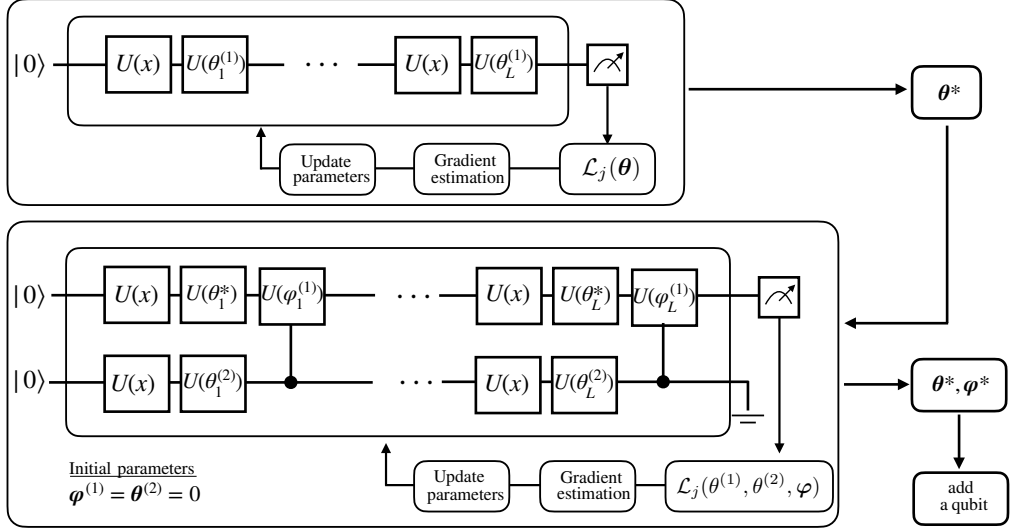


FIG. 15 Iterative training of a two-qubit QNN architecture. First, a single-qubit QNN is trained to obtain the optimal parameters, denoted by θ^* . Next, the two-qubit QNN is initialized by assigning these optimal parameters to the first qubit, while the additional parameters are initialized to zero.